Title
Old Dog, New Trick: High Fidelity, Background-free State Detection of an Ytterbium Ion Qubit

Author
Ransford, Anthony M

Publication Date
2020

Peer reviewed|Thesis/dissertation

UNIVERSITY OF CALIFORNIA
Los Angeles

Old Dog, New Trick: High Fidelity, Background-free State Detection of an Ytterbium Ion Qubit

A dissertation submitted in partial satisfaction
of the requirements for the degree
Doctor of Philosophy in Physics

by

Anthony Micheal Ransford

2020

ABSTRACT OF THE DISSERTATION

Old Dog, New Trick: High Fidelity, Background-free State Detection of an Ytterbium Ion Qubit

by

Anthony Micheal Ransford
Doctor of Philosophy in Physics
University of California, Los Angeles, 2020
Professor Wesley C. Campbell, Chair

The highly popular ytterbium-171 ($^{171}Yb^{+}$) ion is commonly employed in quantum information research as a qubit whose excellent coherence time and fast, simple state preparation has allowed cutting edge work in quantum computation and simulation. Despite these large benefits, the demonstrated measurement fidelity of this ion has lagged the state preparation and gate fidelity achieved to date.

In this thesis we investigate and realize methods of increasing the measurement fidelity of $^{171}Yb^{+}$ in a scaleable way for large quantum systems. Using methods of coherent control, we implement a pulsed state detection scheme using a mode-locked laser to perform background-free spectroscopy of the "bright" state of the qubit. The small hyperfine splitting of the ion necessitates the use of multiple (two) pulses to manipulate time dynamics of the ion to excite a single transition. A Mach-Zehnder interferometer is constructed to control these pulse separations both coarsely ($\sim$ 237 ps) and on a fine sub-femtosecond scale. These pulses cause destructive/constructive interference of the electron wave packet of a single ion levitated in vacuum and are engineered to state-selectively excite the qubit. This allows measurement of the qubit whose transition frequency is much smaller than the bandwidth of the interrogation laser.

During this spectroscopy, mechanical forces from the mode-locked laser frequency comb can drive the ion into large coherent states of motion. This motion has been dubbed "phonon lasing". We investigate the phonon lasing affect and how the ion interacts with multiple comb teeth. The large number of teeth leads to a protection mechanism from runaway energy gain by near-by blue detuned teeth, allowing ions to be trapped and cooled by the mode-locked laser, regardless of its detuning. We further explore these discrete amplitude coherent states by injecting energy into the ion's motion and exciting higher-order oscillations.

We, for the first time, implement an "electron shelving" of the hyperfine qubit, and incoherently transfer the bright state population in the extremely long-lived ($\approx$5 yr) $^2F_{7/2}$ state of $^{171}Yb^+$, functionally disconnected state. This is accomplished via narrow-band optical pumping on the $^2S_{1/2}$ to the $^2D_{5/2}$ quadrupole which has a leaky dipole channel into the $^2F_{7/2}$. Narrow-band optical pumping is again used to rescue the ion at the end of the experiment with the aid of a 760 nm E2 transition back into the cooling cycle. Measurement with this scheme is no longer limited by off-resonant effects from the main cycling transition. Limits of this novel technique, as well as further directions using the F state as a utility for quantum information are explored.

Finally, we combine the pulsed background-free spectroscopy with shelving and demonstrate high-fidelity, background free detection of a single trapped $^{171}Yb^+$ qubit.

The dissertation of Anthony Micheal Ransford is approved.

Eric Hudson

Paul Hamilton

Ni Ni

Wesley C. Campbell, Committee Chair

University of California, Los Angeles

2020

To my wife Val and my dog IO ...

for constant love and support,

every day without fail

Contents

List of Figures . . . . . **x**

List of Tables . . . . . **xv**

Acknowledgments . . . . . **xvi**

Vita . . . . . **xviii**

1 Ion Trapping **3**

1.1 RF Paul traps 3

1.1.1 Mathieu solutions 3

1.1.2 DC Multipoles 6

1.1.3 Micromotion compensation 8

1.2 The Yb^+ ion 9

1.2.1 Bracket states 12

1.2.2 Hyperfine structure 14

1.2.3 $^{174}Yb^+$ 17

1.2.4 $^{171}Yb^+$ 18

1.2.5 $^{173}Yb^+$ 24

2 Atoms and Lasers **26**

2.1 CW Lasers and atoms 26

2.1.1 Dipoles 26

2.1.2 Quadrupoles 29

2.1.3 2-Level systems (qubits) 33

2.1.4 Three Level system (qutrits) . . . 35
2.2 Pulsed Lasers . . . 37
2.2.1 Mode Locked Lasers . . . 37

3 Ions as Qubits . . . 40
3.1 Optical Qubits . . . 40
3.2 Hyperfine Qubits . . . 41
3.3 Zeeman Qubits . . . 41

4 Experimental Setup . . . 42
4.1 Oblate Trap . . . 42
4.1.1 Loading in the oblate trap . . . 44
4.1.2 Oblate trap damage . . . 45
4.2 Lasers . . . 46
4.2.1 The 399 nm Laser . . . 46
4.2.2 The 369 nm laser . . . 46
4.2.3 The 935 nm laser . . . 47
4.2.4 The 411 nm laser . . . 47
4.2.5 The 760 nm lasers . . . 47
4.2.6 The 976 nm laser . . . 48
4.2.7 Laser table . . . 48
4.3 Microwaves . . . 49
4.3.1 12.6 GHz . . . 49
4.3.2 3.6 GHz . . . 49
4.3.3 2.1 GHz . . . 49

4.3.4 7.374 GHz . . . 50
4.4 Electronics . . . 50
4.4.1 The Pulser . . . 50
4.4.2 DACs . . . 51
4.5 Software Control . . . 51
4.5.1 Data Vault . . . 51
4.5.2 Parameter Vault . . . 52
4.5.3 ScriptScanner . . . 52
4.5.4 Experiment structure . . . 52
4.5.5 Sub-sequences . . . 53
4.5.6 Sequences . . . 54
4.5.7 Experiments . . . 55

5 2D Crystals . . . 65
5.1 Configuration simulations . . . 66
5.1.1 Annealing algorithm . . . 66
5.1.2 Metastable Configurations . . . 67
5.2 Hopping between stable and metastable states . . . 69

6 Phonon Lasing . . . 72
6.1 Tsunami TiSaph . . . 72
6.2 Visibility . . . 73
6.3 Phonon lasing . . . 74
6.4 Injection locking . . . 77
6.5 Loading crystals and laser cooling . . . 77

7 Shelving State Detection . . . 79

7.1 Narrow-band optical pumping . . . 79

7.2 Scheme . . . 80

7.3 Limits . . . 80

7.4 Results . . . 85

8 Ultrafast State Detection . . . 92

8.1 Hyperfine . . . 92

8.2 Shelved Hyperfine . . . 95

8.3 Experimental setup . . . 96

8.4 Results . . . 99

9 The F state as a Resource for Quantum Information . . . 103

9.1 A Qubit in the F state . . . 103

9.1.1 State Preparation, Manipulation and Measurement of F state Qubits 103

9.1.2 Driving the F state qubit . . . 104

9.2 Towards Qudits in the F state . . . 105

10 Quantum Networks and the F state of Yb (possible future directions) . 106

10.1 Remote entanglement . . . 107

10.2 Scheme I: $^{171}Yb^{+}$-$^{171}Yb^{+}$ . . . 109

10.3 Scheme II: 171-173 . . . 110

10.4 Scheme III: 173-173 . . . 111

References . . . 114

List of Figures

1.1 Ion motion in the x, y and z directions 6

1.2 Matrix transitioning voltages to multipoles, using symmetry to deduce the vectors (left) and using Comsol to calculate the response to unit voltage applied (right) 8

1.3 Micromotion compensation via minimization of modulation. The ion is moved until no noticeable peaks occur at multiples of the RF drive frequency 10

1.4 Fluorescence detection of neutral Yb atom from atomic source. Detection is done with 3 amps applied to oven for 10 minutes and 10μW of power focused to 30μm diameter 11

1.5 Electronic structure of relevant transitions in $^{174}Yb^{+}$ 17

1.6 Electronic and Hyperfine structure of $^{171}Yb^{+}$ relevant to this thesis 19

1.7 State preparation for the $^{171}Yb^{+}$ qubit. Initial population distribution (left), optical pumping (middle), final prepared state (right) 20

1.8 Population stranded in the F=1 manifold after state preparation. The error rate is less than 1e-5 for typical experimental parameters, s$\sim$ 10 21

1.9 State detection is performed by cycling the $^2S_{1/2}F = 1$ manifold to the $^2P_{1/2}F = 0$ and collecting the resultant state dependent fluorescence 23

1.10 Predicted energy shifts in the $^2F_{7/2}$ hyperfine considering A and B coefficients (upper left) calculated by Itano[49](orange), Flambaum[21](blue) and Di Xiao[1](green). The upper right shows a diagram of the levels and the bottom are allowed magnetic dipole transitions frequencies. 25

2.1 Equation 2.62 plotted for t_r= 12.5 ns and 20 pulses 39

4.1 Solid works diagram of the trap. Inset shows RF ring and access tunnels 42

4.2 Cartoon showing the available solid angle of the trap with the two recessed viewports 56

4.3 Microscope images of the first ring trap damage. The delamination of the gold is circled in red . . . 57
4.4 Current new ring trap microscope images showing full gold coating . . . 58
4.5 Axial secular frequency as a function of applied RF power . . . 58
4.6 Crystal of ions where the axial confinement is too weak and the crystal breaks into a 3-D structure . . . 59
4.7 Composite image taken with EMCCD camera (iXon3). The solid works design is overlaid to show orientation and reflection which changes due to imaging and mirrors . . . 60
4.8 976 nm spectrums. Upper left, F=2 to F=1. Upper right, F=2 to F=2. Bottom F=3 to F=2 . . . 61
4.9 760 nm spectrums. Left, F=3 to F=1. Right, F=4 to F=2. The spectrum is fit to a Bessel modulated Lorentzian . . . 61
4.10 Ion drift rate with before mesh on windows (blue X, orange, Y) and after mesh is installed (green X, red Y) . . . 62
4.11 Laser setup, all lasers are measured on wavemeters and sent through single pass AOMs for switching except for the 399 nm which is shuttered with a hard drive switch. The 369 nm laser is double passed prior to going to the different single pass AOMs for switching. The double pass allows for fast frequency switching as well as slow feedback for cavity drifts. . . . 63
4.12 Power spectral density of noise on a single DC electrode with different filtering. Current operation is done with filters corresponding to the green trace and the bump at 630 MHz is due to electric noise from the ixon EMCCD camera and disappears when communication is removed . . . 64

5.1 Images of trapped ions configurations in our experiment, 1 to 9 . . . 65
5.2 Simulated stable (purple) and metastable (orange) configurations . . . 67

5.3 Potential barrier for configuration of ion dragged along the z axis 68

5.4 6 ion barrier height at different asymmetries 69

5.5 Energy of the face centered pentagon (green) and the hexagon (blue) for different radial trap symmetries 70

5.6 Hopping rate with different asymmetries. We see that with a more symmetric potential (red) the ions stay in the face centered pentagon whereas with large asymmetry (blue) the ions stay in the hexagonal configuration. Near the crossing (green) the temperature of the crystal is large enough to hop between the two configurations 71

6.1 Fluorescence spectrum (in kilocounts per second) from a single trapped ion illuminated by an optical frequency comb. The voltage corresponds to moving the laser cavity and thus scanning the teeth, this repeats every 2V. When the near-resonant tooth is red detuned ∼3.2V, the ion is Doppler cooled near the ground state and the spectrum follows the rest-frame lineshape. When the near-resonant tooth is blue detuned ∼4V, the ion oscillates with a fixed amplitude and the fluorescence shows clear departure from the natural rest-frame resonance shape. 75

6.2 Integrated ion images at various fixed points for the nearest tooth red (top) and blue (bottom) detuned 76

6.3 Acoustic injection locking of the x_1^* fixed point phonon laser when the near-resonant tooth is blue detuned. When the frequency of an injected signal is moved from outside (orange) to within (blue) the phonon laser's gain bandwidth, it is amplified at the expense of other frequencies. 78

7.1 Shelving scheme with the 411 nm laser. Population is transferred on the F=1 $\longrightarrow$ F=3 cycling transition. 81

7.2 Fidelity as function of shelving time. As shelving time is increased the fidelity increases(orange) however eventually the finite lifetime of the $^2F_{7/2}$ state will have a non-negligible effect (blue) and the total fidelity (green) will decrease. 82

7.3 F state population transfer with coherent pi pulse (blue) or incoherent shelving(orange). For the coherent case only 83% population will be transferred and switching to incoherent scheme must happen to achieve full transfer. 84

7.4 S state population transfer. A time constant of 18 ms shows this is very much in line with the theory 86

7.5 Deshelving of the F state manifold with the 760 nm repumpers. Time constants of a few ms are achieved with ≈5mW of power in a 100 μm beam waist. 87

7.6 Zeeman splitting of the $^2S_{1/2}, F = 1 \longrightarrow ^2 D_{5/2}, F = 3$ transition. Detuning is of the red non-doubled light. 88

7.7 Initial measurement of the 411 nm hyperfine interval of the $^2D_{5/2}$ level. The splitting of 190MHz is in line with previous measurements [56] 89

7.8 Rabi flopping on the hyperfine qubit in $^{171}Yb^+$ using the shelving technique . . 90

7.9 High fidelity state preparation and measurement of the hyperfine qubit. Fidelity is measured to be 99.95(4). Note the lack of decays in the region between Poissonians. This is due to the extremely long lived (5.5 yr) F state. 91

8.1 S-P lifetime measurement from ultrafast pulses 93

8.2 Hyperfine structure of $^{171}Yb^+$ (left) showing the transition in blue that we desire to drive and the orange and red transitions which are to be avoided. The right shows the frequency of these transitions relative to the state selective cycling transition (blue) superimposed with the Mach-Zehnder interferometer frequency output. 94

8.3 Scatter counted from the pulses on the TDC. The shape is due to after pulsing of the PMT. The two purple lines are 237 ps apart showing the coarse delay is set properly 95

8.4 Frequency domain of pulses 96

8.5 Experimental setup with Mach-Zehnder interferometer 97

8.6 Ramsey experiment on the three transitions involved, orange is the F=1-F=0 manifold. The fidelity of the oranges is much higher do to the lack of mixing after a single scattered photon. For the other two transitions leakage occurs after a few scattering events 98

8.7 Detection of Rabi oscillation of the hyperfine qubit using the frequency comb . . 100

8.8 Detection of Rabi oscillation of the hyperfine qubit using the frequency comb . . 101

8.9 Detection of Rabi oscillation of the hyperfine qubit using the frequency comb after shelving to the F state 102

9.1 Predicted spectra of the 935 nm transition based on hyperfine coefficients 105

10.1 Structure of $^{171}Yb^{+}$. Frequency-selective driving of the $^{2}S_{1/2}(F = 0)$ states to $^{2}F^{o}_{7/2}(F = 3)$ on the octupole transition will coherently shelve this population. $^{173}Yb^{+}$ structure used in fast excitation and shelving (right) 108

10.2 Three methods of cross-talk free remote entanglement: $^{171}Yb^{+}$-$^{171}Yb^{+}$, (b) $^{171}Yb^{+}$-$^{173}Yb^{+}$ 110

10.3 Ion photon frequency entanglement scheme in $^{173}Yb^{+}$. The ion is optically pumped with pi light (a), microwaves at 10.49GHz drive a superposition of qubit states (b), a mode-locked pulse maps the population (selection rules prevent mixing) (c) and finally the emitted photon color is entangled with the final state of the ion 112

List of Tables

1.1 Yb isotopes and abundances 11

4.1 Transition frequencies measured in our lab. The 369 frequency for 171 is the $^2S_{1/2}$ F=1 to $^2P_{1/2}$ F=0 cooling transition. The 935 for 171 is the $^2D_{3/2}$ F=1 to $^3[3/2]_{1/2}$ F=0 transition. The 411 for 171 is the $^2S_{1/2}$ F=1 to the center of the two hyperfine transitions in the $^2D_{5/2}$. The 760 nm in 171 is the $^2F_{7/2}$ F=3 to $^1[3/2]_{3/2}$ F=1 and $^2F_{7/2}$ F=4 to $^1[3/2]_{3/2}$ F=2 respectively 48

Acknowledgments

I would like to thank my family who have been supportive through all the ups and downs, not only during graduate school but also undergrad and before. My Mom for always talking to me on the way home during my long commutes. I would not have made it through without the love and support of my wife Valerie for dealing with me through all the stress and moving. I could not ask for a better partner to spend my life with. After coming home from long days my dog IO was always there, ready to greet me and make me feel loved.

I was lucky enough to have been in the ion trapping community in undergrad and have had many lab partners who have taught me how important different perspectives are in problem solving. Sebastion Gerber, Nikos Danillidios, Ishan Talukdar and Crystal Noel all guided and struggled along-side me, and I thank them for the physics I learned from them and the preparation they provided me for graduate school. I also could not thank Hartmut enough for mentoring me for years. I learned so much from him and he has helped me immensely even after I left his lab for graduate school.

Wesley C. Campbell: there was not a better graduate advisor for me, truly. Wes constantly challenged me and developed me as a person and a physicist. Perhaps the thing I gained most from him was finding resolution in disagreements. This made me challenge and justify everything. From this I learned what it means to be a scientist. I also learned how to let science find me and use genuine curiosity to guide us to new discoveries. I am forever indebted to Wes for allowing me to be as creative as he has. I have single handedly derailed the experiment for wacky ideas and instead of steering me on some pre-determined path, Wes encouraged me to explore further, and I could not have had a better PhD experience. Thank you, Wes.

I would also like to acknowledge the amazing community of people at UCLA. UCLA atomic physics was filled with brilliant, well communicating people whom I have learned so much from. Each person I could easily write pages about, and this PhD in some way belongs to them as well. Conrad Roman, Michael Ip, Xueping Long, Andrew Jayich and Gary Chen

sat beside me day in and day out and were a huge resource for shared technology and ideas. Eric Hudson, Prateek Puri, Michael Mills taught me about life and CaBaO. Chandler Schlupf and Rob Niederriter taught me about MOTs and broken glass. Randy Putnam and Adam West taught me about gyroscopes, chess and rendering in Blender. Sami Khamis taught me how to relax. Elizabeth West, who has dramatically improved this thesis with editing and was always helpful with physics questions. Finally, the future generation Thomas Dellaert, Patrick McMillin and Changling Zhao. We are very lucky to have such talented new students to take over our experiments and find all the duct tape.

Justin Christensen... what a ride? I can guarantee no physicists have had the pleasure of going to three different schools together and sharing every class and experience, then working next door to each other and collaborating so closely until the end. I could go on and on but we both know how lucky we are.

Finally, thanks to Dylan Gorman for being smarter than me (Amanda says so) and being a great friend. I couldn't have done it without you bud.

Vita

2009–2011	A.A. , Moorpark College
2011–2013	B.A. (Physics), Physics Department, UC Berkeley.
2014–2020	Student Graduate Researcher, Physics Department, UCLA.

Publications

Roman, Conrad, Anthony Ransford, Michael Ip, and Wesley C. Campbell. 2019. "Coherent Control for Qubit State Readout," November. http://arxiv.org/abs/1911.10138

Vutha, Amar C., Eliot A. Bohr, Anthony Ransford, Wesley C. Campbell, and Paul Hamilton. 2018. "Displacement Operators: The Classical Face of Their Quantum Phase." European Journal of Physics 39 (2).

Ip, Michael, Anthony Ransford, Andrew M. Jayich, Xueping Long, Conrad Roman, and Wesley C. Campbell. 2018. "Phonon Lasing from Optical Frequency Comb Illumination of Trapped Ions." Physical Review Letters 121 (4).

Li, Hao Kun, Erik Urban, Crystal Noel, Alexander Chuang, Yang Xia, Anthony Ransford, Boerge Hemmerling, et al. 2017. "Realization of Translational Symmetry in Trapped Cold Ion Rings." Physical Review Letters 118 (5).

Daniilidis, N., S. Gerber, G. Bolloten, M. Ramm, A. Ransford, E. Ulin-Avila, I. Talukdar, and H. Häffner. 2014. "Surface Noise Analysis Using a Single-Ion Sensor." Physical Review

B - Condensed Matter and Materials Physics 89 (24).

Introduction

Standard computers have changed every part of society and revolutionized medicine, engineering, design and social interactions. These computers are based on an approximation of a classical world. However, the world is not classical it is quantum, and Richard Feynman famously noted that if we wanted to simulate the world, we would need a quantum version of a computer[23]. This quantum computer would use physical systems such as spins to store and manipulate information following the rules of quantum mechanics. This idea was endowed with more rigor through the 1980's with the development of gate-based quantum computing theory and the formal definition of a Quantum Turing Machine[8]. These endeavors, much like the computational devices of the early part of the 20th century, were academic in nature. The quantum computing revolution truly began in 1997 when Peter Shor published his factoring and discrete logarithm algorithms for a quantum computer[61]. Since current encryption algorithms based on RSA (Rivest–Shamir–Adleman)[53] leverage the fact that factoring is thought to be a (NP) hard problem, the possibility of breaking public-key encryption has generated much excitement around quantum computing. Other useful algorithms have also been developed, such as Grovers search algorithm of an unsorted database [26] and an algorithm for finding solutions to systems of linear equations [28].

David DiVincenzo laid out a set of criteria[20] for what would constitute a scaleable quantum computer potentially capable of running these and other useful algorithms. These criteria included the ability to create and control a well-defined quantum state, the ability to couple multiple qubits to perform arbitrary rotations and the ability to measure these qubits. Cirac and Zoller showed that chains of ions with laser-controlled transitions could meet these requirements[15]. Since 1995 much effort has gone into pushing trapped ion technology to the level of a fully programmable quantum computer. At the moment we are still in the infancy of this endeavor, with much to learn. Current systems are noisy and difficult to control. John Preskill has dubbed this the NISQ (Noisy Intermediate Scale Quantum device) era[50]. This era is marked by a lack of error correcting protocols and systems sizes which only brush

the surface of quantum capabilities. In this era extra effort must be spent on increasing both gate fidelity and state preparation and measurement fidelity, as the error rates with both gate width and depth will grow exponentially.

In this thesis we will show how ultra-fast pulses and complicated atomic structure can be leveraged to expand the toolbox of quantum information allowing for very high fidelity state preparation and measurement in a background-free way.

CHAPTER 1

Ion Trapping

1.1 RF Paul traps

The first step in performing quantum information tasks on trapped ions is levitating the ions in an isolated vacuum chamber so the environment does not affect the state of the atoms. Charged particles cannot be trapped in static fields due to Earnshaw's theorem. Instead we use radio frequency (RF) electric fields to confine the ion dynamically. The theory of which is as follows.

1.1.1 Mathieu solutions

The force on a charged particle can be written as

$$\vec{F_e} = Q\vec{E}(\vec{x}, t) \tag{1.1}$$

With Q being the net charge of the particle. The electric field can be described by the gradient of a potential

$$\vec{E}(\vec{x}, t) = -\nabla\Phi(\vec{x}, t) \tag{1.2}$$

then generally the equations of motion are

$$m\ddot{\vec{x}} = -Q\nabla\Phi(\vec{x}, t) \tag{1.3}$$

The potential can be expanded in spherical harmonics that are regular at the origin with time dependent coefficients[36]

$$\Phi(\vec{x},t) = \sum_{l,m} A_l^m(t) Y_l^m(\theta,\phi) r^l \tag{1.4}$$

the $l = 0$ case corresponds to a global offset to the potential which has no physical relevance. The $l = 1$ gives the linear terms while the $l = 2$ gives the quadratic terms. Taking the potential to be real and choosing convenient names for the expansion coefficients, Explicitly:

$$\begin{aligned}\Phi = E_x x + E_y y + E_z z + \\ M_1 xy + M_2 yz + M_3(2z^2 - x^2 - y^2) + M_4 zx + M_5(x^2 - y^2)\end{aligned} \tag{1.5}$$

By choosing electrodes whose surface corresponds to an equipotential of the quadrupole term (M_3) and assuming the coefficient is a sum of a harmonic time dependent part and DC part the potential becomes

$$\Phi = (V\cos(\Omega_{RF} t) + V_0)(\frac{2z^2 - x^2 - y^2}{r_0^2}) \tag{1.6}$$

where V is the RF amplitude, Ω_{RF} is the drive frequency and r_0 is a characteristic length. Plugging this into equation 3.

$$m\ddot{\vec{x}} = -Q\boldsymbol{\nabla}\Big((V\cos(\Omega_{RF} t) + V_0)(\frac{2z^2 - x^2 - y^2}{r_0^2})\Big) \tag{1.7}$$

or

$$\ddot{\vec{x}} = -\frac{2Q}{mr_0^2}\Big[V\cos(\Omega_{RF} t) + V_0\Big]\alpha_i x_i \tag{1.8}$$

where the dependent constant α_i satisfies Laplace's equation $\nabla^2\Phi = 0$

$$\alpha_x = \alpha_y = -\frac{\alpha_z}{2} = -1 \tag{1.9}$$

furthermore we can make the substitution $\xi = \frac{\Omega_{RF}t}{2}$ and $u = \frac{x_i}{r_0}$ to arrive at the canonical form of the Mathieu equations[43]

$$\ddot{u}_i + (a_i - 2q_i\cos(2\xi))u_i = 0 \tag{1.10}$$

along with the definitions

$$a_i = \frac{8\alpha_i QV_0}{mr_0^2\Omega_{RF}} \tag{1.11}$$

$$q_i = \frac{4\alpha_i QV}{mr_0^2\Omega_{RF}} \tag{1.12}$$

The bounded first order Mathieu solutions are[25]

$$x_i(t) \approx cos(\omega_i t)[1 - \frac{q_i}{2}cos(\Omega_{RFt})] \tag{1.13}$$

With the definitions

$$\omega_i = \frac{\beta_i\Omega_{RF}}{2} \tag{1.14}$$

and

$$\beta_i = \sqrt{\frac{q_i^2}{2} + a_i} \tag{1.15}$$

Equation 1.13 is plotted with parameters used in trapping during this thesis.

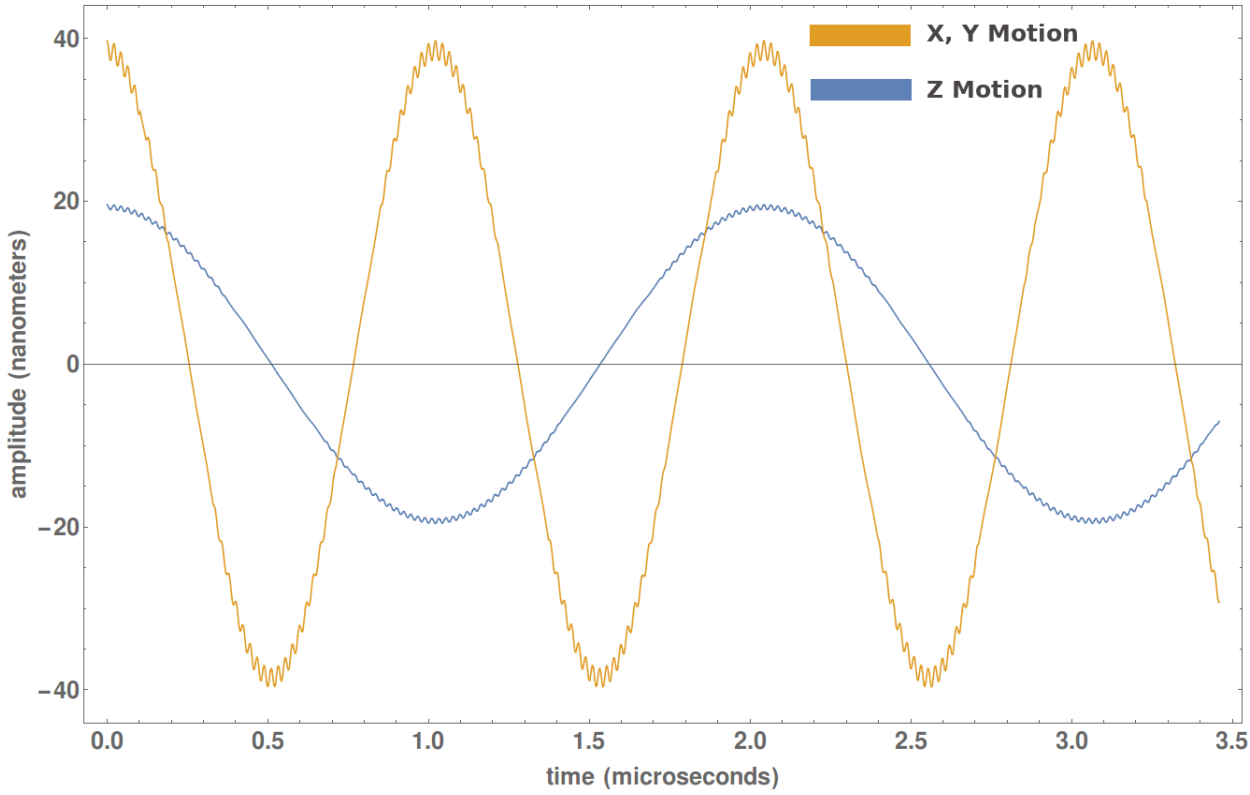

Figure 1.1: Ion motion in the x, y and z directions

1.1.2 DC Multipoles

In the previous section we assumed that the electrodes used to trapped ions were surfaces of hyperbole, this usually is an exaggerated statement not meant to be taken literally. In practice ion traps have imperfect geometries intentionally to allow things like imaging and laser access. Beyond these defects there are also known charging effects that cause stray electric fields at the ions position.

In order to trim out the stray fields and have control over the ion we would like control knobs for all the coefficients in equation 2.5. For this reason (8) extra DC electrodes are placed near the RF electrode to allow application of DC manipulation fields. When a potential is applied to a single arbitrary electrode the potential at the ion can be written in

the form

$$\Phi_1 = E_x^1 x + E_y^1 y + E_z^1 z + M_1^1 xy + M_2^1 yz + M_3^1(2z^2 - x^2 - y^2) + M_4^1 zx + M_5^1(x^2 - y^2) + ... \tag{1.16}$$

In our case we have 8 electrodes and the potential is simply a sum of these

$$\Phi_{DC} = \sum_{i=1}^{8} \Phi_i \tag{1.17}$$

It is desirable to control each total coefficient as apposed to controlling a voltage and generating all coefficients. To do this we need an invertible map between control voltages and multipole values. such that

$$M\vec{\Phi} = \vec{m} \tag{1.18}$$

where $\vec{\Phi}$ is the vector of applied DC voltages and M is a matrix whose size is determined by the number of available electrodes (8x8 in our case) and $\vec{m}$ is the coefficients applied to each multipole.

The goal is now to find M^{-1} such that

$$M^{-1}\vec{m} = \vec{\Phi} \tag{1.19}$$

Allowing the experimenter to pick a multipole value and retrieve the required voltages to apply that multipole. While a precise calculation of this matrix was performed by numerical methods in a finite element boundary solver (ComSol) the matrix can be essentially intuited by symmetry of the electrodes. See figure 1.2 for a visualization of the multipole calculation both in ComSol and by symmetry arguments. Note that M6 which corresponds to the xy

multipole has nearly no projection. This is due to the high degree of symmetry for the DC electrodes and could be remedied in future designs with more arbitrary electrodes.

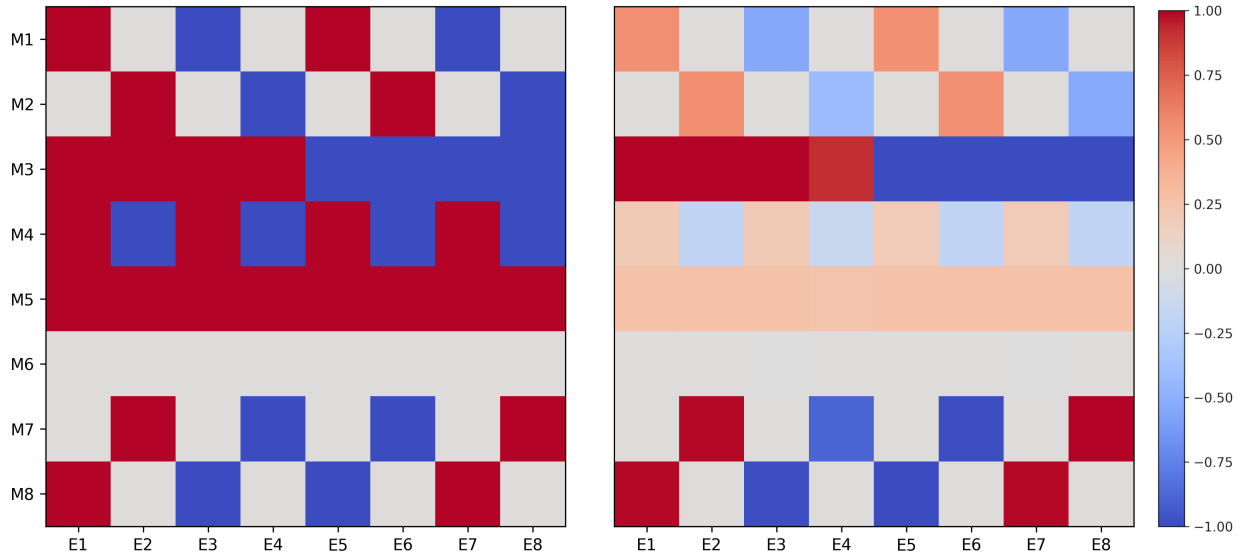

Figure 1.2: Matrix transitioning voltages to multipoles, using symmetry to deduce the vectors (left) and using Comsol to calculate the response to unit voltage applied (right)

1.1.3 Micromotion compensation

While for small displacements of the ion the potential it sees is nearly harmonic, it is not exact. There is in fact intrinsic micromotion due to the finite wave packet size of the atom as well as excess micromotion from the ion being displaced from the trap null due to stray electric fields. We will consider only the excess micromotion caused by stray fields. These stray fields need to be compensated to reduce heating and increase ion lifetime.

Equation 2.10 can be modified to include a constant electric field

$$\ddot{u}_i + (a_i - 2q_i\cos(2\xi))u_i = \frac{Q}{m}\vec{E}\cdot\vec{x}_i \tag{1.20}$$

The equations of motion now become phase modulated (see Berkeland et. al.[11]) at the

micromotion frequency and the time averaged excited state population can be written as

$$P_e = A(E_0)^2 \sum_{n=-\infty}^{\infty} \frac{J_n^2(\beta)}{(\omega_{atom} - \omega_{laser} + n\Omega)^2 + (\frac{\gamma}{2})^2} \tag{1.21}$$

where $A(E_0)$ is an amplitude of the laser and ground and excited state coupling. J_n is the nth order Bessel function, γ is the excited state lifetime and beta is the modulation depth defined in this case as

$$\beta = \frac{1}{2}|k_i u_{0i} q_i| \tag{1.22}$$

with k being the laser wave vector and u_{oi} being the displacement in the ith direction. The main takeaway is that the modulation depth increases linearly with distance from the center of the trap and requires laser projection in the direction of the motion to observe. This leads us to a method of micro-motion compensation that is most used in our setup. The modulation depth is measured via a linescan of the cooling transition and the modulated sidebands are minimized. Figure 1.3 shows extreme modulation far from the null as a function of distance.

1.2 The Yb^+ ion

An ideal ion to work with would be one with a closed cycling transition and who's structure is amenable to the DiVencenzo criteria of state preparation and manipulation of a qubit. While singly ionized alkaline earth metals are a good choice, they are not the only ones. Any atom with a closed S orbital and filled P, D and F shells can be used. This means we can add to our list of hydrogen like ions; Zn^+, Cd^+, Hg^+, He^+, No^+, and Yb^+. Surprisingly

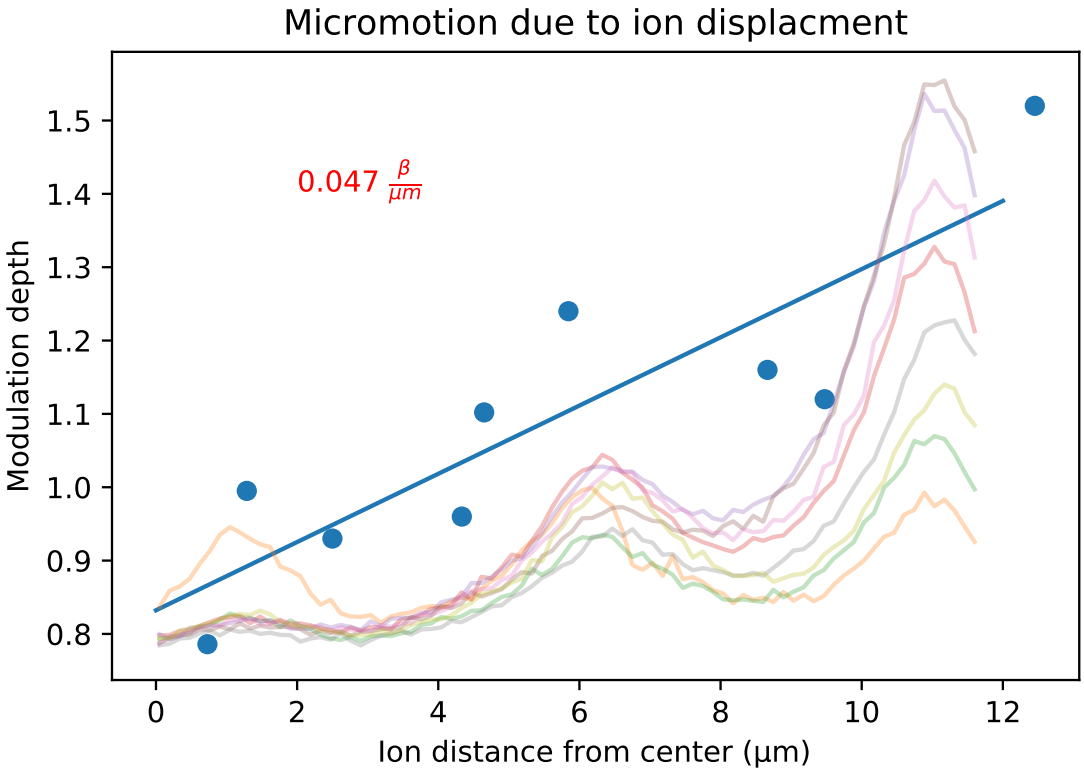

Figure 1.3: Micromotion compensation via minimization of modulation. The ion is moved until no noticeable peaks occur at multiples of the RF drive frequency

when you consider all these along with the alkaline earth metals only Hg^+, Cd^+ and Yb^+ have the desirable spin-1/2 stable isotope. Unfortunately, the cycling transitions for Hg^+ and Cd^+ are deep in the UV (194 nm and 226 nm respectively). Fortunately, Yb^+ exhibits a cycling transition near 369 nm which is available in a diode (NDU1113E) or at the center of a standard doubled Titanium Sapphire laser. For this reason, we, along with many other groups, have chosen Yb^+ as our ion for quantum information.

Ytterbium has seven stable isotopes[14] (see table 1.1) of which we have laser cooled atomic masses 174, 172, 176, 173 and 171. We primarily use the even isotopes for diagnostics and experiments that do not require a qubit. $^{171}Yb^+$ is the quintessential Yb trapped ion qubit and we use this for nearly all the quantum information experiments described in this thesis. $^{173}Yb^+$ has some very interesting nuclear and quantum information applications.

Some of these future experiments will be described in this thesis.

Isotope (AMU)	Abundance	Nuclear spin
168	0.126%	0
170	3.023%	0
171	14.216%	$\frac{1}{2}$
172	21.754%	0
173	16.098%	$\frac{5}{2}$
174	31.896%	0
176	12.887%	0

Table 1.1: Yb isotopes and abundances

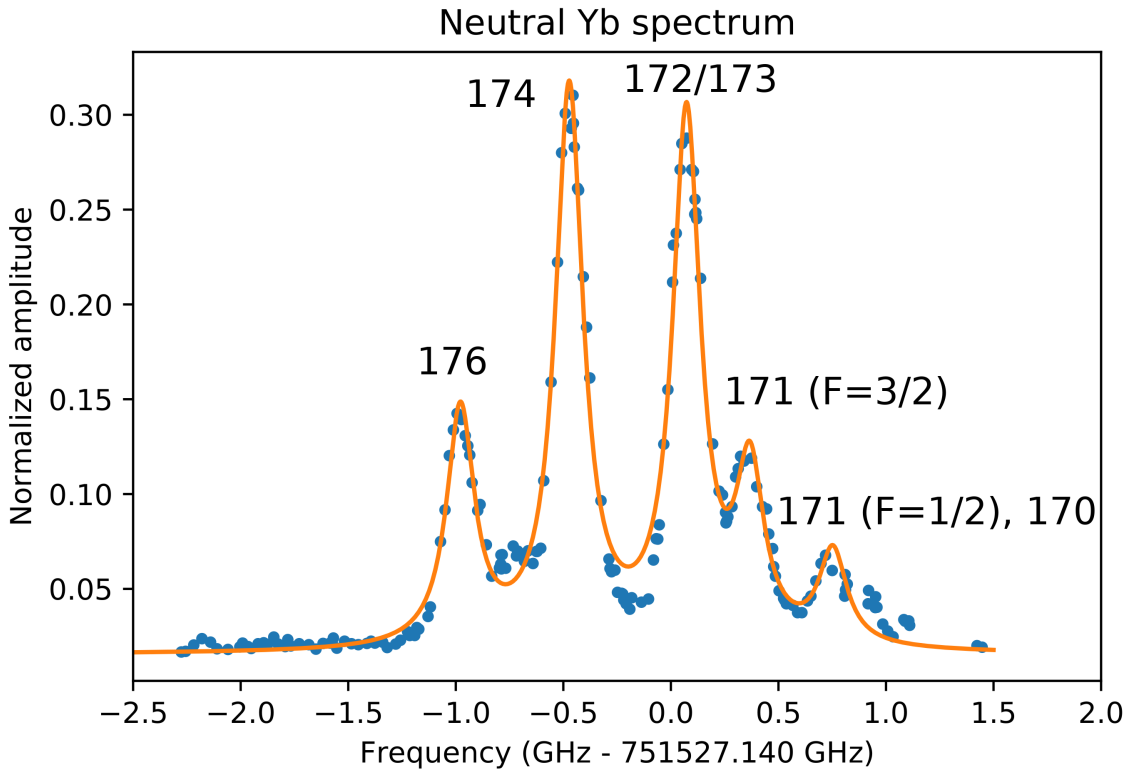

Figure 1.4: Fluorescence detection of neutral Yb atom from atomic source. Detection is done with 3 amps applied to oven for 10 minutes and 10μW of power focused to 30μm diameter

1.2.1 Bracket states

Working with a hydrogen like atoms means that all electrons in the core fill their respective shells. In Yb the highest filled core shell is $4f^{14}$. Normally we would ignore the core and assume the single valence electron has spin 1/2 and quantum numbers $\vec{L}$ and $\vec{S}$ and calculate the total angular momentum of this electron via the normal way ($\vec{J} = \vec{L} + \vec{S}$) and implement spin-orbit coupling (Russel-Saunders) as a perturbation ($\vec{L} \cdot \vec{S}$). This leads to a term symbol

$$^{2S+1}L_J \tag{1.23}$$

where S is the spin of the valence electron(s) (1/2 in our case), L is the orbital angular momentum (S = 0, P=1, D=2, F=3, G=4, H=5, I=6 ...) and J is the total angular momentum ($\vec{L} + \vec{S}$).

This would be the end of the story except in Yb^+ it is possible to excite a core electron from the $4f^{14}$ shell at an energy much lower than the second ionization energy (12 eV corresponding to 101.1 nm). When this core electron is excited it has its own spin and angular momentum and the left behind hole in the core leaves a shell with orbit and spin angular momentum. This leads to new ways to couple angular momentum beyond the standard LS coupling. There are three other non-LS coupling schemes: jj, LK and J_1K. In Yb the bracket states are due to the J_1K coupling scheme while the so-called parenthesis states are the jj coupling scheme.

For the standard LS coupling the orbital angular momentum of the core (l_c) is added to the orbital angular momentum of the orbital (l_o) and the spin of the core (s_c) is added to the orbital spin (s_o) and these are added separately to form the total angular momentum.

$$L = l_c + l_o \tag{1.24}$$

$$S = s_c + s_o \tag{1.25}$$

$$J = L + S \tag{1.26}$$

The coupling scheme for J_1K is

$$J_c = l_c + s_c \tag{1.27}$$

$$K = J_c + l_o \tag{1.28}$$

$$J = K + s_o \tag{1.29}$$

And finally, for jj coupling:

$$J_c = l_c + s_c \tag{1.30}$$

$$J_o = l_o + s_o \tag{1.31}$$

$$J = J_c + J_o \tag{1.32}$$

The term symbols for all schemes are

$$\text{LS coupling} \longrightarrow {}^{2S+1}L_J$$
$$\text{J}_1\text{K coupling} \longrightarrow {}^{2s_0+1}[K]_J$$
$$\text{jj coupling} \longrightarrow (J_1, J_2)_J$$

While you can express any state as a sum of eigenstates in another basis (such as J_1K in the LS basis) the utility of this is limited. For all these schemes the total angular momentum J and the parity are good quantum numbers. From this it can be deduced that a state such

as $^3[3/2]_{1/2}$ which is odd with total angular momentum J=1/2 will behave like a $^2P_{1/2}$ with similar E1 and E2 couplings. This is why that state in particular is used to repump Yb^+ during cooling at 935 nm as it decays primarily to the ground state via an E1 transition.

1.2.2 Hyperfine structure

For all odd isotopes of Yb the nucleus has a net spin that couples to the electrons and leads to hyperfine structure based on the relative orientation of nuclear spin to the electron spin. Following [24], The Hamiltonian for the hyperfine interaction is

$$H_{HFS} = -\vec{\mu}_I \cdot \vec{B}_e \tag{1.33}$$

where $\vec{\mu}_I$ is the magnetic moment of the nucleus and is related to the nuclear spin by

$$\vec{\mu_I} = g_I \mu_N \vec{I} \tag{1.34}$$

where g_I is the nuclear g-factor and μ_N is the Bohr magneton times the mass ratio of the electron to proton and $\vec{I}$ is the nuclear spin. $\vec{B}_e$ is the magnetic field generated by the orbiting electron. Generally speaking, $\vec{B}_e$ will depend on the electronic wave function magnitude at the nucleus and the angular momentum of the electron. We can lump all scalars into a coupling constant and write the interaction as

$$H_{HFS} = A\vec{I} \cdot \vec{J} \tag{1.35}$$

where A is the coupling coefficient and is determined experimentally. This coupling demotes both the projections m_I and m_J from being good quantum numbers and instead the eigenstates of H_{HFS} will be $|IJFm_F\rangle$. We can now write the energy in terms I, J and F

as

$$E_{HFS} = \frac{A}{2}\{F(F+1) - I(I+1) - J(J+1)\} \tag{1.36}$$

I and J are fixed for a given fine structure manifold and this leads to the interval rule for hyperfine structure where

$$E_F - E_{F-1} = AF \tag{1.37}$$

While the magnetic Dipole interaction given by equation 1.33 is usually sufficient especially in ground states with low angular momentum (J) where the 2^k-pole moment only interacts with $J \geq \frac{k}{2}$, Higher order affects can drastically alter the structure in some ion[21]. We will follow the analysis of Beloy and Derevianko[7] for higher order moments of the hyperfine interaction.

The Hamiltonian describing this interaction can be written as the product of two irreducible spherical tensors, one corresponding to the nucleus and one corresponding to the electron.

$$H_{HFI} = \sum_{k,\mu} (-1)^{\mu} T^e_{k,\mu} T^n_{k,-\mu} \tag{1.38}$$

where $T^e_{k,\mu}$ and $T^n_{k,\mu}$ are spherical tensors of rank k that act on the electronic coordinates and nuclear space respectively. Like in the simple example of magnetic dipole interactions, the basis states need to involve new quantum numbers F, m_F. Writing these in the unperturbed basis:

$$|\gamma I J F M_F\rangle = \sum_{M_J, M_I} C^{FM_F}_{JM_J;IM_I} |\gamma J M_J\rangle |I M_I\rangle \tag{1.39}$$

where $C^{FM_F}_{JM_J;IM_I}$ are the Clebsch-Gorden coefficients. For fixed I and J, F is allowed to be in the range of $|J-I| \leq F \leq J+I$. This means the unperturbed levels split into 2J+1 levels

if $J < I$ or $2I + 1$ levels if $J \geq I$. The first order perturbations are given by the diagonal elements of

$$\langle \gamma' I' J' F' M'_F | \sum_{k,\mu} (-1)^{\mu} T^e_{k,\mu} T^n_{k,-\mu} | \gamma I J F M_F \rangle \tag{1.40}$$

and are given by

$$\sum_k X_k(IJF) \langle T^e_k \rangle_J \langle T^n_k \rangle_I \tag{1.41}$$

where

$$X_k(IJF) = (-1)^{I+J+F} \frac{\begin{Bmatrix} F & J & I \\ k & I & J \end{Bmatrix}}{\begin{pmatrix} J & k & J \\ -J & 0 & J \end{pmatrix} \begin{pmatrix} I & k & I \\ -I & 0 & I \end{pmatrix}} \tag{1.42}$$

This energy shift can be parameterized in terms of the so-called A (magnetic-dipole), B (electric-quadrupole), C (magnetic-octupole), D (electric-hexadecapole) and E (magnetic-dotriacontapole) coefficients as

$$\Delta E_{HFS} = AIJX_1(I,J,F) + \frac{B}{4} X_2(I,J,F) + CX_3(I,J,F) + DX_4(I,J,F) + EX_5(I,J,F) \tag{1.43}$$

It should be noted that these are the coefficients for the first order perturbation and decrease as the multi-pole increases. Second order perturbation or higher may be necessary for small coefficients.

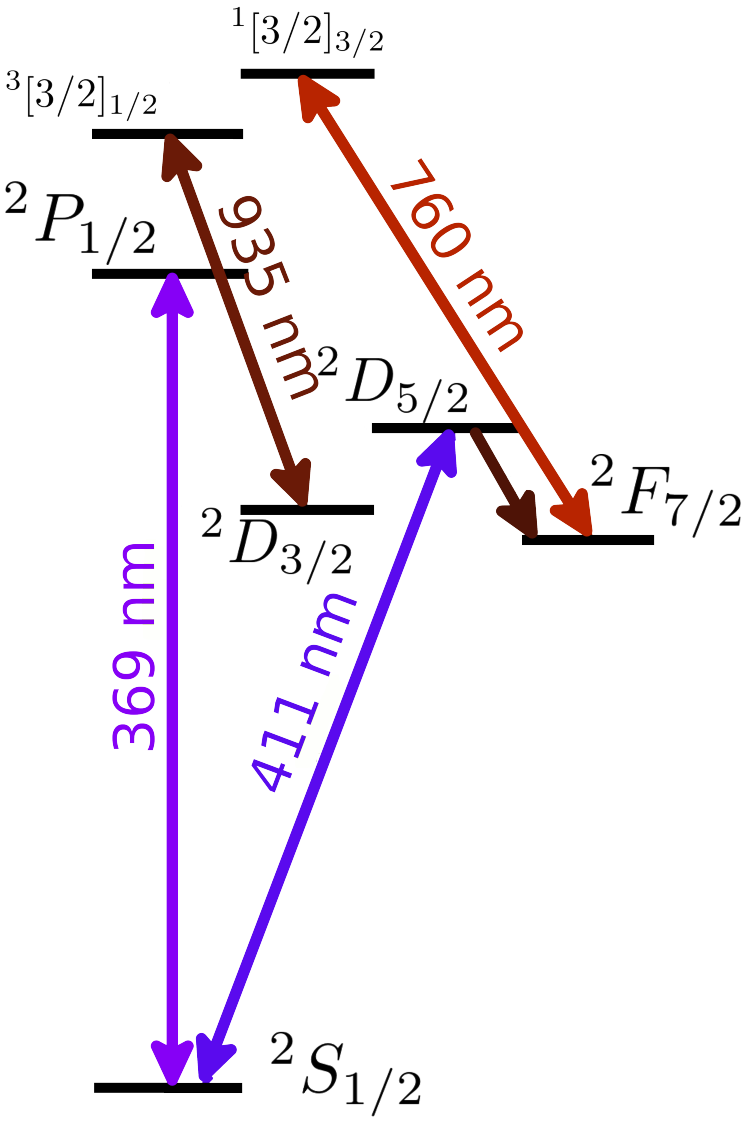

Figure 1.5: Electronic structure of relevant transitions in $^{174}Yb^+$

1.2.3 $^{174}Yb^+$

The most abundant Yb isotope is $^{174}Yb^+$ and happens to have the simplest structure. The relevant transitions are shown in 1.5. Due to this simplicity we use $^{174}Yb^+$ as a diagnostic ion and for experiments that do not require a qubit. There are two distinct features that should be noted, first the low lying $^2F_{7/2}$ which corresponds to the promotion of a core electron to the S orbital. This state provides a dipole decay path for the $^2D_{5/2}$ state at 3.4um. Secondly note the utility of just a couple of bracket states used as repumpers. The 935 nm repumps the

$^2D_{3/2}$ and the 760 nm repumps the $^2F_{7/2}$ via the $^1[3/2]_{3/2}$. These auxiliary states provided repumping without the complication of electromagnetically induced transparency (EIT). It should also be noted that the plethora of available bracket states allow many different repumping levels. The ones used are chosen for historic and technical reasons.

1.2.4 $^{171}Yb^+$

The most used isotope for quantum information is $^{171}Yb^+$. There are many attractive features, one being the microwave frequency 12.6 GHz clock transition on which the qubit is defined, however many ions with nuclear spin (I > 0) can define a first order Zeeman insensitive qubit. What separates $^{171}Yb^+$ is that it is exactly spin (I = 1/2) which gives the ground state manifold a singlet level (F=0). This singlet level allows for fast, extremely efficient incoherent preparation of a pure state in the qubit basis. Furthermore, dipole selection rules forbidding $F = 0 \longrightarrow F = 0$ transitions allow for repeated cycling of the F=1 manifold without mixing the basis states. In the following we describe how state preparation, manipulation and measurement are performed on a single $^{171}Yb^+$ qubit

1.2.4.1 State Preparation

An ion that has just been loaded, laser cooled, or that has just finished some other manipulation will tend to be in an unknown state somewhere in the $^2S_{1/2}$ manifold. This is true as long as sufficient time has been given for the excited $^2P_{1/2}$ to decay (many time constants where $\tau = 8.12$ ns and all metastable states are sufficiently depopulated). The goal is to prepare the pure quantum state $|^2S_{1/2}, F = 0\rangle \equiv |0\rangle$ This is accomplished by applying 369 nm light resonant between the $^2S_{1/2}$ $F = 1 \longrightarrow^2 P_{1/2}$ $F = 1$ manifolds. The steady state solution will find the population in the desired pure state with high probability. The scattering rate for an atomic transition is giving by a Lorentzian as follows[45]

$$\mathrm{R} = \frac{\Gamma}{2}\frac{s}{1 + s + (\frac{2\delta}{\Gamma})^2} \tag{1.44}$$

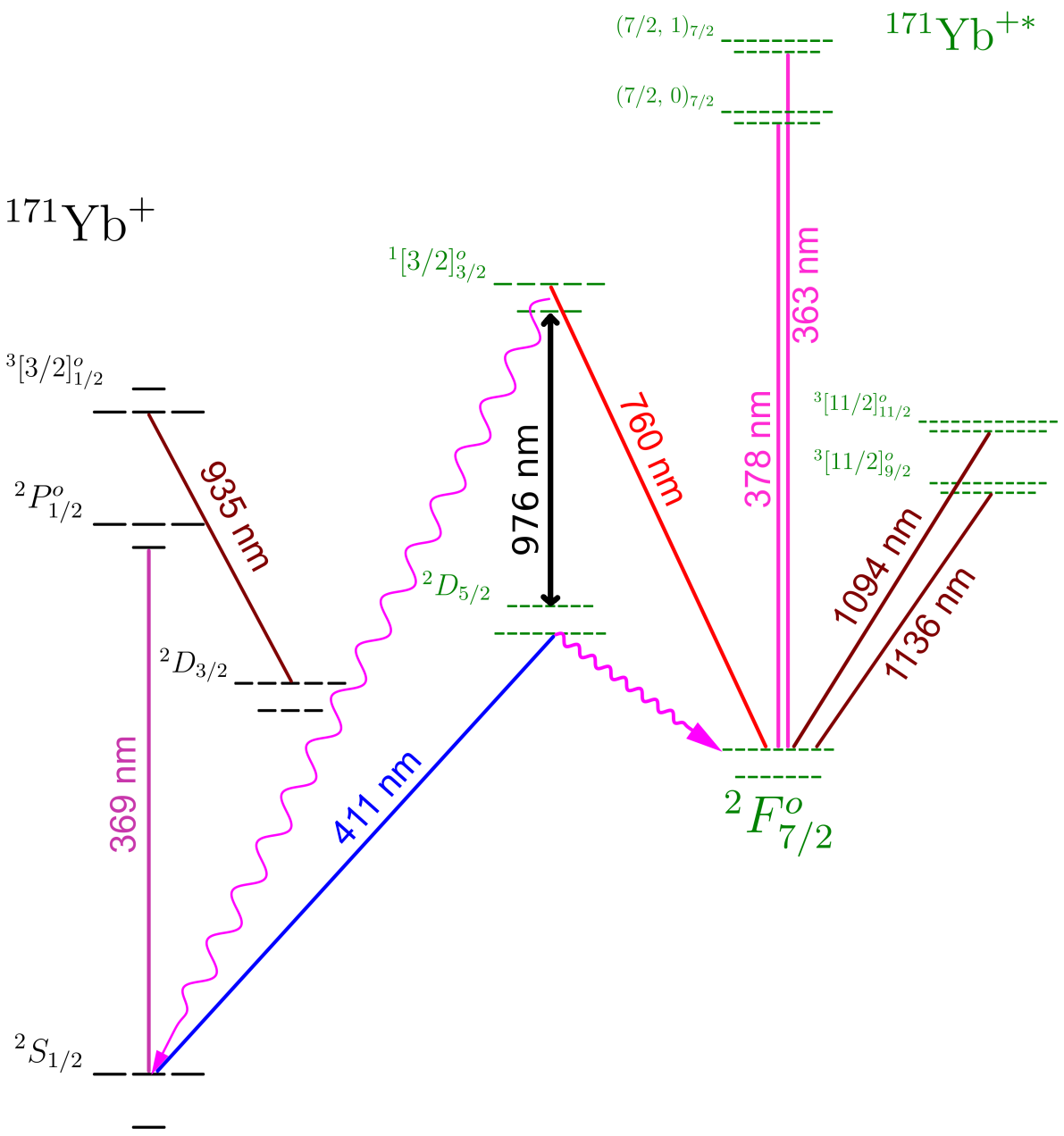

Figure 1.6: Electronic and Hyperfine structure of ^{171}Yb^{+} relevant to this thesis

where $\Gamma = \frac{1}{\tau}$ and s is the saturation parameter defined as

$$s \equiv \frac{2\Omega^2}{\Gamma^2} = \frac{I}{I_s} \tag{1.45}$$

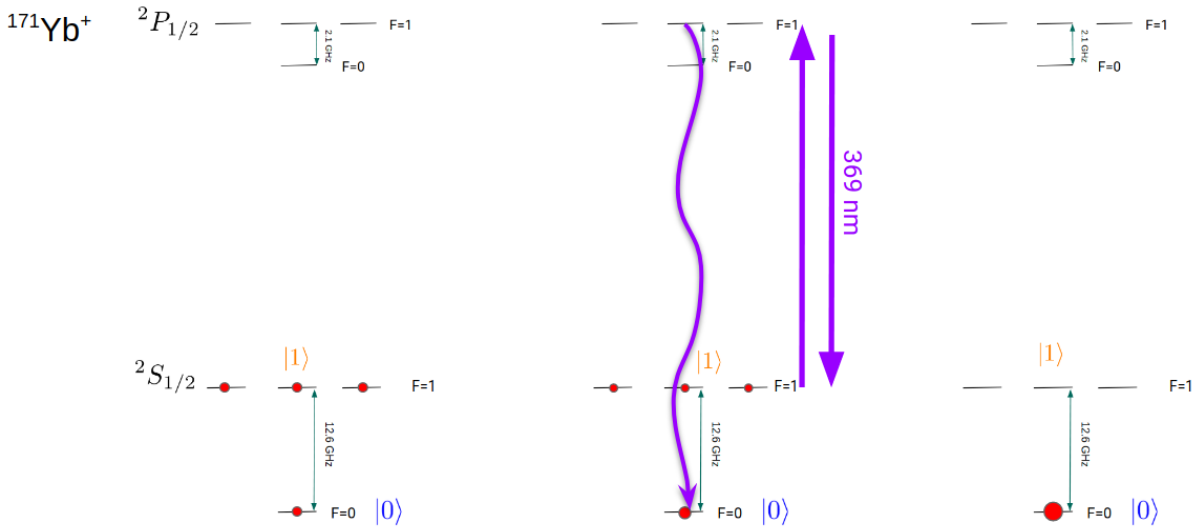

Figure 1.7: State preparation for the $^{171}Yb^{+}$ qubit. Initial population distribution (left), optical pumping (middle), final prepared state (right)

I is the light field intensity and

$$I_s \equiv \frac{\pi h c}{3\lambda^3 \tau} \tag{1.46}$$

with λ being the wavelength of the transition. I_s for Yb^{+} is 512 W/m^2

In order to find out the steady state population in the $|^2S_{1/2}, F = 0\rangle$ state we need to compare the rate in ($\delta = 0$) to the rate out. The rate out is caused by off resonant scatter on the $|^2S_{1/2}\ F = 0\rangle \longrightarrow^2 P_{1/2}$ (F = 1) manifold which can decay to the $2S_{1/2}$ (F = 1) manifold. The detuning for this error process is 14.747 GHz. Using equation 1.33 and taking the ratio of these rates we find that the population stranded in the F=1 manifold after allowing excited decays and taking into account Clebsch-Gordon coefficients is

$$\epsilon = \frac{2(1+s)}{1+s+(\frac{2\delta}{\Gamma})^2} \tag{1.47}$$

The factor of 2 in the numerator is due to the branching ratio of the $^2P_{1/2}$ $F = 1$, (1/3 goes to F=0, 2/3 goes to F=1). The error rate is plotted in figure 1.8

In practice a separate laser from other operations is not used and instead a sideband is applied to a carrier frequency at the 2.105 GHz. A subtlety to this is that the carrier can optically pump the atom dark without the sideband however with a much worse steady state rate $\sim (\frac{\delta_c}{\delta_{op}})^2 \sim 0.02$. For this reason, it is crucial for high fidelity to choose an EOM modulation depth that depletes the carrier as this residual error can creep in.

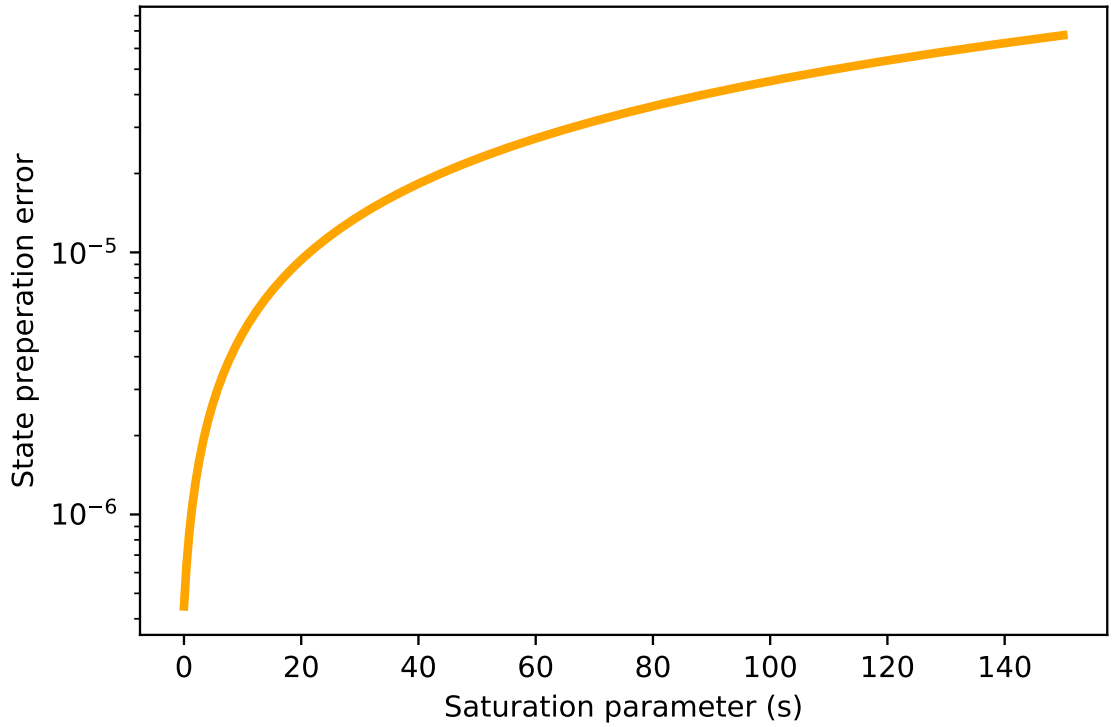

Figure 1.8: Population stranded in the F=1 manifold after state preparation. The error rate is less than 1e-5 for typical experimental parameters, s$\sim$ 10

1.2.4.2 Qubit Manipulation

Superpositions of states are generated with microwaves near 12.6 GHz with a microwave horn 10 inches from the ion. With a solid state minicircuits ZVE-3W-183+ amplifier generating 3W of power we achieve Rabi frequencies on the order of 25kHz.

The two-level Hamiltonian with an oscillating microwave interaction can be written as

$$H = \vec{\mu} \cdot \vec{B} cos(\omega t) \tag{1.48}$$

using Shrödingers equation $i\hbar \frac{\partial |\Psi\rangle}{\partial t} = H |\Psi\rangle$ with $|\Psi\rangle = c_a(t) e^{-i\omega_0 t} |g\rangle + c_b(t) e^{i\omega_0 t} |e\rangle$ and $\Omega = \frac{\langle g|\vec{\mu}\cdot\vec{B}|e\rangle}{\hbar}$

$$i\dot{c_a} = \Omega \cos(\omega t) e^{-i\omega_0 t} c_b \tag{1.49}$$

and

$$i\dot{c_b} = \Omega^* \cos(\omega t) e^{i\omega_0 t} c_a \tag{1.50}$$

after throwing away the sum frequencies (RWA), these can be decoupled in the usual way by taking derivatives, yielding

$$\frac{d^2 c_b}{dt^2} + i(\omega - \omega_0)\frac{dc_b}{dt} + \left|\frac{\Omega}{2}\right|^2 c_b = 0 \tag{1.51}$$

taking $c_1(t=0) = 1$ and $c_2(t=0) = 0$ the excited state population with time is

$$\left|c_b(t)\right|^2 = \frac{\Omega}{\sqrt{\Omega^2 + \Delta^2}} \sin^2\Big(\frac{\Omega}{\sqrt{\Omega^2 + \Delta^2}} \frac{t}{2}\Big) \tag{1.52}$$

for $\Delta = 0$

$$\left|c_b(t)\right|^2 = \sin^2\Big(\frac{\Omega t}{2}\Big) \tag{1.53}$$

This along with phase control of the microwaves allows for arbitrary placement of a single qubit along the Bloch sphere.

1.2.4.3 State detection (measurement)

After a rotation is completed a projective measurement must be made to determine the state of the qubit. The standard way to do this in Yb^+ is to connect the F=1 manifold in the $^2S_{1/2}$ to the F=0 state in the $^2P_{1/2}$ see figure 1.9. An excitation of this transition will lead to an emitted photon and the atom will remain in the F=1 manifold due to the selection rule $F = 0 \longrightarrow F = 0$ being disallowed. This allows for many cycling events to produce many photons if the atom was in the $|1\rangle$ state and zero photons if the atom was in the $|0\rangle$ state. However, unlike optical pumping the hyperfine splittings are not negligible.

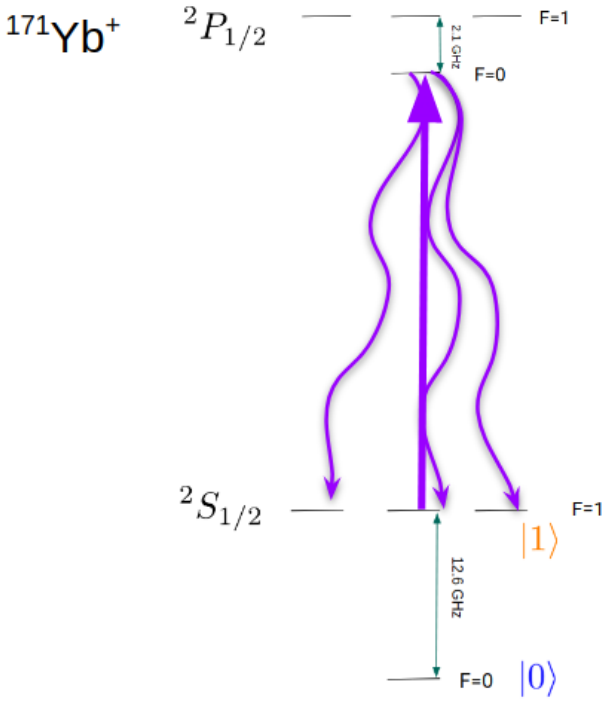

Figure 1.9: State detection is performed by cycling the $^2S_{1/2}F = 1$ manifold to the $^2P_{1/2}F = 0$ and collecting the resultant state dependent fluorescence

The main error occurs from scattering off the $^2P_{1/2}$ F=1 transition which can decay into the $^2S_{1/2}$ F=0 level causing an initially bright ion to become prematurely dark. This state

is 2.105 GHz detuned and the off resonant to on resonant rate ratio from eq 1.33 is

$$\epsilon = \frac{1}{2}\frac{(1+s)}{1+s+(\frac{2\delta}{\Gamma})^2} \tag{1.54}$$

the zero-saturation error in this is 2.26×10^{-5} corresponding to scattering 44,311 photons before the ion stops yielding photons on average. While this is the fundamental limit in practice, speed and finite solid angle limit the fidelity. The best measured Yb^+ fidelity using this method at 99.97% [39].

1.2.5 $^{173}Yb^+$

$^{173}Yb^+$ has a highly deformed nucleus [21] which leads to the predicted hyperfine B coefficient ($\sim$-5 GHz) being larger than the A coefficient ($\sim$300 MHz) and due to the large nuclear spin of 173 (5/2) from equation 1.42 we see that this leads to a strong modification to the energy structure as seen in figure 1.10. We discuss future work with $^{173}Yb^+$ in chapters 9 and 10.

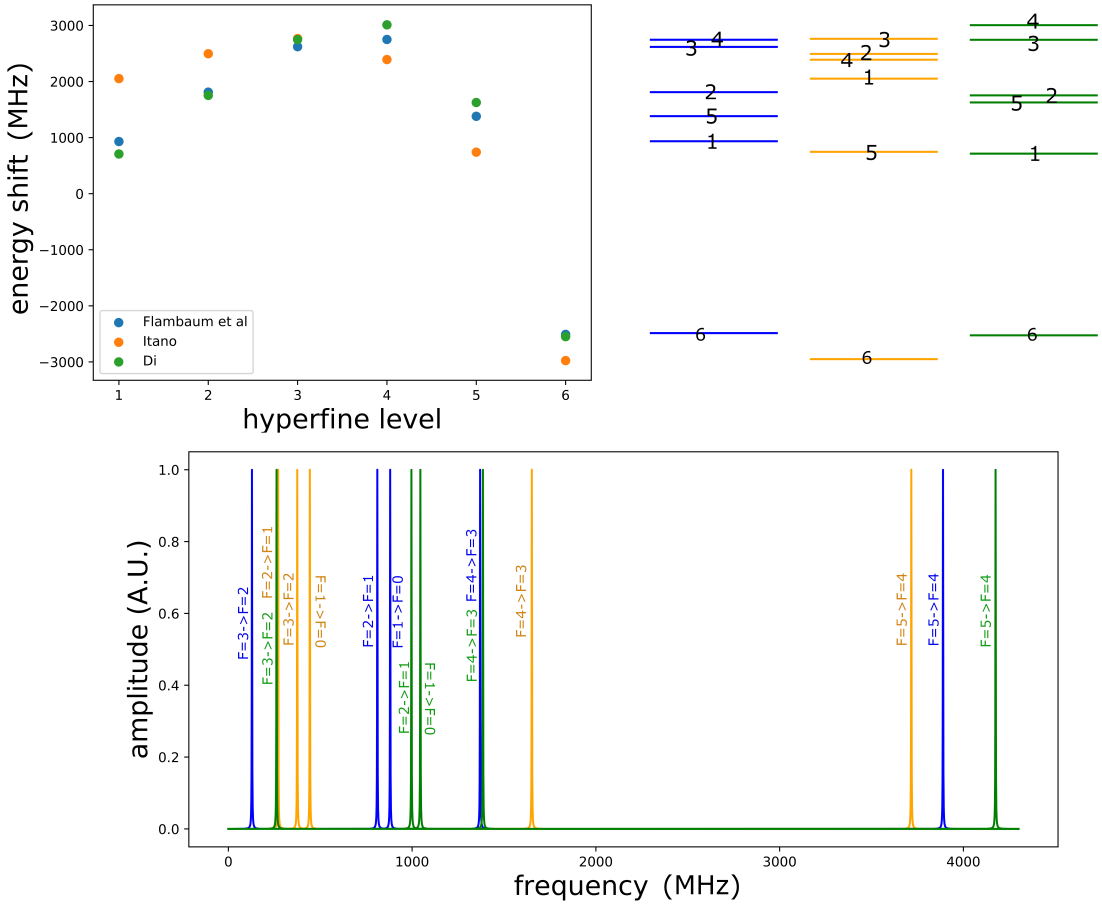

Figure 1.10: Predicted energy shifts in the $^2F_{7/2}$ hyperfine considering A and B coefficients (upper left) calculated by Itano[49](orange), Flambaum[21](blue) and Di Xiao[1](green). The upper right shows a diagram of the levels and the bottom are allowed magnetic dipole transitions frequencies.

CHAPTER 2

Atoms and Lasers

2.1 CW Lasers and atoms

In order to drive transitions in our ions for laser cooling, state preparation, measurement and shelving we apply laser radiation at or near an atomic transition. In our experiment we drive two types of transitions with lasers E1 (dipole) and E2 (Quadrupole).

2.1.1 Dipoles

The dipole Hamiltonian is

$$H = \vec{E} \cdot \vec{d} \tag{2.1}$$

Where $\vec{E}$ is the electric field and $\vec{d}$ is the dipole operator for the atom. The electric field can be written as

$$\vec{E} = \frac{\vec{\mathcal{E}}}{2} e^{i(\vec{k}\cdot\vec{r}-\omega t)} + c.c. \tag{2.2}$$

where $\vec{E_0} = E_0(E_x\hat{x} + E_y\hat{y} + E_z\hat{z})$ is the electric field amplitude times a complex polarization restricted to an arbitrary plane, and the dipole operator is the electric charge time the electron position operator

$$\vec{d} = e\vec{r} \tag{2.3}$$

If the wavelength of light is much larger than the spread of the wavefunction i.e. $\vec{k}\cdot\vec{r} << 1$

we can simplify the field to

$$\vec{E} = \frac{\vec{\mathcal{E}}}{2} e^{i(\vec{k}\cdot\vec{r}-\omega t)} + c.c. \approx \frac{\vec{\mathcal{E}}}{2} e^{i\omega t} + c.c \tag{2.4}$$

now the Hamiltonian becomes

$$\vec{E}\cdot\vec{d} = \frac{e\vec{\mathcal{E}}\cdot\vec{r}}{2} e^{-i\omega t} + c.c. \tag{2.5}$$

and using

$$\vec{\mathcal{E}}\cdot\vec{r} = x\mathcal{E}_x + y\mathcal{E}_y + z\mathcal{E}_z \tag{2.6}$$

the mapping to spherical coordinates for the position operators are

$$x = \frac{2\pi}{3} r(Y_{-1}^1 - Y_1^1) \tag{2.7}$$

$$y = i\frac{2\pi}{3} r(Y_{-1}^1 + Y_1^1) \tag{2.8}$$

$$z = \frac{2}{\sqrt{2}}\frac{2\pi}{3} r Y_0^1 \tag{2.9}$$

plugging this into (6)

$$\vec{\mathcal{E}}\cdot\vec{r} = r\sqrt{\frac{2\pi}{3}}\Big[\mathcal{E}_x(Y_{-1}^1 - Y_1^-) + i\mathcal{E}_y(Y_{-1}^1 + Y_1^1) + \frac{2}{\sqrt{2}}\mathcal{E}_z Y_0^1\Big] \tag{2.10}$$

regrouping and using the definitions

$$\mathcal{E}_+ = \frac{1}{\sqrt{2}}(\mathcal{E}_x + i\mathcal{E}_y) \tag{2.11}$$

$$\mathcal{E}_- = \frac{1}{\sqrt{2}}(\mathcal{E}_x - i\mathcal{E}_y) \tag{2.12}$$

gives

$$\vec{\mathcal{E}} \cdot \vec{r} = r\sqrt{\frac{4\pi}{3}}\left[\mathcal{E}_+ Y_{-1}^1 - \mathcal{E}_- Y_1^1 + \mathcal{E}_z Y_0^1\right] \tag{2.13}$$

Plugging into (5)

$$\vec{E} \cdot \vec{d} = er\sqrt{\frac{\pi}{3}}e^{-i\omega t}\left[\mathcal{E}_+ Y_{-1}^1 - \mathcal{E}_- Y_1^1 + \mathcal{E}_z Y_0^1\right] \tag{2.14}$$

Now we want to find the transition amplitudes between hydrogenic wavefunctions

$$\langle nlm|\, \vec{E} \cdot \vec{d}\, |n'l'm'\rangle \tag{2.15}$$

combining (14) and (15)

$$\begin{aligned}\langle nlm|\, \vec{E} \cdot \vec{d}\, |n'l'm'\rangle = e\sqrt{\frac{\pi}{3}}e^{-i\omega t}\Big[&\mathcal{E}_+ \langle nlm|\, rY_{-1}^1\, |n'l'm'\rangle \\ &- \mathcal{E}_- \langle nlm|\, rY_1^1\, |n'l'm'\rangle \\ &+ \mathcal{E}_z \langle nlm|\, rY_0^1\, |n'l'm'\rangle\Big]\end{aligned} \tag{2.16}$$

For hydrogenic wavefunctions the radial and angular parts of $|nlm\rangle$ are separable and thus can be written as a reduced matrix element that does not depend on the projection of the spherical harmonics multiplied by the angular matrix elements that do.

$$\begin{aligned}\langle nlm|\, \vec{E} \cdot \vec{d}\, |n'l'm'\rangle = e\sqrt{\frac{\pi}{3}}e^{-i\omega t}\langle nl|\, |r|\, |nl\rangle \Big[&\mathcal{E}_+ \langle lm|\, Y_{-1}^1\, |l'm'\rangle \\ &- \mathcal{E}_- \langle lm|\, Y_1^1\, |l'm'\rangle \\ &+ \mathcal{E}_z \langle lm|\, Y_0^1\, |l'm'\rangle\Big]\end{aligned} \tag{2.17}$$

let $\mathcal{A} = e\sqrt{\frac{\pi}{3}} \langle nl| \, |r| \, |nl\rangle \, e^{-i\omega t}$ and using the Wigner-Eckhart theorem

$$\langle lm| \, T_q^{(k)} \, |l'm'\rangle = (-1)^{l-m} \begin{pmatrix} l & k & l' \\ -m & q & m' \end{pmatrix} \langle L| \, |T^{(k)}| \, |L\rangle \tag{2.18}$$

we finally arrive at

$$\begin{aligned} &\langle nlm| \, \vec{E} \cdot \vec{d} |n'l'm'\rangle = \\ &\qquad \mathcal{A} \langle L| \, |T^{(1)}| \, |L\rangle \times \\ &\qquad \Big[\mathcal{E}_+ \begin{pmatrix} l & 1 & l' \\ -m & -1 & m' \end{pmatrix} - \mathcal{E}_- \begin{pmatrix} l & 1 & l' \\ -m & 1 & m' \end{pmatrix} + \mathcal{E}_z \begin{pmatrix} l & 1 & l' \\ -m & 0 & m' \end{pmatrix} \Big] \end{aligned} \tag{2.19}$$

2.1.2 Quadrupoles

The Quadrupole Hamiltonian is

$$H = -Q_{ij} \nabla_i E_j \tag{2.20}$$

where

$$Q_{ij} = r_i r_j \tag{2.21}$$

writing out all the terms

$$\begin{aligned} H = -\big[& x^2 \partial_x E_x + xy \partial_x E_y + xz \partial_x E_z \\ & + yx \partial_y E_x + y^2 \partial_y E_y + yz \partial_y E_z \\ & + zx \partial_z E_x + zy \partial_z E_y + z^2 \partial_z E_z \big] \end{aligned} \tag{2.22}$$

We need to Taylor expand the field to second order to get non-zero matrix elements so

$$\vec{E} = \frac{\vec{\mathcal{E}}}{2} e^{i(\vec{k}\cdot\vec{r}-\omega t)} + c.c. \approx \frac{\vec{\mathcal{E}}}{2} e^{i\omega t}(1 + i\vec{k}\cdot\vec{r}) + c.c \tag{2.23}$$

since only derivatives of the electric field are in H, the first term is 0 and using

$$\vec{k}\cdot\vec{r} = k_x x + k_y y + k_z z \tag{2.24}$$

it is clear that $\nabla_i E_j \to k_i \mathcal{E}_j$ and (22) becomes

$$\begin{aligned} H = -\big[& x^2 k_x \mathcal{E}_x + xy k_x \mathcal{E}_y + xz k_x \mathcal{E}_z \\ & + yx k_y \mathcal{E}_x + y^2 k_y \mathcal{E}_y + yz k_y \mathcal{E}_z \\ & + zx k_z \mathcal{E}_x + zy k_z \mathcal{E}_y + z^2 k_z \mathcal{E}_z \big] \end{aligned} \tag{2.25}$$

We now need to replace the dyadic components of Q with spherical tensors in order to apply the Wigner-Eckhart theorem. This can be done with tedious amounts of algebra. The dyadic components are,

$$x^2 = r^2\Big[\frac{1}{3} + 2\sqrt{\frac{\pi}{5}}\Big(\frac{1}{\sqrt{6}}Y^2_{-2} + \frac{1}{\sqrt{6}}Y^2_2 - Y^2_0\Big)\Big] \tag{2.26}$$

$$y^2 = r^2\Big[\frac{1}{3} - 2\sqrt{\frac{\pi}{5}}\Big(\frac{1}{\sqrt{6}}Y^2_{-2} + \frac{1}{\sqrt{6}}Y^2_2 + Y^2_0\Big)\Big] \tag{2.27}$$

$$z^2 = r^2\Big[\frac{1}{3} + \frac{4}{3}\sqrt{\frac{\pi}{5}}Y^2_0\Big] \tag{2.28}$$

$$xy = r^2 2i\sqrt{\frac{\pi}{30}}\Big(Y^2_{-2} - Y^2_2\Big) \tag{2.29}$$

$$xz = r^2 2\sqrt{\frac{\pi}{30}}\Big(Y_{-1}^2 - Y_1^2\Big) \tag{2.30}$$

$$yz = r^2 2i\sqrt{\frac{\pi}{30}}\Big(Y_{-1}^2 + Y_1^2\Big) \tag{2.31}$$

plugging these into (25)

$$\begin{aligned}
H = \\
-r^2\Bigg\{ &\Big[\frac{1}{3} + 2\sqrt{\frac{\pi}{5}}\Big(\frac{1}{\sqrt{6}}Y_{-2}^2 + \frac{1}{\sqrt{6}}Y_2^2 - Y_0^2\Big)\Big]k_x\mathcal{E}_x + 2i\sqrt{\frac{\pi}{30}}\Big(Y_{-2}^2 - Y_2^2\Big)k_x\mathcal{E}_y + \\
&2\sqrt{\frac{\pi}{30}}\Big(Y_{-1}^2 - Y_1^2\Big)k_x\mathcal{E}_z + 2i\sqrt{\frac{\pi}{30}}\Big(Y_{-2}^2 - Y_2^2\Big)k_y\mathcal{E}_x + \\
&\Big[\frac{1}{3} - 2\sqrt{\frac{\pi}{5}}\Big(\frac{1}{\sqrt{6}}Y_{-2}^2 + \frac{1}{\sqrt{6}}Y_2^2 + Y_0^2\Big)\Big]k_y\mathcal{E}_y + 2i\sqrt{\frac{\pi}{30}}\Big(Y_{-1}^2 + Y_1^2\Big)k_y\mathcal{E}_z \\
&+ 2\sqrt{\frac{\pi}{30}}\Big(Y_{-1}^2 - Y_1^2\Big)k_z\mathcal{E}_x + 2i\sqrt{\frac{\pi}{30}}\Big(Y_{-1}^2 + Y_1^2\Big)k_z\mathcal{E}_y + \Big[\frac{1}{3} + \frac{4}{3}\sqrt{\frac{\pi}{5}}Y_0^2\Big]k_z\mathcal{E}_z\Big]
\end{aligned} \tag{2.32}$$

then grouping by spherical harmonics

$$\begin{aligned}
H = -r^2\Bigg[&\frac{1}{3}\Big(k_x\mathcal{E}_x + k_y\mathcal{E}_y + k_z\mathcal{E}_z\Big) \\
&+ \Big[2\sqrt{\frac{\pi}{30}}k_x\mathcal{E}_x - i2\sqrt{\frac{\pi}{30}}\Big(k_x\mathcal{E}_y + k_y\mathcal{E}_x\Big) - 2\sqrt{\frac{\pi}{30}}k_y\mathcal{E}_y\Big]Y_2^2 \\
&- \Big[2\sqrt{\frac{\pi}{30}}\Big(k_x\mathcal{E}_z + k_z\mathcal{E}_x\Big) - i2\sqrt{\frac{\pi}{30}}\Big(k_y\mathcal{E}_z + k_z\mathcal{E}_y\Big)\Big]Y_1^2 \\
&- \Big[2\sqrt{\frac{\pi}{5}}k_x\mathcal{E}_x + 2\sqrt{\frac{\pi}{5}}k_y\mathcal{E}_y + \frac{4}{3}\sqrt{\frac{\pi}{5}}k_z\mathcal{E}_z\Big]Y_0^2 \\
&+ \Big[2\sqrt{\frac{\pi}{30}}\Big(k_x\mathcal{E}_z + k_z\mathcal{E}_x\Big) + i2\sqrt{\frac{\pi}{30}}\Big(k_y\mathcal{E}_z + k_z\mathcal{E}_y\Big)\Big]Y_{-1}^2 \\
&+ \Big[2\sqrt{\frac{\pi}{30}}k_x\mathcal{E}_x + i2\sqrt{\frac{\pi}{30}}\Big(k_x\mathcal{E}_y + k_y\mathcal{E}_x\Big) - 2\sqrt{\frac{\pi}{30}}k_y\mathcal{E}_y\Big]Y_{-2}^2 \\
&\Bigg]
\end{aligned} \tag{2.33}$$

The monopole in the top line (33) is $\vec{k}\cdot\vec{\mathcal{E}}$ which is zero for plane waves. Removing this and factoring we get

$$\begin{aligned} H = -2\sqrt{\frac{\pi}{30}}r^2\Bigg[&\Big[k_x\mathcal{E}_x - i\Big(k_x\mathcal{E}_y + k_y\mathcal{E}_x\Big) - k_y\mathcal{E}_y\Big]Y_2^2 \\ &- \Big[\Big(k_x\mathcal{E}_z + k_z\mathcal{E}_x\Big) - i\Big(k_y\mathcal{E}_z + k_z\mathcal{E}_y\Big)\Big]Y_1^2 \\ &- \Big[\sqrt{6}k_x\mathcal{E}_x + \sqrt{6}k_y\mathcal{E}_y + \frac{2}{3}\sqrt{6}k_z\mathcal{E}_z\Big]Y_0^2 \\ &+ \Big[\Big(k_x\mathcal{E}_z + k_z\mathcal{E}_x\Big) + i\Big(k_y\mathcal{E}_z + k_z\mathcal{E}_y\Big)\Big]Y_{-1}^2 \\ &+ \Big[k_x\mathcal{E}_x + i\Big(k_x\mathcal{E}_y + k_y\mathcal{E}_x\Big) - k_y\mathcal{E}_y\Big]Y_{-2}^2\Bigg] \end{aligned} \tag{2.34}$$

taking matrix elements with the hydrogenic wavefunctions

$$\langle nlm| - Q_{ij}\nabla_i E_j\,|n'l'm'\rangle \tag{2.35}$$

and using the separable wave functions defining the reduced matrix element

$$\mathcal{B} = -2\sqrt{\frac{\pi}{30}}\,\langle nl|\,|r^2|\,|nl\rangle \tag{2.36}$$

we can apply the Wigner Eckhart (18) to obtain

$$
\begin{aligned}
&\langle nlm| - Q_{ij}\nabla_i E_j \,|n'l'm'\rangle = \\
&\mathcal{B}\,\langle L|\,|T^{(2)}|\,|L\rangle \times \\
&\Big[\Big[k_x\mathcal{E}_x - i\Big(k_x\mathcal{E}_y + k_y\mathcal{E}_x\Big) - k_y\mathcal{E}_y\Big]\begin{pmatrix} l & 2 & l' \\ -m & 2 & m'\end{pmatrix} \\
&\quad - \Big[\Big(k_x\mathcal{E}_z + k_z\mathcal{E}_x\Big) - i\Big(k_y\mathcal{E}_z + k_z\mathcal{E}_y\Big)\Big]\begin{pmatrix} l & 2 & l' \\ -m & 1 & m'\end{pmatrix} \\
&\quad - \Big[\sqrt{6}k_x\mathcal{E}_x + \sqrt{6}k_y\mathcal{E}_y + \frac{2}{3}\sqrt{6}k_z\mathcal{E}_z\Big]\begin{pmatrix} l & 2 & l' \\ -m & 0 & m'\end{pmatrix} \\
&\quad + \Big[\Big(k_x\mathcal{E}_z + k_z\mathcal{E}_x\Big) + i\Big(k_y\mathcal{E}_z + k_z\mathcal{E}_y\Big)\Big]\begin{pmatrix} l & 2 & l' \\ -m & -1 & m'\end{pmatrix} \\
&\quad + \Big[k_x\mathcal{E}_x + i\Big(k_x\mathcal{E}_y + k_y\mathcal{E}_x\Big) - k_y\mathcal{E}_y\Big]\begin{pmatrix} l & 2 & l' \\ -m & -2 & m'\end{pmatrix}\Big]
\end{aligned}
\tag{2.37}
$$

2.1.3 2-Level systems (qubits)

Many times we approximate our atomic system as a 2-level system coupled by a laser.

The two-level Hamiltonian with a laser coupling term can be written as

$$
H_{tot} = E_g|g\rangle\langle g| + E_e|e\rangle\langle e| + \frac{\hbar\Omega}{2}\Big(e^{-i\omega_L t}|e\rangle\langle g| + e^{i\omega_L t}|g\rangle\langle e|\Big) \tag{2.38}
$$

using Schrödinger's equation $i\hbar\frac{\partial|\Psi\rangle}{\partial t} = H\,|\Psi\rangle$ with $|\Psi\rangle = c_g\,|g\rangle + c_e\,|e\rangle$

$$
i\hbar\Big(\dot{c}_g\,|g\rangle + \dot{c}_e\,|e\rangle\Big) = c_g E_g\,|g\rangle + c_e E_e\,|e\rangle + \frac{\hbar\Omega}{2}\Big(c_g e^{-i\omega_L t}\,|e\rangle + c_e e^{i\omega_L t}\,|g\rangle\Big) \tag{2.39}
$$

now act on the left side of (2) with $|g\rangle$ and $|e\rangle$ respectively you obtain

$$i\hbar\dot{c}_g = c_g E_g + \frac{\hbar\Omega}{2} c_e e^{i\omega_L t} \tag{2.40}$$

and

$$i\hbar\dot{c}_e = c_e E_e + \frac{\hbar\Omega}{2} c_g e^{-i\omega_L t} \tag{2.41}$$

We want to rotate at the laser frequency to obtain a time independent total Hamiltonian while the laser is on. Let $c_e \rightarrow c_e e^{-i\omega_L t}$ and take E_g to be zero (You could likewise take $E_g = -\frac{E}{2}$ and $E_e = \frac{E}{2}$ with $c_g \rightarrow c_g e^{i\frac{\omega_L}{2}t}$ and $c_e \rightarrow c_e e^{-i\frac{\omega_L}{2}t}$).

Equations (3) and (4) become

$$i\hbar\dot{c}_g = \frac{\hbar\Omega}{2} c_e \tag{2.42}$$

and

$$i\hbar e^{-i\omega_L t}\Big(\dot{c}_e - i\omega_L c_e\Big) = c_e E_e e^{-i\omega_L t} + \frac{\hbar\Omega}{2} c_g e^{-i\omega_L t} \tag{2.43}$$

Notice that the laser frequency is the atomic frequency plus the detuning $\omega_L = \omega_a + \delta$ and that $\hbar\omega_a = E_e$

Substituting

$$i\hbar\dot{c}_e + (\hbar\omega_a + \hbar\delta)c_e = c_e\hbar\omega_a + \frac{\hbar\Omega}{2} c_g \tag{2.44}$$

Simplifying

$$i\hbar\dot{c}_e = -\hbar\delta c_e + \frac{\hbar\Omega}{2} c_g \tag{2.45}$$

By rotating the state vectors Equations (5) and (8) are equivalent to a time-independent Schrödinger equation with Hamiltonian:

$$H_{rot} = \hbar \begin{pmatrix} 0 & \frac{\Omega}{2} \\ \frac{\Omega}{2} & -\delta \end{pmatrix} \tag{2.46}$$

with eigenvalues

$$E_{\pm} = \frac{\hbar}{2}\Big(-\delta \pm \sqrt{\delta^2 + \Omega^2}\Big) \tag{2.47}$$

2.1.4 Three Level system (qutrits)

While the two-level system works in many cases in some cases a third level must be considered and can lead to coherent effects such as EIT. A three-level system can provide useful tools such as shelving and the ability to define qutrits. For a three-level system we perform the same procedure and define the frequencies as ω_{L1}, ω_{L2}, ω_{L3} as the lasers that couple the states $|0\rangle\langle 1|$, $|0\rangle\langle 2|$ and $|1\rangle\langle 2|$ respectively. The Hamiltonian for this system is

$$H = E_0|0\rangle\langle 0| + E_1|1\rangle\langle 1| + E_2|2\rangle\langle 2| + \frac{\hbar\Omega_1}{2}e^{i\omega_{L1}t}|0\rangle\langle 1| + \frac{\hbar\Omega_2}{2}e^{i\omega_{L2}t}|0\rangle\langle 2| + \frac{\hbar\Omega_3}{2}e^{i\omega_{L3}t}|1\rangle\langle 2| + h.c. \tag{2.48}$$

taking the state vector as

$$|\Psi\rangle = c_0\,|0\rangle + c_1\,|1\rangle + c_2\,|2\rangle \tag{2.49}$$

and applying Schrödinger's equation

$$i\hbar\frac{\partial\,|\Psi\rangle}{\partial t} = H\Psi \tag{2.50}$$

we obtain

$$
\begin{aligned}
i\hbar\Big(\dot{c}_0\,|0\rangle + \dot{c}_1\,|1\rangle + \dot{c}_2\,|2\rangle\Big) = \\
& c_0\Big(E_0\,|0\rangle + \frac{\hbar\Omega_1}{2}e^{-i\omega_{L1}t}\,|1\rangle + \frac{\hbar\Omega_2}{2}e^{-i\omega_{L2}t}\,|2\rangle\Big) \\
& + c_1\Big(E_1\,|1\rangle + \frac{\hbar\Omega_1}{2}e^{i\omega_{L1}t}\,|0\rangle + \frac{\hbar\Omega_3}{2}e^{-i\omega_{L3}t}\,|2\rangle\Big) \\
& + c_2\Big(E_2\,|2\rangle + \frac{\hbar\Omega_2}{2}e^{i\omega_{L2}t}\,|0\rangle + \frac{\hbar\Omega_3}{2}e^{i\omega_{L3}t}\,|1\rangle\Big)
\end{aligned}
\tag{2.51}
$$

Now we act on the left of (14) with the basis vectors to obtain 3 differential equations

$$
i\hbar\dot{c}_0 = c_0E_0 + c_1\frac{\hbar\Omega_1}{2}e^{i\omega_{L1}t} + c_2\frac{\hbar\Omega_2}{2}e^{i\omega_{L2}t} \tag{2.52}
$$

$$
i\hbar\dot{c}_1 = c_1E_1 + c_0\frac{\hbar\Omega_1}{2}e^{-i\omega_{L1}t} + c_2\frac{\hbar\Omega_3}{2}e^{i\omega_{L3}t} \tag{2.53}
$$

$$
i\hbar\dot{c}_2 = c_2E_2 + c_0\frac{\hbar\Omega_2}{2}e^{-i\omega_{L2}t} + c_1\frac{\hbar\Omega_3}{2}e^{-i\omega_{L3}t} \tag{2.54}
$$

From Here we can make some simplifying definitions. $E_0 = 0$, $c_1 \to c_1e^{-i\omega_{L1}t}$, $c_2 \to c_2e^{-i\omega_{L2}t}$

equations 15-17 become

$$
i\hbar\dot{c}_0 = c_1\frac{\hbar\Omega_1}{2} + c_2\frac{\hbar\Omega_2}{2} \tag{2.55}
$$

$$
i\hbar\dot{c}_1 = c_0\frac{\hbar\Omega_1}{2} - c_1\hbar\delta_1 + c_2\frac{\hbar\Omega_3}{2}e^{i(\omega_{L1}+\omega_{L3}-\omega_{L2})t} \tag{2.56}
$$

$$
i\hbar\dot{c}_2 = c_0\frac{\hbar\Omega_2}{2} + c_1\frac{\hbar\Omega_3}{2}e^{-i(\omega_{L1}+\omega_{L3}-\omega_{L2})t} - c_2\hbar\delta_2 \tag{2.57}
$$

defining $\phi = \omega_{L1} + \omega_{L3} - \omega_{L2}$ The Hamiltonian becomes:

$$H_{rot} = \hbar \begin{pmatrix} 0 & \frac{\Omega_1}{2} & \frac{\Omega_2}{2} \\ \frac{\Omega_1}{2} & -\delta_1 & \frac{\Omega_3}{2} e^{i\phi t} \\ \frac{\Omega_2}{2} & \frac{\Omega_3}{2} e^{-i\phi t} & -\delta_2 \end{pmatrix} \tag{2.58}$$

2.2 Pulsed Lasers

Pulsed lasers can refer both to switched incoherent lasers and mode-locked lasers. The difference between them have to do with the pulse to pulse phase coherence. If there is not an optical phase relationship from pulse to pulse, then coherent manipulation of an oscillator (such as an atom) cannot be performed since the intensity of the laser relative to the oscillators phase upon consecutive pulses will be random. However, if there is a well-defined phase, then the oscillator can be excited repeatedly with the same intensity at the same phase. In this work we will be looking at coherent interactions with mode-Locked lasers and ions and will be exclusively in the regime where there is pulse-pulse coherence. It should be noted that the laser is not the only thing in the system whose phase matters. If the oscillator (ion) phase scrambles due to decoherence, it will have the same effect as the laser phase being incoherent.

2.2.1 Mode Locked Lasers

A laser cavity will support any mode that satisfies two conditions, 1) the mode is within the bandwidth of the lasing medium and 2) the cavity is an integer multiple of the wavelength of the mode. The electric in a 1-D cavity with $N = 2m + 1$ modes can be written as [40]

$$E(t) = \sum_{n=-m}^{m} E_n \exp\left[i(\omega_0 + n\frac{2\pi}{t_r})t + \phi_n \right] \tag{2.59}$$

where ω_0 is the center mode frequency of the bandwidth of the laser, $t_r = \frac{2L}{c}$ is the repetition rate of the laser and ϕ_n is the phase of each mode. We have assumed equal

amplitude of each mode. If the phases ϕ_n fluctuate randomly relative to each other this will result in random intensity spikes as modes have a probability of being in phase for short periods of time. If a non-linear element such as a saturable absorber whose transmission coefficient increases with intensity is inserted, these in-phase fluctuations will be less damped than the lower power out-of-phase amplitudes. This leads to a fixed phase relationship between modes in the cavity. For this analysis we will assume that all modes lock to the same phase which we may as well set to zero. Then equation 2.59 becomes

$$E(t) = \sum_{n=-m}^{m} E_n \exp\left[i(\omega_0 + n\frac{2\pi}{t_r})t\right] \tag{2.60}$$

This can be summed to [40]

$$E(t) = E_0\left[\frac{1-\exp\left(i\frac{2N\pi t}{t_r}\right)}{1-\exp\left(i\frac{2\pi t}{t_r}\right)}\right] \tag{2.61}$$

and the intensity of the light is

$$I(t) = E(t)E^*(t) = E_0^2\frac{\sin^2(\frac{N\pi t}{t_r})}{\sin^2(\frac{\pi t}{t_r})} \tag{2.62}$$

In this thesis we used an actively mode-locked Titanium-Sapphire laser with a repetition rate of 80 MHz and about $N = 600$ modes. Figure 2.1 show that even at $N = 20$ the pulses are highly localized.

The solution shows that in time a mode-locked laser creates a train of intense pulses leaking out of the laser cavity at the repetition rate. As more and more modes participate the pulses become shorter and in the limit of large mode numbers can be considered delta functions. The Fourier transform of a train of delta functions is again a train of delta functions and thus in the frequency domain the mode-locked laser has a "comb" of frequencies separated by the repetition rate.

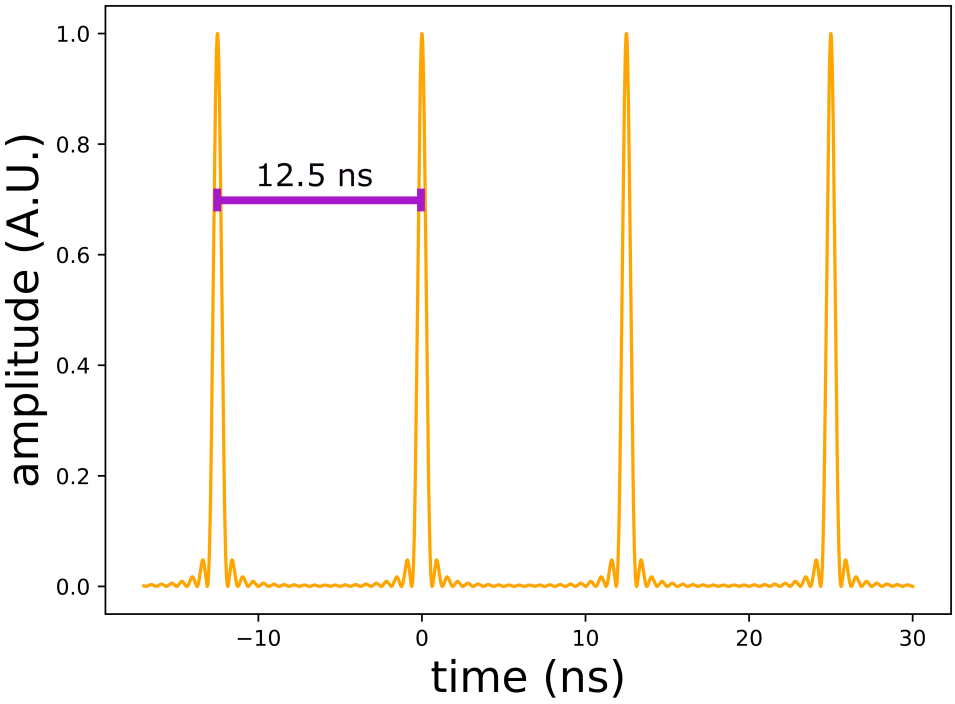

Figure 2.1: Equation 2.62 plotted for t_r= 12.5 ns and 20 pulses

CHAPTER 3

Ions as Qubits

One of the strengths of ions compared to other platforms such as superconducting qubits is the fundamentally identical nature of multiple ions. While this is true, interactions of ions with the external environment can lead to decoherence. Furthermore, the finite lifetimes of transitions lead to decays or off-resonant effects that remove the qubit from its ideal two-level basis. In the following we will describe three kinds of ionic qubits and their benefits and difficulties

3.1 Optical Qubits

Optical frequencies are 10's-1000's of THz and generally drive atomic transitions between different orbital angular momentum states. While opposite parity states can couple to the dipole operator, these transitions tend to have too short of a lifetime to use as a qubit. Instead optical qubits are usually defined on long lived quadrupole transitions which decay on the order of 1 s. The high frequencies of optical qubits provide natural protection from off-resonant scattering. This is because in the standard system the ground $|0\rangle$ state is also coupled to a strong cycling transition many THz away. This means that detection times are only limited by the excited metastable state lifetime. The downside of these qubits is also their lifetime, quantum operations are required to be much faster than the coherence time and many repeated operations, especially slow ones can suffer from decoherence due to finite lifetime. While this is the fundamental decoherence source, the laser itself needs to match this coherence time and thus lasers with line-widths <10kHz are generally required which are much more difficult to obtain than the narrow microwave sources used in the following

qubits.

3.2 Hyperfine Qubits

Hyperfine qubits are defined on two states of different alignment of the total electronic and nuclear spin, ($F_{\pm} = I \pm J$) and usually on a magnetic field insensitive projection such as $|F = 0, m_F = 0\rangle \longrightarrow |F = 1, m_F = 0\rangle$. The transitions frequencies tend to be in the 1-20 GHz range. The coupling is due to a magnetic dipole interaction. Due to hyperfine qubits being in the microwave regime, cheap narrow line-width oscillators are available at high power. Hyperfine qubits may also be driven with a resonant beat-note of a laser allowing line-width defined by microwaves and coupling to motion of the ion in the trap. Hyperfine qubits with nuclear spin 1/2 also have a low-lying singlet state that can be optically pumped into, allowing fast frequency selective preparation of a pure quantum state. Disadvantages of the hyperfine structure are the extra level only GHz detuned that cause mixing of the qubit during detection.

3.3 Zeeman Qubits

Zeeman qubits are defined simply on the projection of the electron spin. These are also magnetic dipole transitions. The frequencies of these states are split by a Bohr magneton of 1.4MHz/Gauss and tend to be 50-100MHz for reasonable fields. While qubits that are sensitive in first order to a magnetic field are highly susceptible to magnetic field noise, this has been mitigated in certain instances with great success [57] by using magnetic shielding. These qubits can be coupled with stimulated Raman transitions in the same way as hyperfine qubits but without the extra levels associated with a hyperfine qubit. This very pure two-level grounds state may have long term advantages in quantum computing [13].

CHAPTER 4

Experimental Setup

4.1 Oblate Trap

A quadrupole trapping potential can be formed with two common geometries, the first and more common is the 4-rod trap where the rods form a quadrupole radially and the ideally very long rods are capped with DC electrodes. The other geometry of which our trap is an example of is a ring electrode. This style trap provides 3D confinement without the need for DC caps although in practice DCs are used for micromotion compensation.

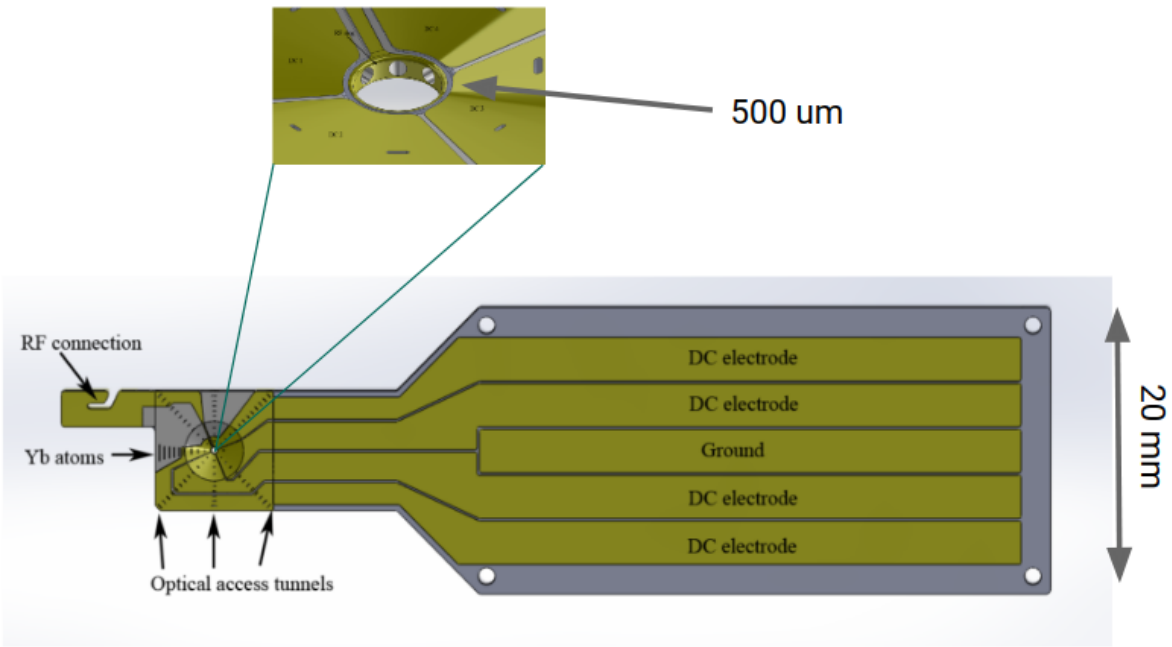

Figure 4.1: Solid works diagram of the trap. Inset shows RF ring and access tunnels

Our trap is a micro-fabricated ring design which confines ions radially as well as in the

Z direction. The ring diameter is 500μm and was laser drilled through the center of a microscope slide. The glass is etched by Translume[68] who also plated the electrodes with gold. In addition, three through hole trenches are created to allow laser access through the sides of the ring with 100μm entrance and exit holes at the ring see 4.1. An additional hole allows access for neutral Yb atoms to reach the center of the trap where they can be loaded and cooled. The far side of the ring opposite the loading hole is also recessed to allow excess Yb to be deposited away from the ring.

The Yb source is a stainless-steel tube where natural abundance Yb foil is placed. The tube has tantalum foil spot welded to create a hot spot at the foil when current is applied. We typically apply 2.35 Amps to the source and after a thermalization time of about 3.5 minutes we load a single Yb ion. If the source is left on, we will load subsequent ions every 3-10 seconds.

Both the source and the trap are placed in an 8" vacuum octagon with dual AR coated recessed windows allowing for very large solid angles (see figure 4.2). Also view ports surrounding the trap allow laser access to the trenches in the ring.

In order to reach the required UHV pressures (3×10^{-11}mBar), we must pump the chamber down while baking for about 2 weeks in an oven at 200 °C. After cooling down an evaporable getter (NEG) is activated to absorb particles. After the NEG is fired which requires external pumping, we close the angle valve separating the chamber from the pump. An attached ion pump and Tisub pump are then used to bring the pressure down to its final value.

The chamber is mounted to the optical table with electrically isolating feet in order to prevent ground loops and pickup through the table. The chamber is grounded to a silver grounding plate which in turn is earth grounded.

Imaging is accomplished through the two re-entrant windows with standard special optics microscope objective (54-17-29@370NM). One objective is focused through an adjustable aperture and onto a PMT while the other is focused on to an adjustable aperture and then imaged through a secondary homemade doublet onto either a PMT or an EMCCD camera

(ixon3). This imaging can be switched with a computer controlled flipper mirror. See fig 4.7 for a composite image of the trap on the EMCCD with the solid works drawing super imposed. This imaging is made by scattering 369 nm light on the trap as all other light is filtered from the camera.

4.1.1 Loading in the oblate trap

The trap is driven at 47.233 MHz with a DDS channel from our pulse sequencer. The voltage is amplified with a ZHL-5W amplifier and fed to an RF resonator can with a quality factor of ∼200. The RF can impedance matches the RF to the trap as well as steps the voltage up to the required hundreds of volts.

An oven made of a stainless-steel tube with ytterbium foil is spot welded to tantalum strips and is heated to send atoms to the center of the trap. The atoms are resonantly excited with 399 nm light and photo ionized with the 369 nm laser which is duel purposed for cooling.

Stray fields can initially move the ion off the RF null and laser cooled ions can have significant micro-motion. We use several techniques to minimize the micro-motion, the coarsest of which uses the camera. By increasing and decreasing the RF voltage we can follow the ion towards the center of the trap by adjusting the linear field in the direction it moves. When the ion is near the center of the trap, we move the ion around ∼10μm diameter while observing the line width and micromotion side-bands, see figure 1.3. The ion can be adjusted to minimize these side-bands and is generally sufficient for all experiments in this thesis. It should be noted that none of the current techniques address micro-motion in the Z direction, we have found a location in the Z where the lifetimes are maximized. The three-dimensional stray fields compensated for in x,y, and z are (1.610, -1.030, -4.8) V/mm

The trap is not perfectly cylindrically symmetric even in principle as in 4.1. A large RF trace is fed to the ring on one side of the trap. This breaking of the symmetry is obvious with large crystals where we observe a linear null superimposed with our symmetric null. Due to this affect we find it much more difficult to identify the null in the direction of

this superimposed trap (x directions). A trap was designed with the RF being delivered via a shielded trench to maintain a higher degree of symmetry, but due to manufacturing difficulties this via was not reliable.

Trapped ions in the oblate trap can be seen in figure 4.6. In this instance the confinement in the Z direction was weak enough that the ions formed 3D structures. As the voltage is increased the ions become 2D and the axial secular frequency follows the expected square root dependence on RF power see figure 4.5

Images of the trap taken with the iXon EMCCD camera and laid over the solid works design are shown in figure 4.7. We use this mapping of the trap to initially align our imaging to the trap center and find that the null of the RF is the geometric center within $\sim 10\mu$m

4.1.2 Oblate trap damage

In early August of 2018 there was a discrete behavior change of the trapped ions. The trap null appeared to be drifting on the timescale of seconds and it became impossible to keep the lasers pointed at the ions or low micro-motion for any reasonable period of time. After much investigation it was found that the gold RF ring had de-laminated from the underlying glass see figure 4.3. The believed cause of this is thermal stress from slow cycling of the RF power (Turning the RF off for a conference).

Luckily Translume had an identical trap in Michigan and quickly shipped it out see figure 4.4. This trap has no visible damage and was placed in the chamber and baked out. When loading this trap, it was discovered that the stray fields in the new setup drifted quite bit (many V/mm per day). The suspicion was charging of the re-entrant view-ports. An external DC probe was able to move the ions significantly with only 1 volt about 10mm from the ion.

In order to fix this charging, we opened the chamber and installed grounded high transparency mesh made of 316 stainless steel with a visibility of 81% on both re-entrant view-ports. After baking and loading the stray fields are extremely stable see figure 4.10

4.2 Lasers

4.2.1 The 399 nm Laser

Once neutral atoms are at the center of the trap, they are excited by an isotope selective 399 nm laser to the $^1P_1$ transition. This state brings the continuum states into reach of the ion cooling 369 nm laser. The 399 laser is a DL100 Pro series ECDL from toptica. The laser can be tuned to a specific isotope for loading and we find that we load 80-90% of the time the intended isotope. The imperfection here is due to the large overlap of the Doppler broadened transitions and the similar sized Doppler shifts. See 1.4 for the spectrum in our specific setup. The 399 nm laser is measured on a WS7 wavemeter and the stability is sufficiently long over the loading period that we do not need an active lock. We shine 80μW of 399 nm light at about 50μm diameter waist. When an ion is detected a mechanical shutter blocks the 399 nm laser both to prevent the loading of more ions while the oven is cooling down and to avoid possible charging from the 399 nm laser.

4.2.2 The 369 nm laser

The 369 nm laser is a direct diode by Moglabs. It is equipped with a Nichia NDU1113E. We get about 5mW of power directly out of the laser. 300uW is split off and directed to a vacuum sealed cavity made of glass and steel and designed to have an athermal expansion coefficient. The laser is Pound-Drever-Hall locked to the cavity with modulated sidebands on the laser current of 250kHz. The cavity is made from two >99.7 % reflective mirrors with a radius of curvature of 150mm from layertec. These mirrors are arranged in a nearly confocal configuration allowing locking to the 0,0 transverse mode. The free spectral range (FSR) is measured to be 1048 MHz with a finesse of 942. This corresponds to a linewidth of 1.1 MHz and the signal to noise for our setup is >10 allowing locking of the laser with a short term stability much lower than the transition linewidth (20MHz). In practice the long term drift tends to be 10s of MHz per day and we feedback on this by periodically measuring the ions cooling transition and adjusting the double-passed light frequency.

4.2.3 The 935 nm laser

When the ion is excited to the $^2P_{1/2}$ state there is a 0.5% chance it will leave the cooling cycle and decay to the $^2D_{3/2}$ metastable state. The lifetime of this state is 52.7 ms and would result in an extreme reduction in fluorescence and cooling power if not re-pumped. We repump this state to the $^3[3/2]_{1/2}$ state which decays into the cooling cycle with 98.2% probability otherwise returns to the $^2D_{3/2}$ to be re-pumped again. We use a distributed Bragg refractor (DBR) laser for 935 nm that is software locked to a WSU toptica wavemeter. The lock center is stable to ∼5MHz and the linewidth of the DBR is estimated to be about 30MHz from transition measurements. The 935 is passed through a single AOM to allow for power control as well as fast switching and subtracting for background free fluorescence detection used when addressing the position of 369 nm lasers on the ion as well as for initial loading.

4.2.4 The 411 nm laser

The 411 nm laser is used to drive the $^2S_{1/2} \longrightarrow^2 D_{5/2}$. This laser is generated with an M2 TiSaph laser that is doubled from 822 nm. The laser is software locked in the red. We generate about 100mW of 411 nm light that is passed through a double pass AOM configuration and fiber coupled to the chamber where it is overlaid with the 399nm laser. There is about 5mW sent to the ion with a waist of about 30μm diameter.

4.2.5 The 760 nm lasers

Two 760 lasers are required due to the large splitting of the hyperfine levels in the $^2F_{7/2}$ and the $^1[3/2]_{3/2}$ (3.6 GHz and 8.9 GHz respectively). One is generated from a homemade ECDL Littrow configuration and produces 50mW out of the laser. The other is a DBR which generates 40mW. Both these lasers are software locked 5.257 GHz apart to drive their respective transitions. They are each sent through a single pass AOM and overlaid on a PBS. The lasers are then combined with the 935 nm laser on a dichroic and fiber coupled to the chamber. We typically send about 10mW of each beam to the ion at a waist of 100μm

diameter. See figure 4.9 for spectrum of the used 760 nm transitions. Note in order to gain statistics multiple ion were loaded, the fact that these were of the micromotion null and that they remained dark for long periods of time induced the visible micromotion side bands in figure 4.9.

4.2.6 The 976 nm laser

The 976 nm laser repumps the $^2D_{5/2}$ and has the advantage that it does not need to wait for a decay to the F state to return the ion to the cooling cycle. We currently employ this laser to do much faster spectroscopy of the $^2S_{1/2} \longrightarrow ^2 D_{5/2}$ transition with the 411 nm laser. The 976 nm laser is a DBR butterfly fiber coupled laser available from thorlabs (DBR760PN). The laser is passed through an AOM and overlaid with the 935 nm laser. Spectrum of the 976 nm transitions are shown if figure 4.8.

4.2.7 Laser table

See table 4.1 for a list of the current laser frequencies used in our lab as measured on a high finesse WSU wavemeter and calibrated to a rubidium saturated absorption lock at 780 nm.

Laser	$^{171}Yb^+$	$^{174}Yb^+$
369	811.28910 THz	811.29153 THz
935	320.57175 THz	320.569030 THz
399	751.52680 THz	751.52760 THz
411	2× 364.737290 THz	2× 364.737640 THz
760	394.424700 THz and 394.429957 THz	394.423900 THz
976	see 4.8	307.068535 THz

Table 4.1: Transition frequencies measured in our lab. The 369 frequency for 171 is the $^2S_{1/2}$ F=1 to $^2P_{1/2}$ F=0 cooling transition. The 935 for 171 is the $^2D_{3/2}$ F=1 to $^3[3/2]_{1/2}$ F=0 transition. The 411 for 171 is the $^2S_{1/2}$ F=1 to the center of the two hyperfine transitions in the $^2D_{5/2}$. The 760 nm in 171 is the $^2F_{7/2}$ F=3 to $^1[3/2]_{3/2}$ F=1 and $^2F_{7/2}$ F=4 to $^1[3/2]_{3/2}$ F=2 respectively

4.3 Microwaves

4.3.1 12.6 GHz

In order to the drive the qubit in 171 a narrow source near 12.642812 is needed. In our experiment this is accomplished with an HP8672A. About +10 dBm of power is generated 200 MHz higher than needed and mixed onto a DDS at 200 MHz. This allows fast frequency, amplitude and phase control. The signal is band pass filtered near the qubit to remove extra tones. After pre-amplification the tone is amplified with a mini circuits solid state amplifier to about 3W (ZVE-3W-183+). The power is directed onto a directional microwave horn with 20 dB of gain (PE9855/SF-20). The horn is positioned 1 foot from the ion outside the chamber.

4.3.2 3.6 GHz

The metastable qubit explored in chapter 9, defined in the F state of 173 is separated by 3.6 GHz and we derive this source from an RF consultants oscillator which is mixed with a DDS at 200 MHz. The desired tone is amplified to 16W with a mini-circuits amplifier ZHL-16W-43-S+ and sent to a directional microwave horn with 10 dB gain from Pasternak (PE9863-10). The power is directed to the ion about 2 feet away from outside the chamber.

4.3.3 2.1 GHz

The upper hyperfine splitting in 171 is 2.105 GHz and a tone must be placed on the 369 nm laser to ensure efficient preparation of the F=0 ground state qubit. This tone is generated with a custom multi-channel frequency source for Yb (MagiQ). The frequency is amplified and sent to a Newport resonant electro-optic modulator. The amplitude is adjusted so that the carrier is optimally depleted.

4.3.4 7.374 GHz

When Doppler cooling $^{171}Yb^{+}$ with the carrier of the 369 nm laser, the atom can be trapped in the $^{2}S_{1/2}$ F=0 state. In order to return the atoms to the cooling cycle a tone is added to this beam at 7379 GHz. The second order sideband of the modulation is about 1% the carrier and occurs at 14.758 GHz (10 MHz blue of the actual splitting). This provides optimal repumping when Doppler cooling ∼10 MHz red detuned.

4.4 Electronics

An ion trap requires a fairly sophisticated set of AC and DC voltages that control the ion with the required precision. The two main pieces of electronics are the pulse sequencer (pulser) developed by Thaned Pruttiversan [51] and a Digital to analog converter developed by Dylan Gorman.

4.4.1 The Pulser

The pulser provides us with up to 16 direct digital synthesizers (DDS) although we only currently populate 11. There are also 35 digital outputs available for TTL switching. The timing is controlled by a master FPGA (XEM6010 by Opal Kelly) which preloads a sequence to all available DDS boards onto a local FPGA. The sequence is cycled through with TTLs provided by the master FPGA along with any required TTL outputs. The timing resolution for TTL pulses is 10 ns and the timing for DDS pulses is 40 ns. Phase amplitude and frequency can be programmed at every step of the sequence. The pulser does not have a limit of duration (for instance many hours can pass between TTLs in one sequence) however it does have a complexity limit with 1024 unique switches. Much more technical information can be found in the paper about the sequencer[51]. The pulser also provides a counter that can read PMT TTLs corresponding to atomic fluorescence. The incoming TTLs can be collected in groups triggered by the internal TTL "Readout Counts" channel or time tagged with 10 ns resolution and sorted later.

4.4.2 DACs

The DACs used in this project are the AD660 16-bit chips by Analog Devices. They use buried Zener diode references and placed on a custom circuit board with a XEM6010 FPGA by Opal Kelly (same as the pulser) and up to 28 channels are available however we only populate the nine necessary for our experiment. The DAC power supplies are floated and filtered with multi-stage LC filters. The output of the DACs are sent to 4 stage RC filters and given ground near the chamber feed through conforming to a star grounding procedure in order to avoid ground loops. The output of various filter schemes can be seen in 4.12.

4.5 Software Control

The complexity of the experiment requires modular, re-usable and flexible code. To this vain we have implemented LabRAD[3] experimental control with a Python 2.7 interface. GUI's are written with the PyQt4 package and math functions are done with NumPy and SciPy packages. The control takes on a network paradigm of servers and clients to control devices. In the following I will outline some of the most important servers that we use for data saving, data analysis, and controlling hardware devices. The repositories for both common shared code and code specific the experiment described in this thesis can be found at https://github.com/CampbellGroup.

4.5.1 Data Vault

Data Vault is a server that provides access to and the ability to save data. All data can be saved with current parameters and are logged in a local file structure. Each data set is saved in a comma delimited CSV file with the number of columns corresponding the number of dimensions of the data. Alongside the CSV file a .ini file saves the date time and relevant parameters of the experiment. The data vault emits TCP-IP signals whenever data sets are started, modified or closed. This allows graphical interfaces to update dynamically with changing data.

4.5.2 Parameter Vault

Experiments in practice require tens of parameters which may change over hours or days. It is very useful not only to keep track of these parameters but also to update their values in a centralized location. Parameter Vault is a server that does just that for us. Scripts can use parameter vault to get current values of Doppler cooling powers, detuning, etc. The parameters are stored in the LabRAD registry under the Parameters folder and can be accessed either through the server or directly through the LabRAD interface.

4.5.3 ScriptScanner

In order to limit repetitive code and to provide a modular system for writing scripts a server scanning such scripts was created by Michael Ramm in the Haeffner group. We have adopted and adapted this server to suite our needs. The scriptscanner controls what experiments are being run in what order as well as pausing and scheduling. A companion client/GUI was written as well that allows user changing of parameters as well as selecting experiments and scheduling.

4.5.4 Experiment structure

All experiments written in python on are based on three levels. The lowest level is the pulse sub-sequence. Sub sequences include things like Doppler Cooling, Optical Pumping, Microwave interrogation etc. The sub sequence is where the actual DDS channels are called, and timing is specified. The next higher level is the pulse sequence. This layer concatenates sub sequences to create a final ready to program pulse sequence to the FPGA pulser. These include things like microwave Ramsey point, Dipole measurement point etc. The final layer is the experiment class. This allows one to program custom settings on all devices and program the pulser including reading and analyzing the data from a high level allowing sequences and sub sequences to remain de-cluttered. The following is an outline for these three levels.

4.5.5 Sub-sequences

In the following example a subsequence turns on required lasers for a fixed duration to Doppler cool. All variables not coded explicitly are replaced by the parameter vault at run time in order to use current values. The start and stop times are defined in such a way so they can be concatenated in the Sequence.

```
from common.lib.servers.Pulser2.pulse_sequences.pulse_sequence import pulse_sequence
from labrad.units import WithUnit as U


class doppler_cooling(pulse_sequence):

    required_parameters = [
                           ('DopplerCooling', 'cooling_power'),
                           ('DopplerCooling', 'repump_power'),
                           ('DopplerCooling', 'detuning'),
                           ('DopplerCooling', 'duration'),
                           ('Transitions', 'main_cooling_369')
                           ]

    def sequence(self):
        p = self.parameters

        self.addDDS('DopplerCoolingSP',
                    self.start,
                    p.DopplerCooling.duration,
                    U(110.0, 'MHz'),
                    U(-9.0, 'dBm'))

        self.addDDS('369DP',
                    self.start,
                    p.DopplerCooling.duration,
                    p.Transitions.main_cooling_369/2.0 + U(200.0, 'MHz') +
```

```
                p.DopplerCooling.detuning/2.0,
                p.DopplerCooling.cooling_power)

        self.addDDS('935SP',
                self.start,
                p.DopplerCooling.duration,
                U(320.0, 'MHz'),
                p.DopplerCooling.repump_power)

        self.addDDS('760SP',
                self.start,
                p.DopplerCooling.duration,
                U(320.0, 'MHz'),
                U(-2.0,  'dBm'))

        self.end = self.start + p.DopplerCooling.duration
```

4.5.6 Sequences

Sequences simply concatenate sub sequences and are the same class as sub sequences. In the following example the main cooling transition is interrogated after doppler cooling.

```
from common.lib.servers.Pulser2.pulse_sequences.pulse_sequence import pulse_sequence
from sub_sequences.DopplerCooling import doppler_cooling
from sub_sequences.DipoleInterogation import dipole_interogation
from sub_sequences.TurnOffAll import turn_off_all


class interleaved_point(pulse_sequence):

    required_subsequences = [turn_off_all, doppler_cooling, dipole_interogation]

    def sequence(self):
        self.addSequence(turn_off_all)
```

```
self.addSequence(doppler_cooling)
self.addSequence(dipole_interogation)
```

4.5.7 Experiments

The top level of this structure is the experiment class. These tend to be messier and more flexible than the lower level classes. This is where data analysis, data saving, plotting and hard coding of parameters can be performed. If a pulse sequence is used in the experiment this is where the pulser is programmed.

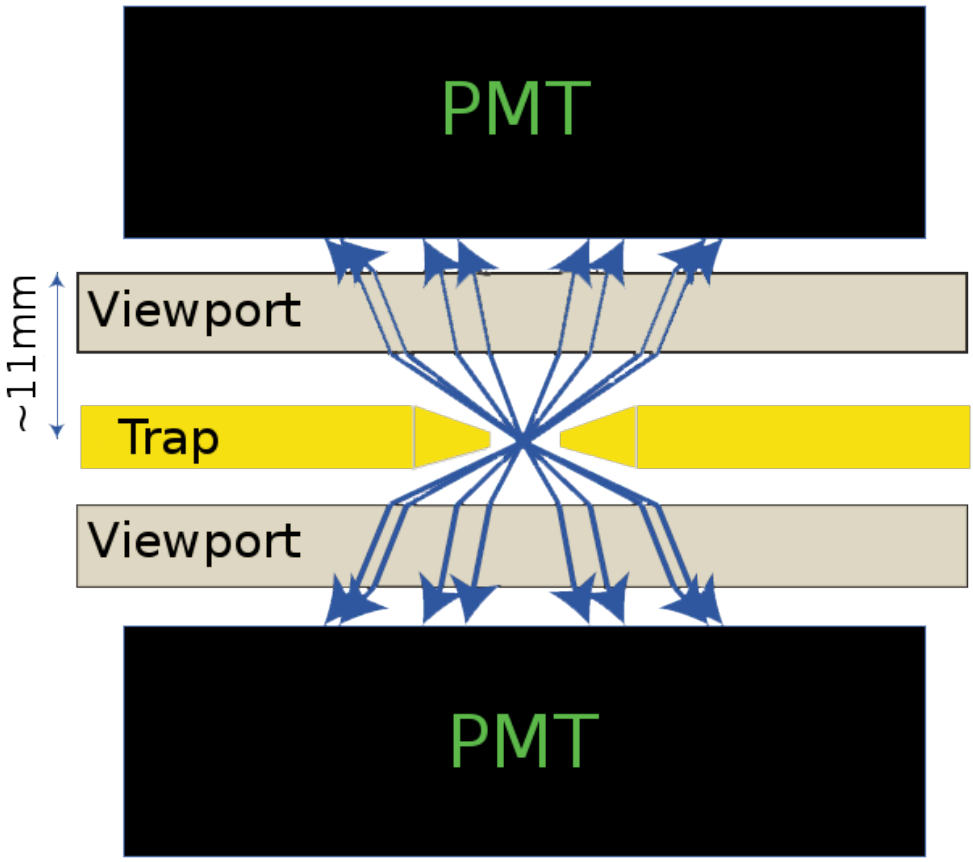

Figure 4.2: Cartoon showing the available solid angle of the trap with the two recessed viewports

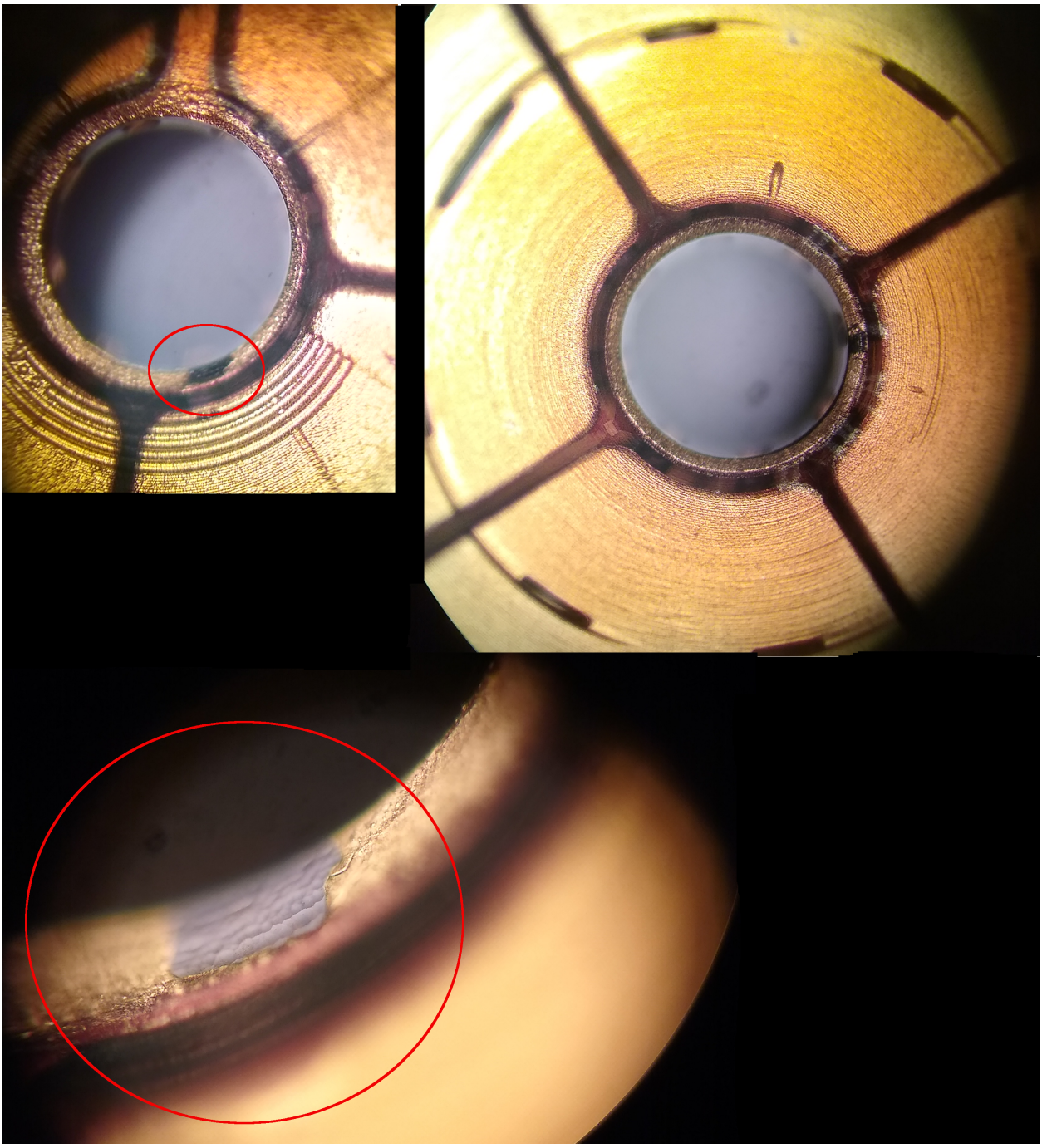

Figure 4.3: Microscope images of the first ring trap damage. The delamination of the gold is circled in red

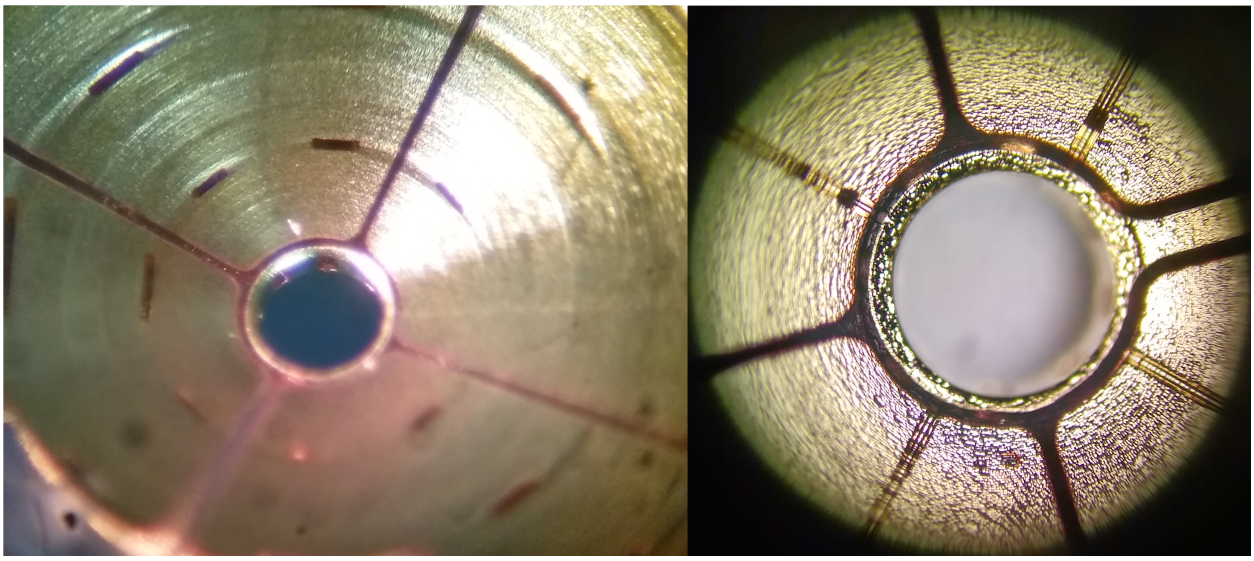

Figure 4.4: Current new ring trap microscope images showing full gold coating

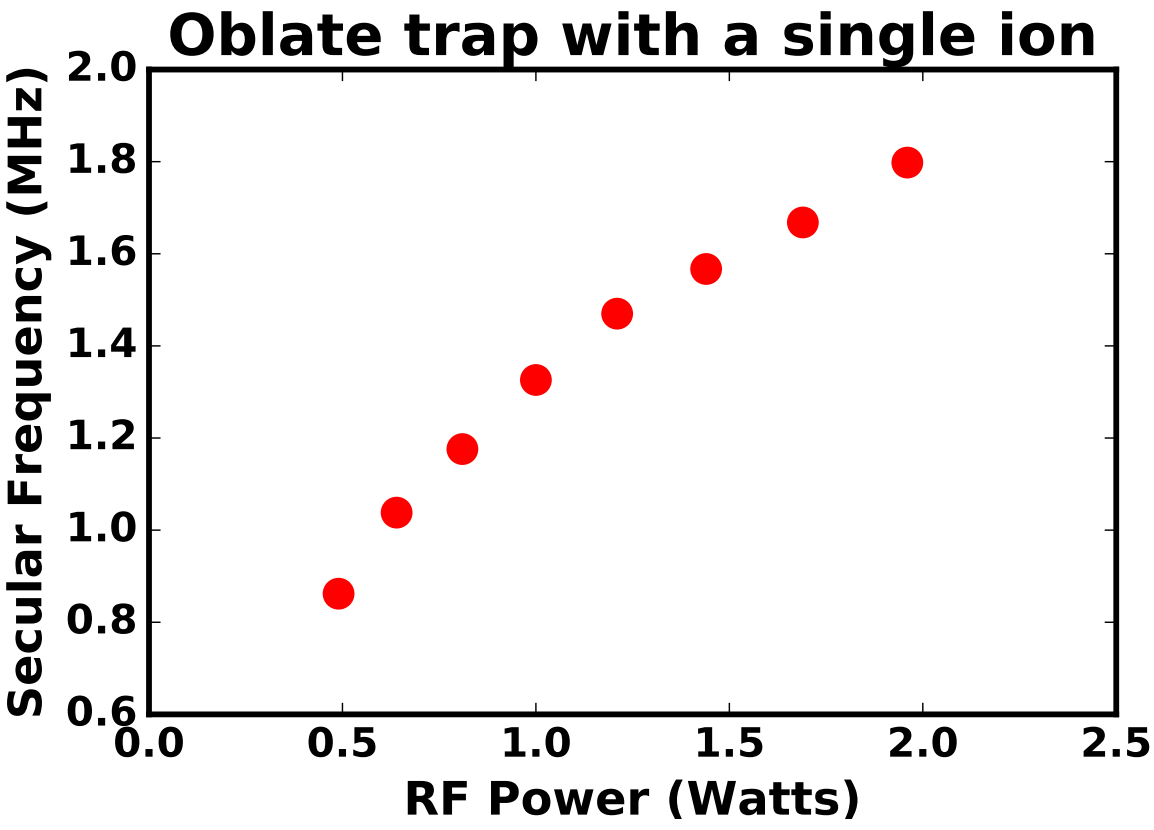

Figure 4.5: Axial secular frequency as a function of applied RF power

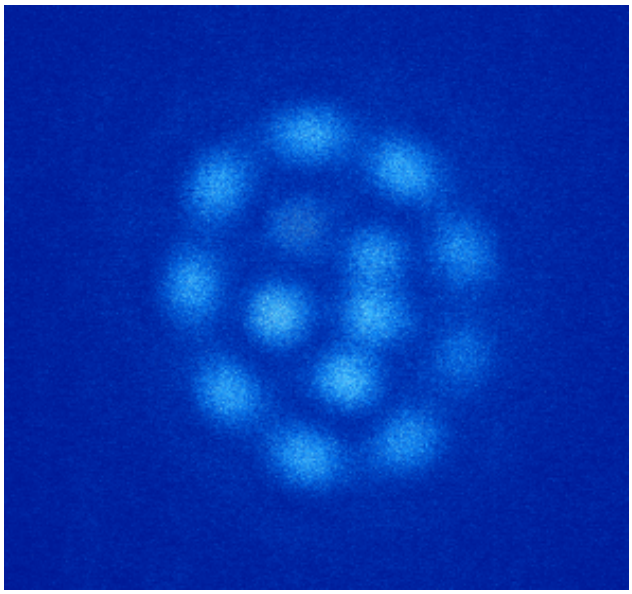

Figure 4.6: Crystal of ions where the axial confinement is too weak and the crystal breaks into a 3-D structure

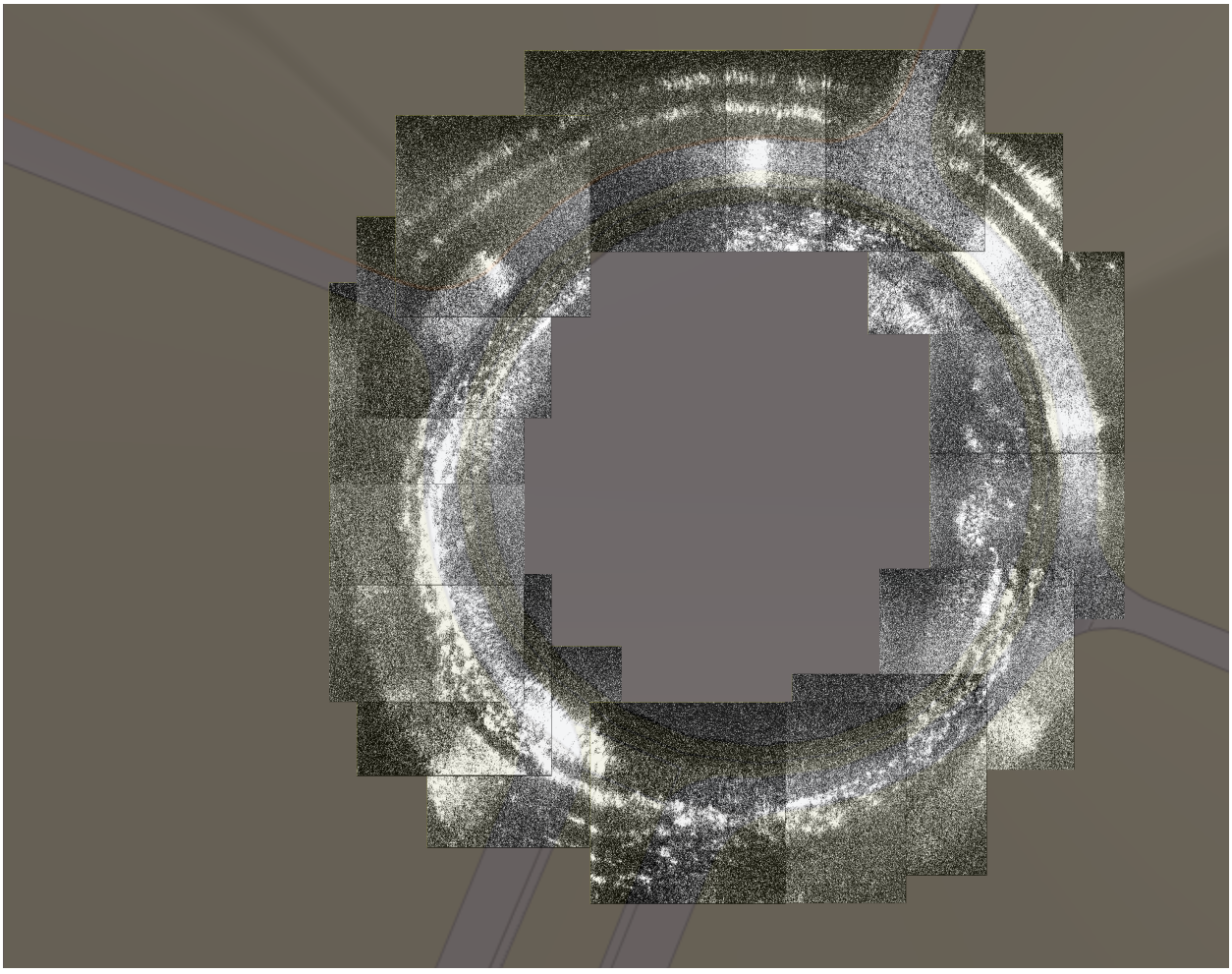

Figure 4.7: Composite image taken with EMCCD camera (iXon3). The solid works design is overlaid to show orientation and reflection which changes due to imaging and mirrors

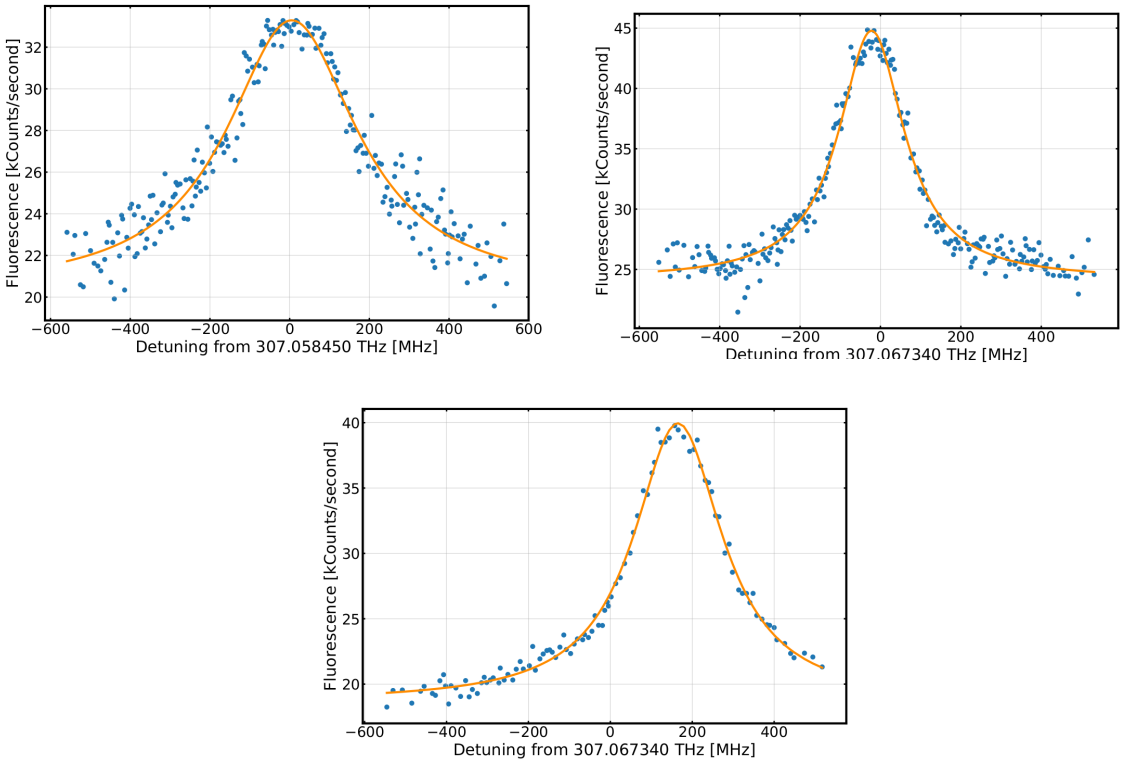

Figure 4.8: 976 nm spectrums. Upper left, F=2 to F=1. Upper right, F=2 to F=2. Bottom F=3 to F=2

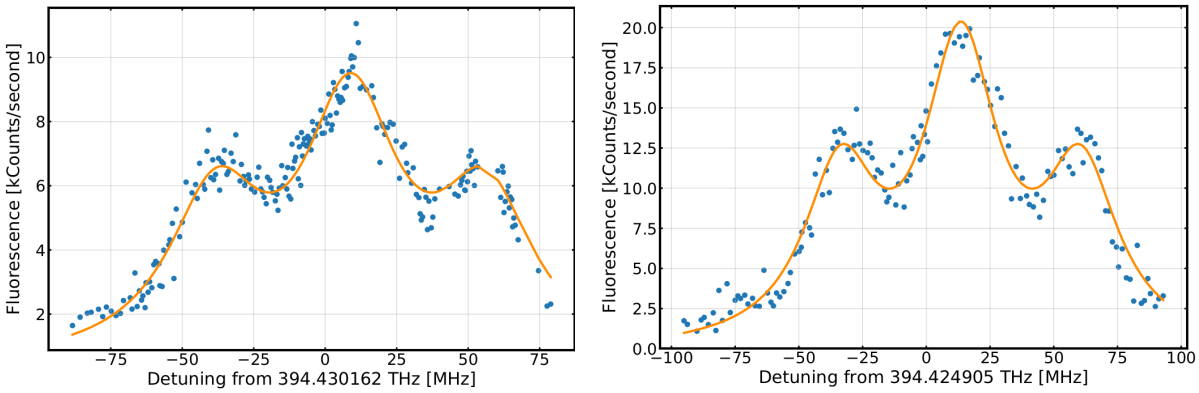

Figure 4.9: 760 nm spectrums. Left, F=3 to F=1. Right, F=4 to F=2. The spectrum is fit to a Bessel modulated Lorentzian

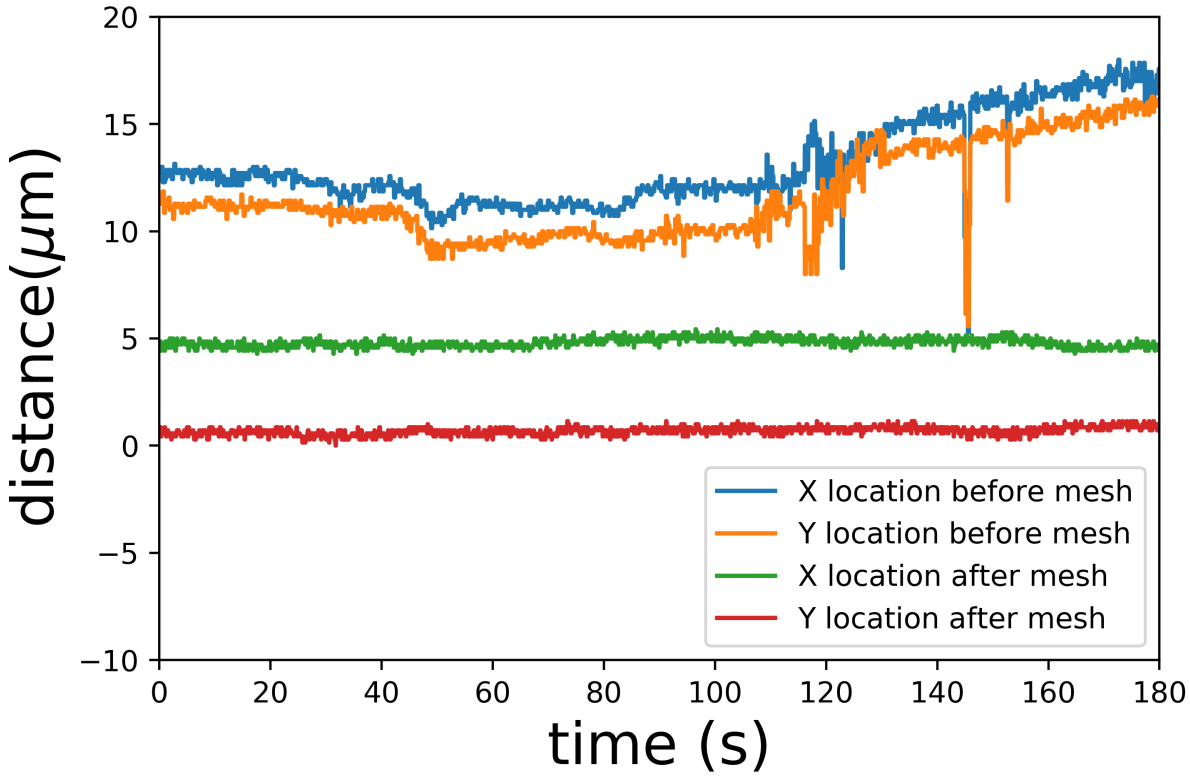

Figure 4.10: Ion drift rate with before mesh on windows (blue X, orange, Y) and after mesh is installed (green X, red Y)

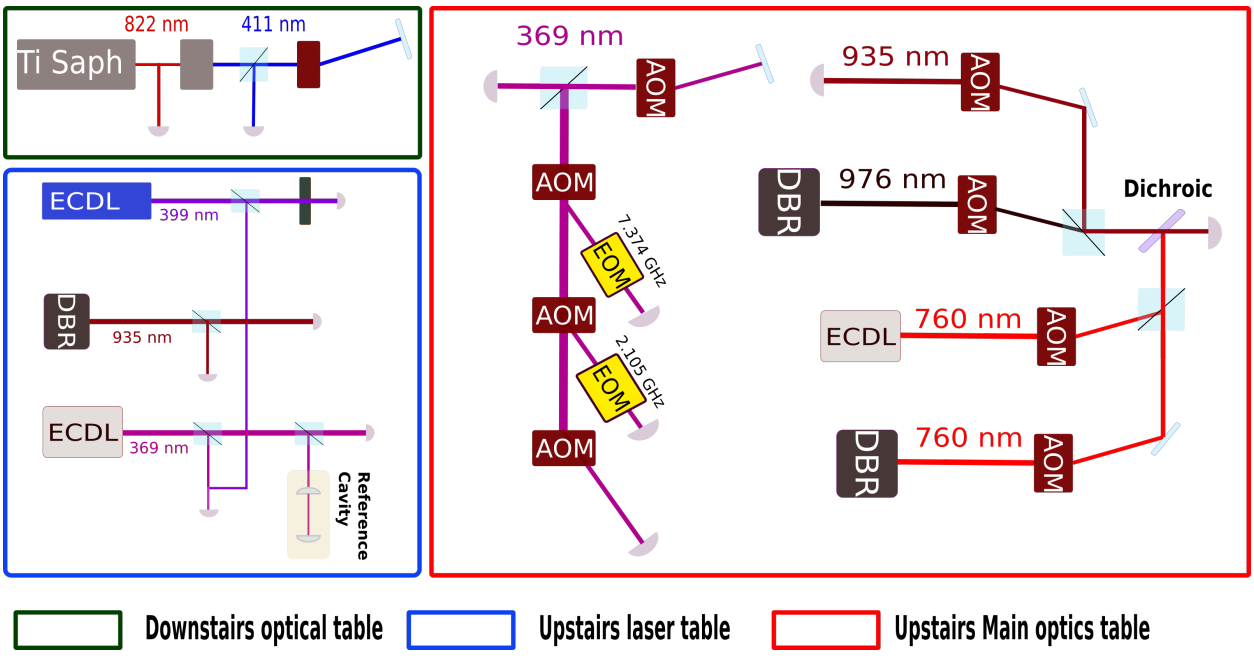

Figure 4.11: Laser setup, all lasers are measured on wavemeters and sent through single pass AOMs for switching except for the 399 nm which is shuttered with a hard drive switch. The 369 nm laser is double passed prior to going to the different single pass AOMs for switching. The double pass allows for fast frequency switching as well as slow feedback for cavity drifts.

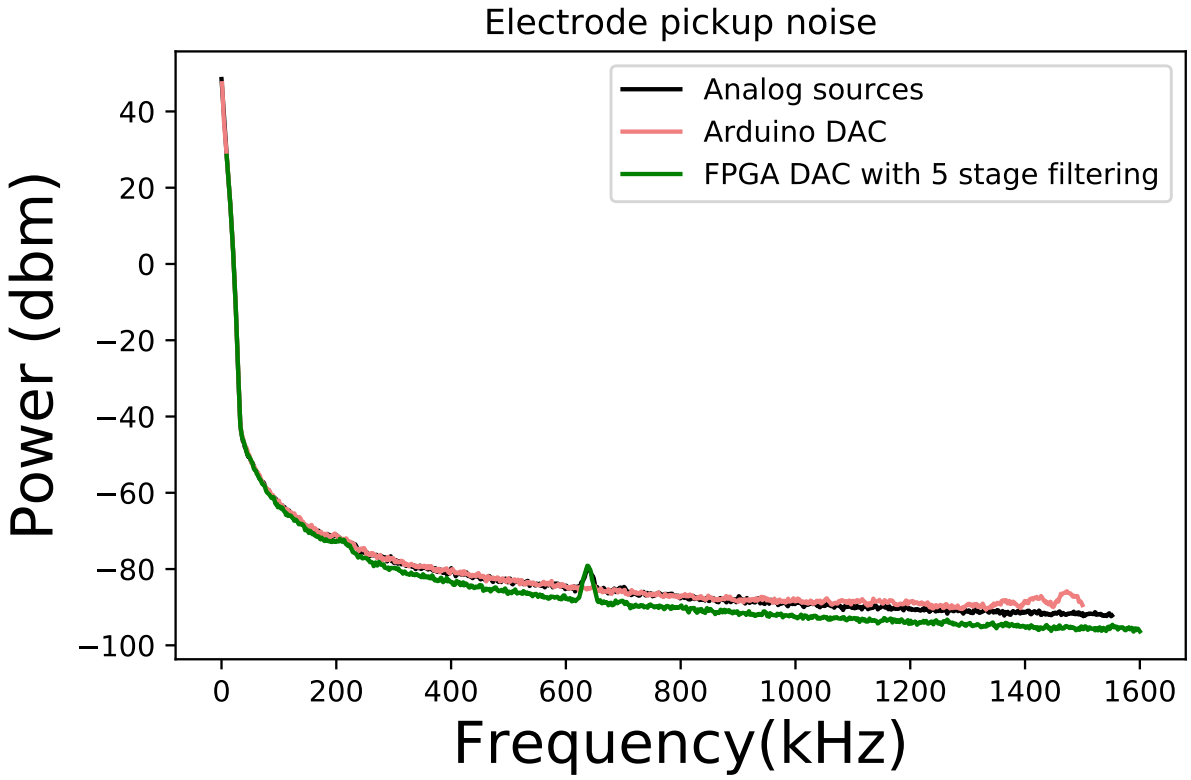

Figure 4.12: Power spectral density of noise on a single DC electrode with different filtering. Current operation is done with filters corresponding to the green trace and the bump at 630 MHz is due to electric noise from the ixon EMCCD camera and disappears when communication is removed

CHAPTER 5

2D Crystals

The oblate spheroid potential of the trap used in this thesis leads to natural trapping of 2D crystals (see figure 5.1). These interesting structures could be useful for studying 2D physics such as Ising models[12]. In the following we explore why geometries are possible in this trap and how metastable configurations (unique to 2D) can form.

Figure 5.1: Images of trapped ions configurations in our experiment, 1 to 9

5.1 Configuration simulations

The potential created in our trap can be approximated as[68]

$$\psi(x,y,z) = \frac{q^2 V_{0,RF}^2}{m\Omega_{RF}^2 r_0^4}(x^2+y^2+4z^2) \tag{5.1}$$

where q is the charge, $V_{0,RF}$ is the amplitude of the RF, m is the mass and r_0 is a characteristic length (in our case 512μm). Beyond this potential there is an interaction between the ions in the trapped described by the Coulomb potential. Each ion interacts with every other ion such that the interaction energy for each ion is

$$E_i = \sum_{i \neq j} \frac{q^2}{4\pi\epsilon d_i} \tag{5.2}$$

5.1.1 Annealing algorithm

By calculating the position energy (eq 1.1) and the interaction energy (1.2) we can find the total energy and minimize this. This is done by Yoshimura[68] for our trap geometry, however for a large range of ion numbers it is simple enough to write an annealing algorithm with a cost function that finds a local minimum quickly. The procedure is as follows:

1. ions are placed randomly in space and the total configuration energy is calculate
2. the ions are moved by a variable amount in random directions
3. if the energy has decreased the result of step 2 is accepted and step 2 is repeated
4. if the energy increases the results of step 2 are rejected and step2 is repeated

A package for doing this is written in python and located on our group github at . This allows for control over the potential, trap asymmetry, and initial ion configurations.

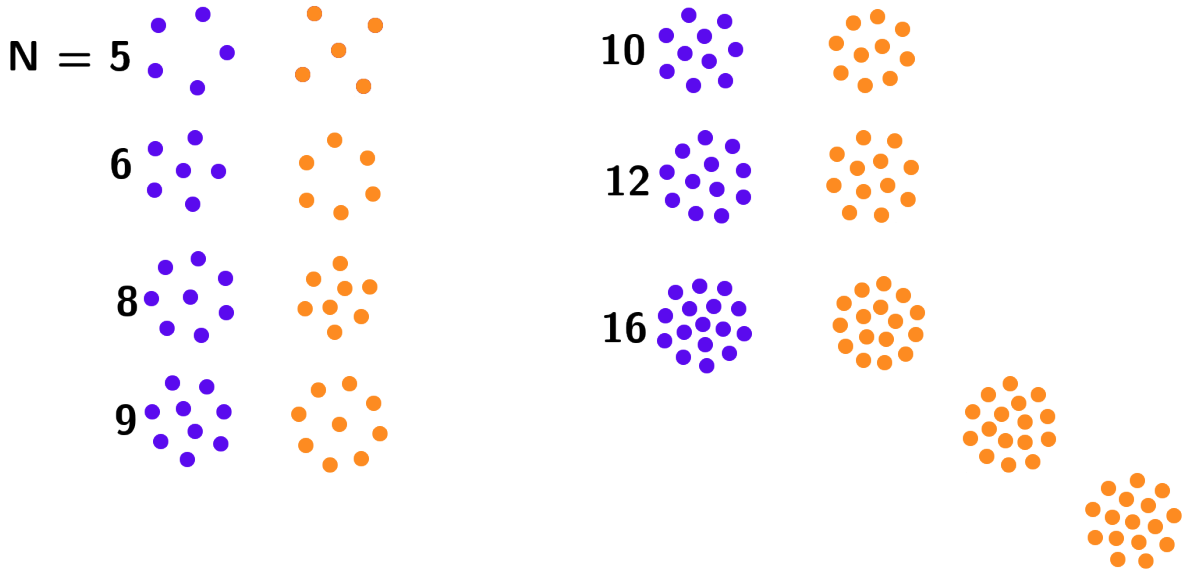

Figure 5.2: Simulated stable (purple) and metastable (orange) configurations

5.1.2 Metastable Configurations

When we perform these minimizations, we find the ions not only find global minimums when compared to previous calculations[6] but also metastable states see figure 5.2. While the N=5 state does exist it seems the barrier for it to fall into the stable pentagon is much lower than the temperature of our crystals since we never observe this state. The N=6 state on the other hand can be observed in both the stable and metastable states.

We modify the code to allow a single ion to be pinned in space and calculate the configuration energy. By dragging this ion from the center of the crystal to the edge we can plot the configuration energy as a function of this coordinate, see figure 5.3. While this almost

certainly is not the path the ions take during this transformation it should give an order of magnitude picture of the barrier height.

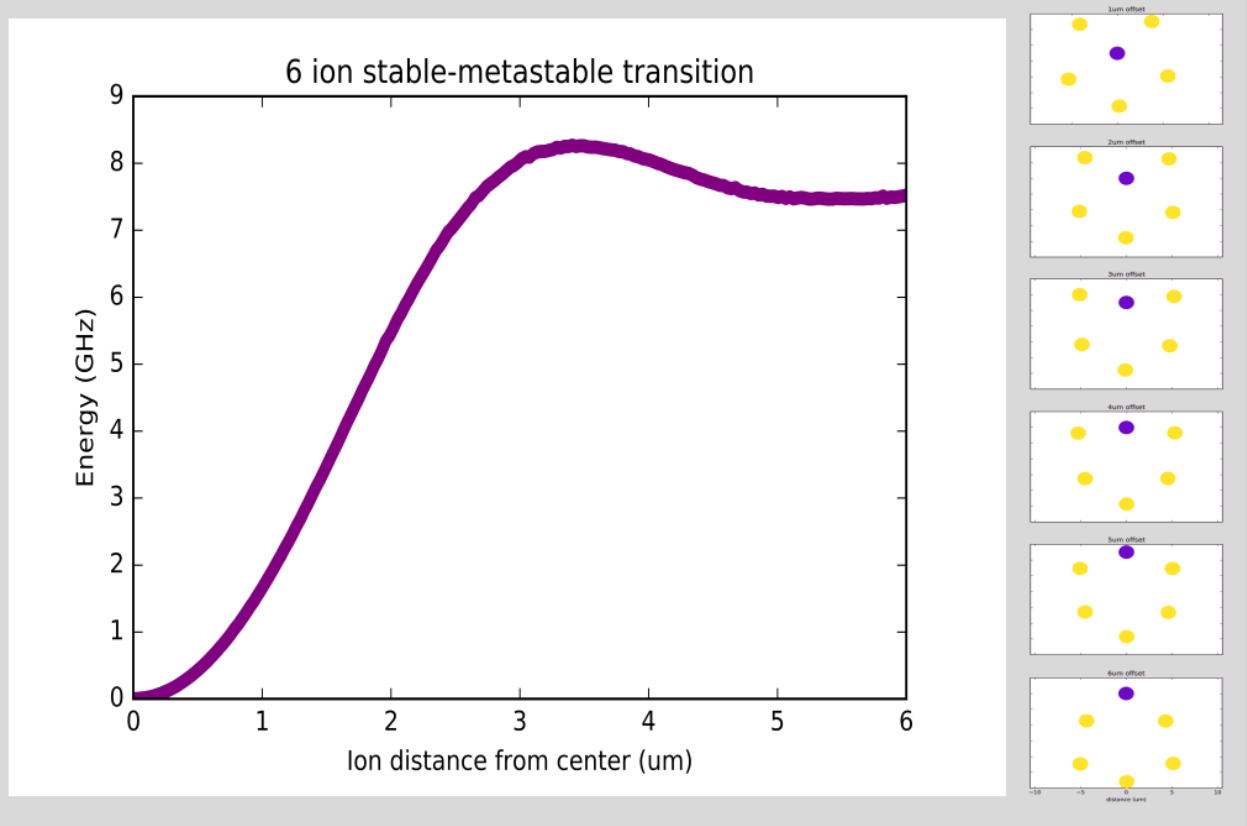

Figure 5.3: Potential barrier for configuration of ion dragged along the z axis

Interestingly as the symmetry of the trap confinement is changed the metastable state and stable state swap roles. as can be seen in figure 5.4. This leads to a hysteric path dependence while squeezing. If the ion crystal begins in the metastable state it will stay adiabatically in that state throughout the squeezing process, however if it is in the symmetric grounds state the ion crystal will stay in this state even after it is metastable until a phase transition occurs discontinuously. See 5.5 for simulations of this discontinuity.

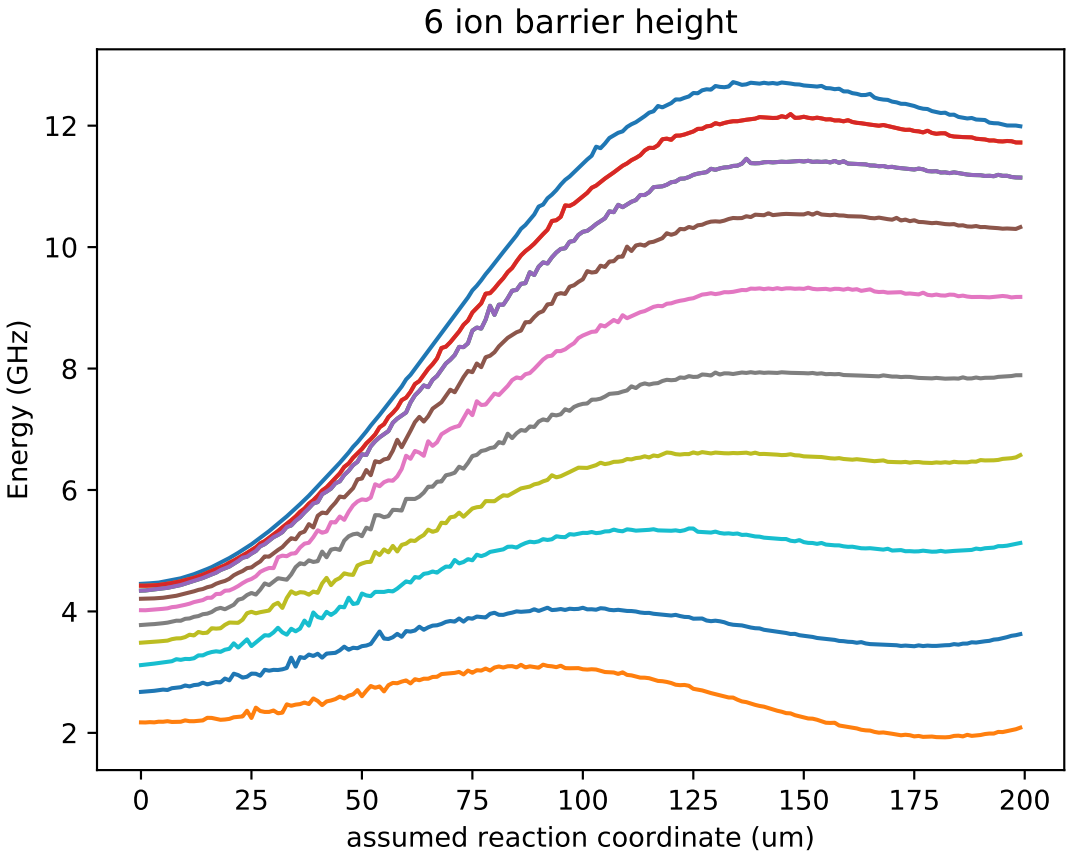

Figure 5.4: 6 ion barrier height at different asymmetries

5.2 Hopping between stable and metastable states

If we fix the asymmetry such that it is near the swapping points of the two configurations in energy we see hopping between the two states, depending on which side of the crossing we are at we spend time in either the symmetric ground state or the asymmetric ground state see figure 5.6

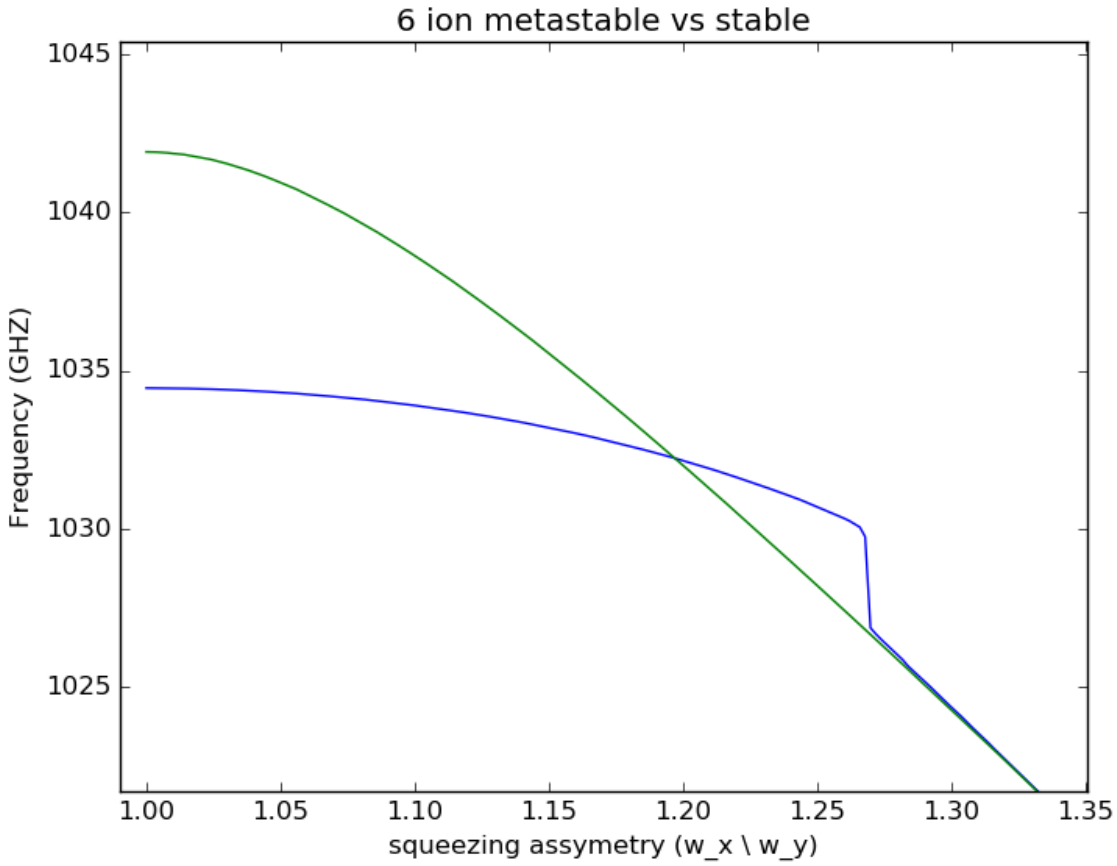

Figure 5.5: Energy of the face centered pentagon (green) and the hexagon (blue) for different radial trap symmetries

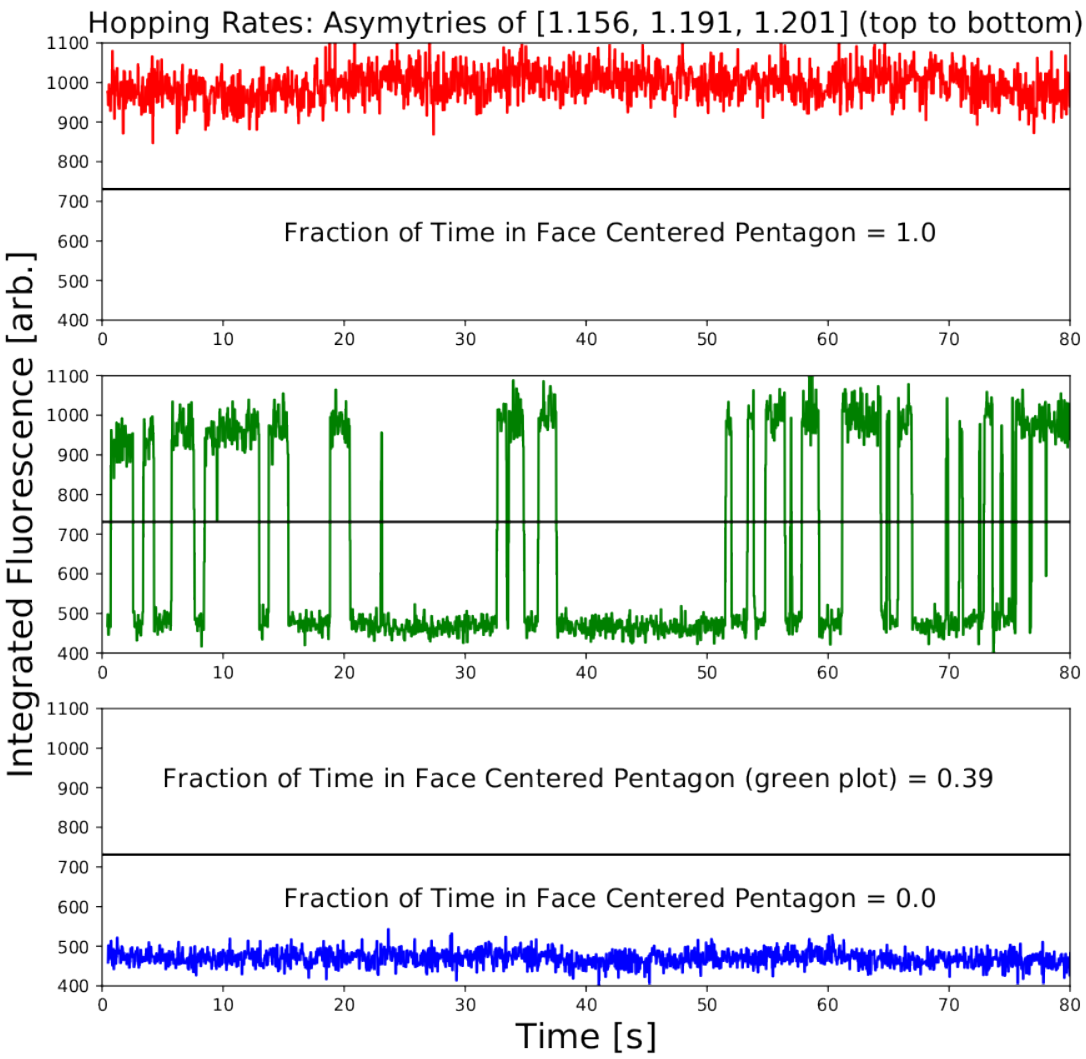

Figure 5.6: Hopping rate with different asymmetries. We see that with a more symmetric potential (red) the ions stay in the face centered pentagon whereas with large asymmetry (blue) the ions stay in the hexagonal configuration. Near the crossing (green) the temperature of the crystal is large enough to hop between the two configurations

CHAPTER 6

Phonon Lasing

Mode locked lasers have typically been used for highly nonlinear purposes such as engraving or employed as frequency combs for references to atomic transitions. Mechanical forces have not been generally applied to cold atoms with mode locked lasers due to the small per comb tooth power in short pulse duration lasers. Recently however in order to bring atomic physics deep into the UV spectrum, Mode locked lasers have been leveraged for MOT's[37], Doppler Cooling[19] and in this work, a mechanism dubbed phonon lasing[19] which allows for cooling of ions to near Doppler temperatures with broadband pulses. Pulsed lasers can be easily doubled deep into the UV spectrum allowing optical power to be produced at colors unattainable with CW lasers. By bringing the toolbox of AMO into the UV species such as Hg^+, Al^+, He^+, and highly charged ions [65, 27, 46, 66] could benefit from easy to generate doubled mode locked light. To this end we set out to laser cool Yb ions at 369 nm with a frequency comb. While the cooling transition of Yb^+ is not deep in the UV, it provides a simple test bed for applying mechanical forces to ions on a species that could be simply Doppler cooled with standard lasers.

6.1 Tsunami TiSaph

The ML laser for this work is a commercial picosecond Ti:sapphire laser oscillator [1] with a repetition rate of $f_r = 1/T_r = 81.553$ MHz. The center frequency of the laser is set near 405.645 THz, and the output is frequency doubled via single-pass through a 0.8 cm LBO crystal cut for Type I phase matching for SHG of 760 nm light, generating an average UV

[1] SpectraPhysics Tsunami

power of around 9 mW at $\lambda \approx 369.5$ nm. The laser bandwidth (> 10 GHz) far exceeds the natural linewidth ($\gamma \equiv 1/\tau = 2\pi \times 19.7$ MHz) and Zeeman splitting (< 5 MHz) of the $^2P_{1/2} \leftrightarrow {}^2S_{1/2}$ transition in Yb^+. The peak ion fluorescence observed indicates that the optical power per comb tooth at the ion is ≈ 1.4 μW. For the experiments in this chapter, we simultaneously illuminate the trapped ion with the mode-locked laser at 369.5 nm and a CW repump laser at 935 nm that has no observable direct mechanical effect on the ion.

6.2 Visibility

The transition driven in this work is the $^2S_{1/2} \longrightarrow^2 P_{1/2}$ dipole transition in $^{174}Yb^+$. The excited state lifetime is 8.12 ns[59]. Since the repetition rate of our laser corresponds to 12.5 ns, the same order as the lifetime, one might expect that any optical pulse to pulse coherence may die out. The probability of a decay event after excitation is given by

$$\rho_{gg} = 1 - e^{-\frac{T_R}{\tau}} \tag{6.1}$$

and corresponds to the ion decaying 78% of the time. However, while the probabilities decay as the lifetime, the of diagonal elements which correspond to the coherences decay half as fast. The quasi-steady-state scattering rate for an atom at rest illuminated by a resonant comb of uniformly intense teeth ($\tau_{\text{pulse}} \ll T_{\text{r}}$) is given by [22, 32, 4]

$$\Gamma_{\text{comb}}(\delta) = \frac{1}{T_{\text{r}}} \frac{\sin^2\left(\frac{\theta}{2}\right) \sinh\left(\frac{T_{\text{r}}}{2\tau}\right)}{\cosh\left(\frac{T_{\text{r}}}{2\tau}\right) - \cos^2\left(\frac{\theta}{2}\right) \cos(\delta T_{\text{r}})}, \tag{6.2}$$

where δ is the angular detuning of a reference tooth from resonance ($\delta \equiv \omega_{\text{tooth}} - \omega_{\text{atom}}$) and θ is the pulse area, defined as the integral of the instantaneous Rabi frequency for a single pulse, $\theta \equiv \int \mathrm{d}t \Omega(t)$.

We define a visibility to quantify what contrast we may expect to see as a single tooth is scanned across resonance. $V \equiv (\Gamma_{\text{max}} - \Gamma_{\text{min}})/(\Gamma_{\text{max}} + \Gamma_{\text{min}})$, where Γ_{min} and Γ_{max} are the minimum and maximum scattering rates as the comb is scanned over a range of $\Delta f = 1/T_{\text{r}}$.

From Eq. 6.2, we find

$$V = \cos^2\left(\frac{\theta}{2}\right) \operatorname{sech}\left(\frac{T_r}{2\tau}\right), \tag{6.3}$$

For our parameters we expect the visibility to be 0.77 even though 78% of the population has decayed between pulses.

6.3 Phonon lasing

Figure 6.1 shows the 369.5 nm fluorescence collected from a trapped ion as the teeth of the optical frequency comb illuminating it are scanned. The data are taken for 100 ms of illumination per point so that the ion's motional temperature reaches steady-state for each frequency shown, and background counts ($\approx$ 170 kcps) have been subtracted by taking the difference between the PMT signal with and without the 935 nm repump laser.

The fluorescence in figure 6.1 tracks the ion's (power-broadened) rest-frame lineshape (Eq. 6.2) well when the near-resonant tooth is on the red side of atomic resonance ($\delta < 0$), which is the regime in which cw-like Doppler cooling actively cools the ion's motion. As the near-resonant tooth crosses resonance and becomes blue-detuned ($\delta > 0$), the fluorescence no longer follows the rest-frame prediction of Eq. 6.2, and an additional peak appears. As shown in Fig. 6.1, the ion image in this case spreads out along a principal axis of the trap with an amplitude of $x_0 = (4.9 \pm 0.5)$ μm. This fluorescence image matches well to the classical probability distribution of a harmonic oscillator convolved with the point-spread function of our imaging system (see, *e.g.* figure 6.2), which shows that the ion is oscillating with fixed amplitude. The classical harmonic oscillator state is what has been named a phonon laser in this case. The non-linear gain of blue detuned teeth adding energy with red detuned teeth removing energy leads to this steady state oscillation. The power delivered and removed in this process can be modeled as

$$\frac{\mathrm{d}E}{\mathrm{d}t} = -\beta(E)\frac{2E}{m} + S(E). \tag{6.4}$$

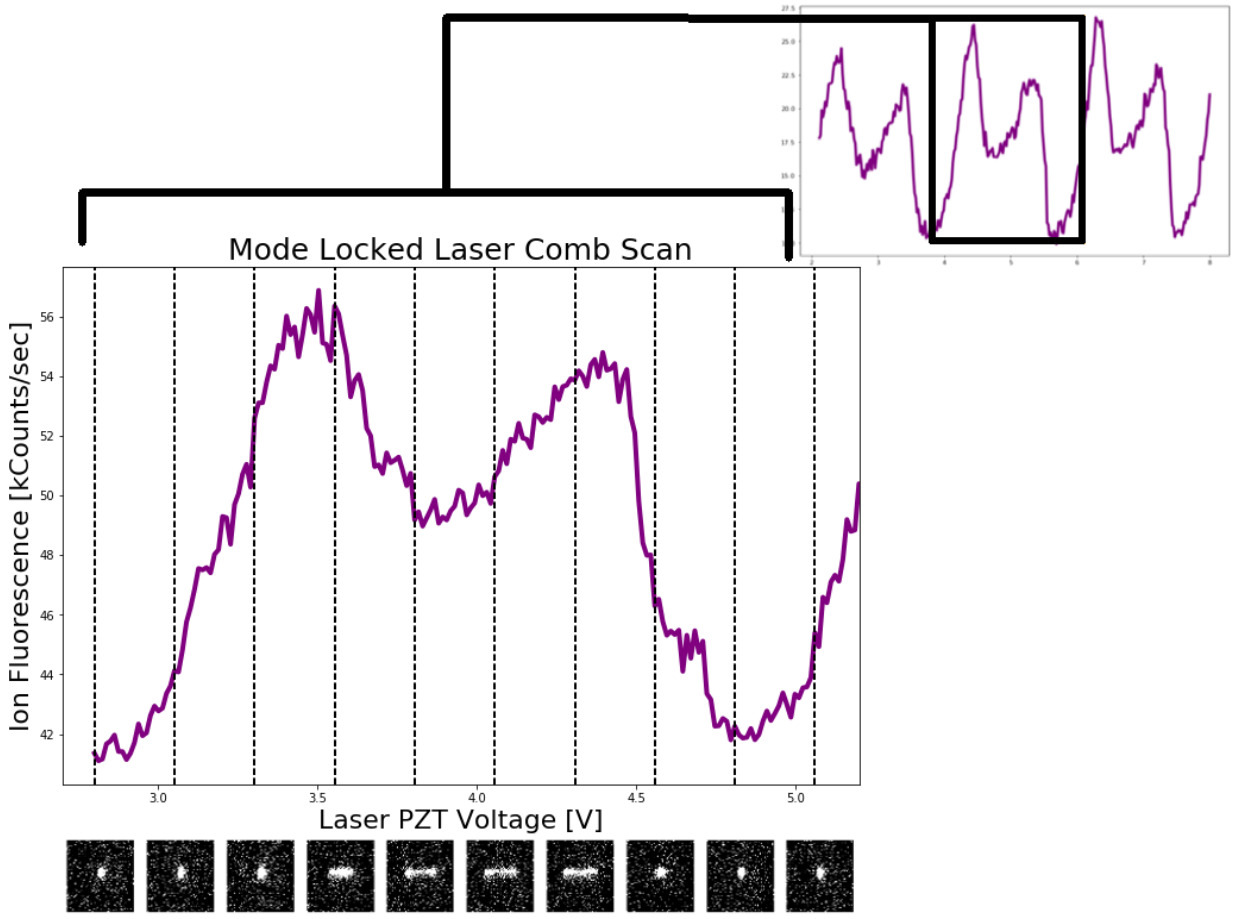

Figure 6.1: Fluorescence spectrum (in kilocounts per second) from a single trapped ion illuminated by an optical frequency comb. The voltage corresponds to moving the laser cavity and thus scanning the teeth, this repeats every 2V. When the near-resonant tooth is red detuned ∼3.2V, the ion is Doppler cooled near the ground state and the spectrum follows the rest-frame lineshape. When the near-resonant tooth is blue detuned ∼4V, the ion oscillates with a fixed amplitude and the fluorescence shows clear departure from the natural rest-frame resonance shape.

where $E \equiv \frac{1}{2}m\omega_x^2 x_0^2$ is the secular energy, $\beta(E)$ is an amplitude damping coefficient which can be positive or negative, and $S(E)$ is a stochastic heating rate due to spontaneous emission and the randomness in absorption[33]. The steady state solutions to equation 6.4 leads to fixed amplitudes exhibiting discrete energy and correspond to interacting with larger detuned comb teeth.

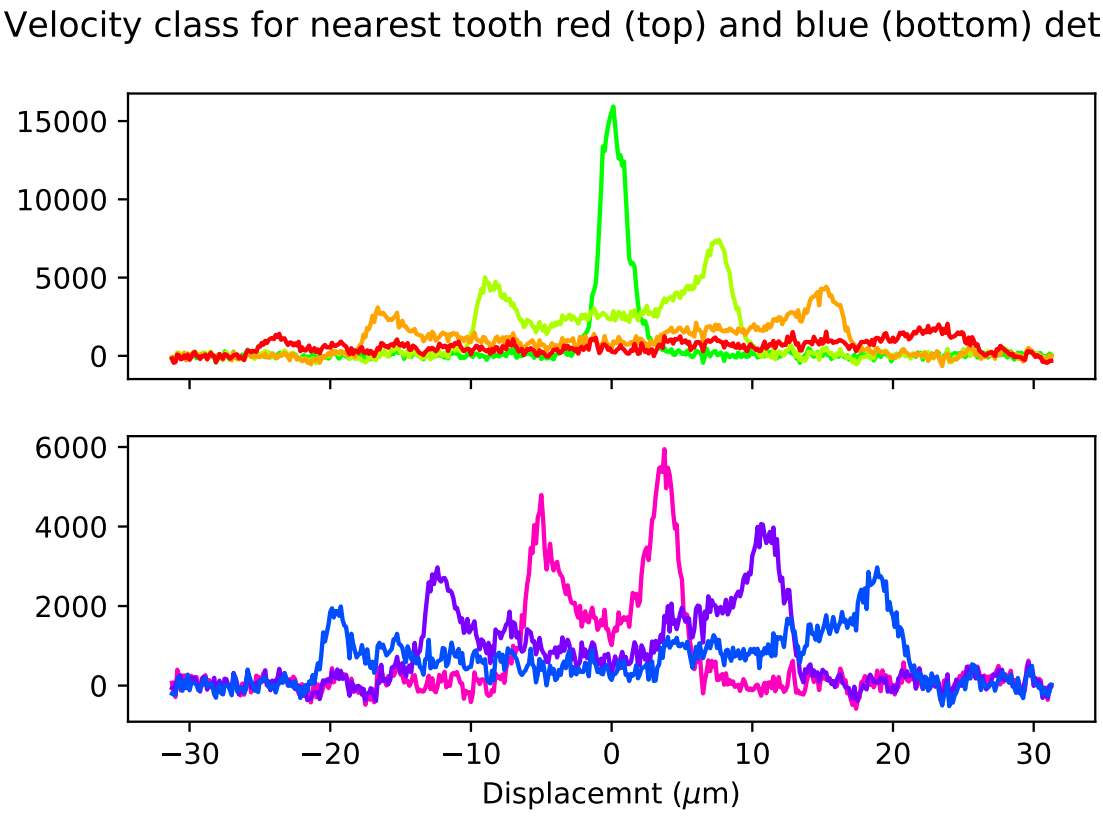

Figure 6.2: Integrated ion images at various fixed points for the nearest tooth red (top) and blue (bottom) detuned

Figure 6.2 shows these fixed amplitudes which have been intentionally excited using a signal generator attached to a DC electrode. Note that for the nearest tooth red detuned a simple Lorentzian well describes the lowest amplitude and the ion remains well localized

6.4 Injection locking

While the term "laser" in this context is nebulous we can see if this phonon laser performs some of the tasks one might expect from a laser such as injection locking. Using an aperture in the imaging system, ion fluorescence is collected from only one of the classical turning points in space, and the photons are time-tagged [51]. Figure 6.3 shows a numerical discrete Fourier transform of the recorded photon signal in the region near the secular frequency of the ion when it is in the lowest amplitude for blue detuning. A narrow peak appears at the frequency of a small sinusoidal voltage that was applied to one of the trap electrodes (the injected signal), and the broad peak is the free-running phonon laser spectrum. When the injected oscillation frequency is within the phonon laser's gain profile, almost all of the gain is dedicated to amplifying the injected signal, and the phonon laser locks on to the injected signal in frequency and phase. [42, 41, 30].

6.5 Loading crystals and laser cooling

One very unique effect of using this comb for laser cooling is that the ion remains in the trap and relatively cold for all laser detunings (Figure 6.1). This means that within an uncertainty of ∼10GHz on the cooling laser envelope driving a 20 MHz transition, we are able to load and laser cool ions to near Doppler temperatures regardless of teeth positions. This provides and exciting prospect for exotic UV ions whose transitions may not be known to this precision and relaxes the constraint of needing to know the absolute frequency of the strongest interacting comb tooth. We have successfully loaded and cooled single ions and crystals while using only pulsed laser light at 369 nm.

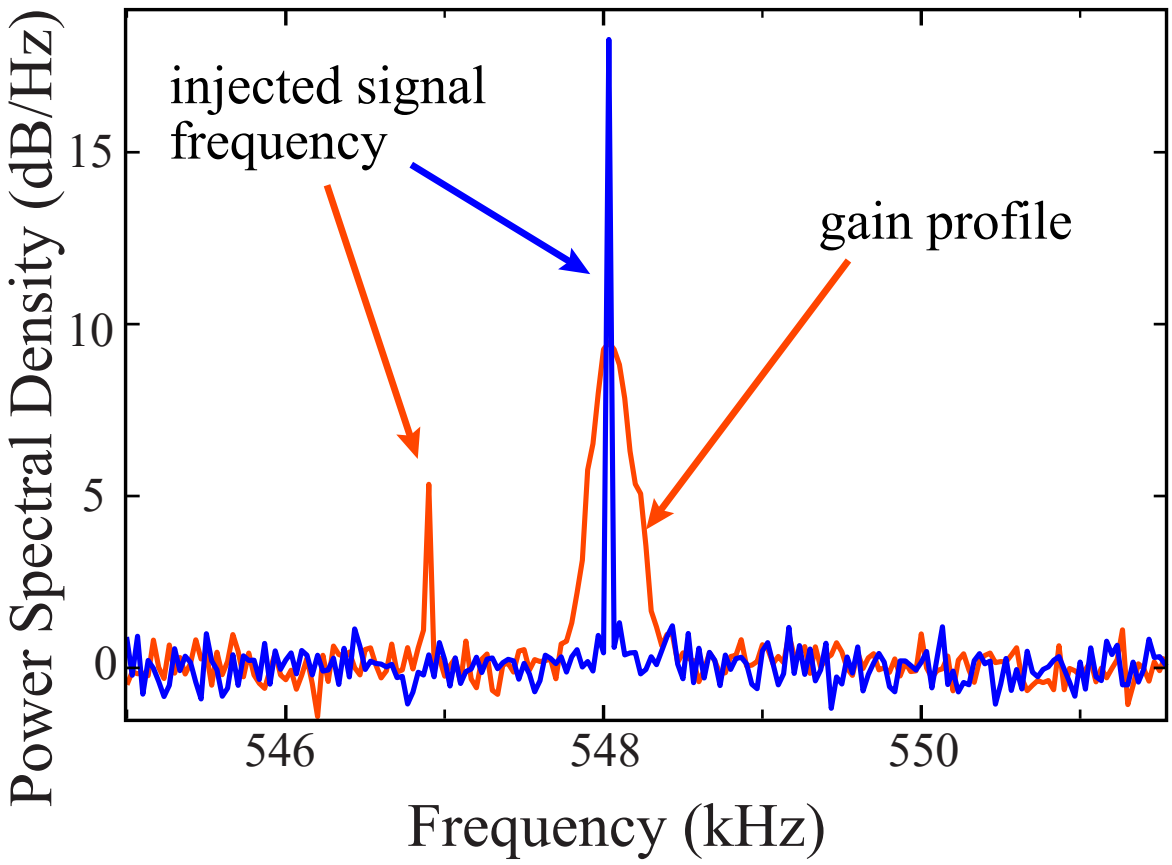

Figure 6.3: Acoustic injection locking of the x_1^* fixed point phonon laser when the near-resonant tooth is blue detuned. When the frequency of an injected signal is moved from outside (orange) to within (blue) the phonon laser's gain bandwidth, it is amplified at the expense of other frequencies.

CHAPTER 7

Shelving State Detection

The standard nuclear spin 1/2 state detection scheme described in chapter 2 works well for most current applications. However, it should be noted that the best shown SPAM fidelity with this scheme 99.931(6)%[16] is worse than the best single qubit gate fidelity (99.9999% [29]) and within one sigma of two qubit gate fidelity (99.91(6)%[35]). While error correcting schemes can limit the necessity of high fidelity SPAM, current systems are not error corrected and suffer from SPAM errors on the same footing as gate error. In the following we describe and demonstrate a method to increase the SPAM fidelity in $^{171}Yb^{+}$. This method uses incoherent optical pumping to hide population from the cooling cycle allowing for the elimination of off-resonant effects as well as essentially unlimited detection times relaxing all constraints on state detection. Of course, there is never free lunch and the cost of this method is time. The shelving scheme takes ∼100ms. While this is much longer than any other timescale in a single operation, we believe that for large gate depths or quantum simulations with long interaction times, the benefits of this scheme will be worth the constant time overhead.

7.1 Narrow-band optical pumping

Optical pumping is normally performed on a strong dipole transition ($\Gamma \sim 2\pi \times 20$MHz). This is because weak transitions tend to decay extremely slowly (∼1s). This does not have to be the case however, especially if there exists a leaky dipole decay from the excited state. We exploit two such transitions in Yb^{+} to allow us to cycle a narrow transition incoherently until the population leaks into a third state. The first such transition is the $^2S_{1/2} \longrightarrow {}^2D_{5/2}$

at 411 nm (see figure 7.1). The unique low lying F state in Yb^+ provides a dipole decay path at 3.4 μm on the $^2D_{5/2} \longrightarrow {}^2F_{7/2}$. Due to this decay path along with the transition being higher frequency than other hydrogen like ions, the lifetime of this state is only (6.9-7.4) ms[64, 69]. The second transition we drive is the $^2F_{7/2} \longrightarrow {}^1[3/2]_{3/2}$ E2 transition at 760 nm. The excited state of this transition can dipole decay to the $^2S_{1/2}$ state at 289 nm. This decay has a very short 28.6 ns lifetime [10]. This gives the total line-width of the transition at 5.5 MHz.

7.2 Scheme

The goal of the scheme is to transfer the entirety of the $^2S_{1/2}$ F=1 manifold into the long lived F level without decaying into the $^2S_{1/2}$ F=0 state or exciting the F=0 population. This can be accomplished by leveraging the quadrupole selection rules. We drive the $^2S_{1/2}$ F=1 state to the $^2D_{5/2}$ F=3 transition. Since $\Delta F = 3$ transitions are not allowed the population will decay either into the F state with 83% [64] probability or into the $^2S_{1/2}$ F=1 and can be continually cycled until all population is shelved.

7.3 Limits

We model this incoherent process with simple rate equations. Consider the three levels of Yb^+, $(S_{1/2}, D_{5/2}, F_{7/2})$ with populations ρ_S, ρ_D, ρ_F respectively. With $\gamma = \frac{1}{\tau}$ being the decay rate and η being the branching ratio into the F state, then the population accumulated in the F state per unit time is

$$\frac{d\rho_F}{dt} = \gamma\eta\rho_D \tag{7.1}$$

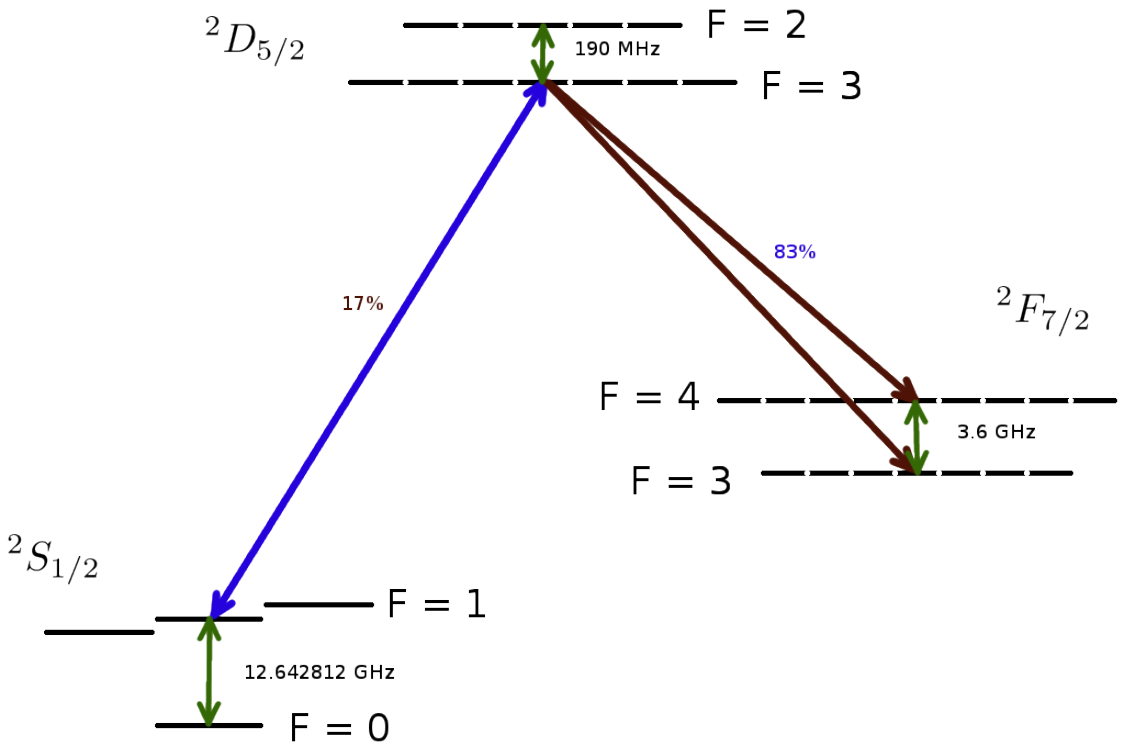

Figure 7.1: Shelving scheme with the 411 nm laser. Population is transferred on the F=1 $\longrightarrow$ F=3 cycling transition.

we work in the limit where the 411 nm quickly saturates the transition such that the population in the S and D manifolds are the same.

$$\rho_S = \rho_D \tag{7.2}$$

and therefore the population in ρ_f can be written in terms of ρ_D only

$$\rho_F = 1 - \rho_S + \rho_D = 1 - 2\rho_D \tag{7.3}$$

plugging ρ_D into (7.1)

$$\frac{d\rho_F}{dt} = \frac{\gamma\eta}{2}(1 - \rho_F) \tag{7.4}$$

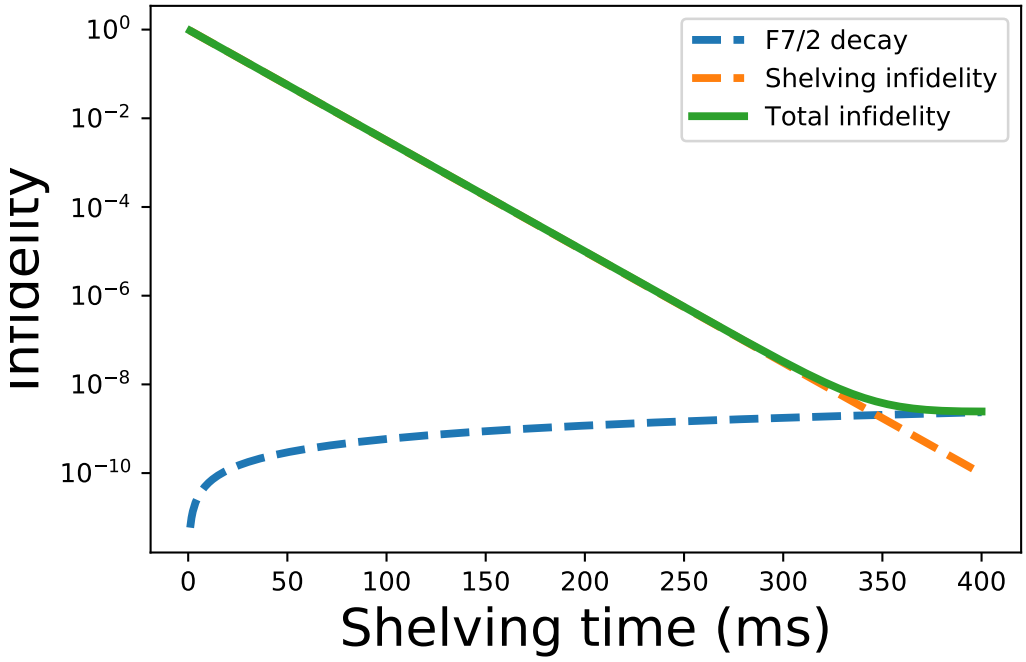

Figure 7.2: Fidelity as function of shelving time. As shelving time is increased the fidelity increases(orange) however eventually the finite lifetime of the ${}^2F_{7/2}$ state will have a non-negligible effect (blue) and the total fidelity (green) will decrease.

integrating...

$$\rho_F = 1 - \exp\left[-\frac{\gamma\eta}{2}t\right] = \mathcal{F} \tag{7.5}$$

Equation (7.55) is the shelving fidelity as a function of time. One way to improve the shelving time is with coherent pulses since the $1/2$ in the exponent of equation 7.5 comes from the assumption of an incoherent process, assuming a fast pi-pulse we modify equation (7.2) and say at $t = 0$

$$\rho_D = 1; \rho_S = 0; \rho_F = 0 \tag{7.6}$$

and for all time probability is conserved so

$$1 = \rho_D + \rho_F + \rho_S \tag{7.7}$$

$$\frac{\rho_F}{\rho_S + \rho_F} = \eta \tag{7.8}$$

then

$$\frac{d\rho_F}{dt} = \gamma\eta[1 - (\rho_F + \rho_S)] \tag{7.9}$$

using (7.8)

$$\frac{d\rho_F}{dt} = \gamma\eta(1 - \frac{\rho_F}{\eta}) \tag{7.10}$$

or

$$\frac{d\rho_F}{\eta - \rho_F} = \gamma dt \tag{7.11}$$

integrating gives us

$$\rho_F = \eta(1 - \exp[-\gamma t]) \tag{7.12}$$

equation (7.12) and equation (7.5) are plotted in figure 3.

Given these rates the best way to improve speed would involve performing a pi-pulse and then waiting for the optimal time, when the population inversion benefit is lost, to switch to incoherent pumping. This occurs when the derivatives or rate of population transfer to F state between coherent and incoherent excitation equal each other. The coherent rate is

$$R_{coherent} = \gamma\eta \exp[-\gamma t] \tag{7.13}$$

and the incoherent rate (the derivative of equation (7.5)) is

$$R_{incoherent} = \frac{\gamma\eta}{2} \exp\Big[-\frac{\gamma\eta}{2}t\Big] \tag{7.14}$$

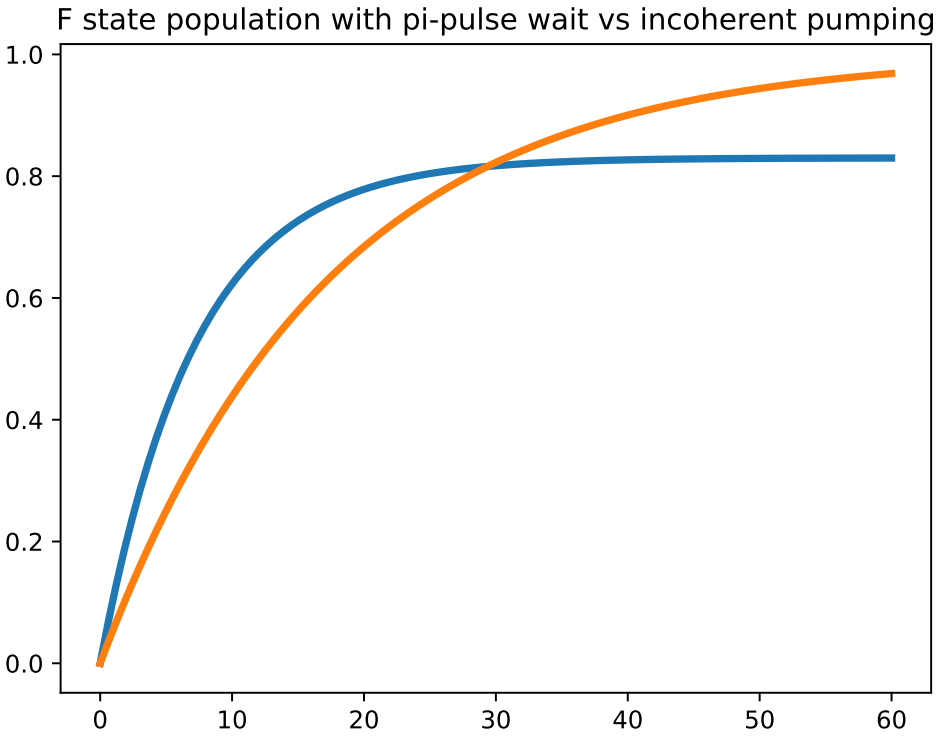

Figure 7.3: F state population transfer with coherent pi pulse (blue) or incoherent shelving(orange). For the coherent case only 83% population will be transferred and switching to incoherent scheme must happen to achieve full transfer.

these rates are equivalent when

$$\exp\left[-\frac{\gamma\eta}{2}t\right] = 2\exp[-\gamma t] \tag{7.15}$$

then solving for t

$$t = \frac{ln(2)}{\gamma(1-\frac{\eta}{2})} \tag{7.16}$$

for $\gamma = 1/7.2$ms and $\eta = 0.83$ this corresponds to a time of 8.53 ms and an F state

population of 0.576, whereas by rearranging equation (5)

$$t = -\frac{2}{\gamma\eta} ln(1 - \rho_F) \tag{7.17}$$

we see that incoherently this would have taken 14.9 ms to transfer 57.6% of the population to the F state. Saving us about 6.5 ms. Since the process of shelving takes about 100ms this 6% gain is unlikely to be advantageous considering the added difficulty of performing coherent operations with the 411nm laser. One could think of further schemes to increase speed such as coherent pulses to the D state with the 411 nm laser and then coherent pulse into the F state with a 3.4 μm laser (this could be done many times to the 14 available levels in the F manifold). This would not be limited in speed but poses the technical challenge of having both a 411 nm laser and a 3.4 μm laser coherent with each other.

7.4 Results

Shelving and deshelving was initially performed on $^{174}Yb^{+}$ as seen in figures 7.4 and 7.5. The population in the S manifold decreases exponentially as expected with a fitted time constant of 18ms. This data is taken by driving the 411 nm transition for varying times allowing population to decay to either the F or the S states and then Doppler cooling while collecting photons. A discriminator is placed between the well separated bright and dark state Poissonian distributions as in figure 7.9. After each repetition of the experiment the ion must be deshelved from the F state which is accomplished with the 760 nm laser. Figure 7.5 shows a time constant of a few ms with about 5 mW of power. For the deshelving process the short upper state lifetime (28.6 ns) [9] and the small partial linewidth keep this process well below saturation, meaning faster deshelving times occur linearly with increased power. However due to the long shelving time we find this deshelving rate to be sufficient.

In order to apply this technique to $^{171}Yb^{+}$ we measured the hyperfine transitions see figure 7.7. We find the interval of 190MHz as measured with our WSU2 High Finesse wavemeter which matches well with the previous measurements of 191(2) MHz [56]. The red detuned

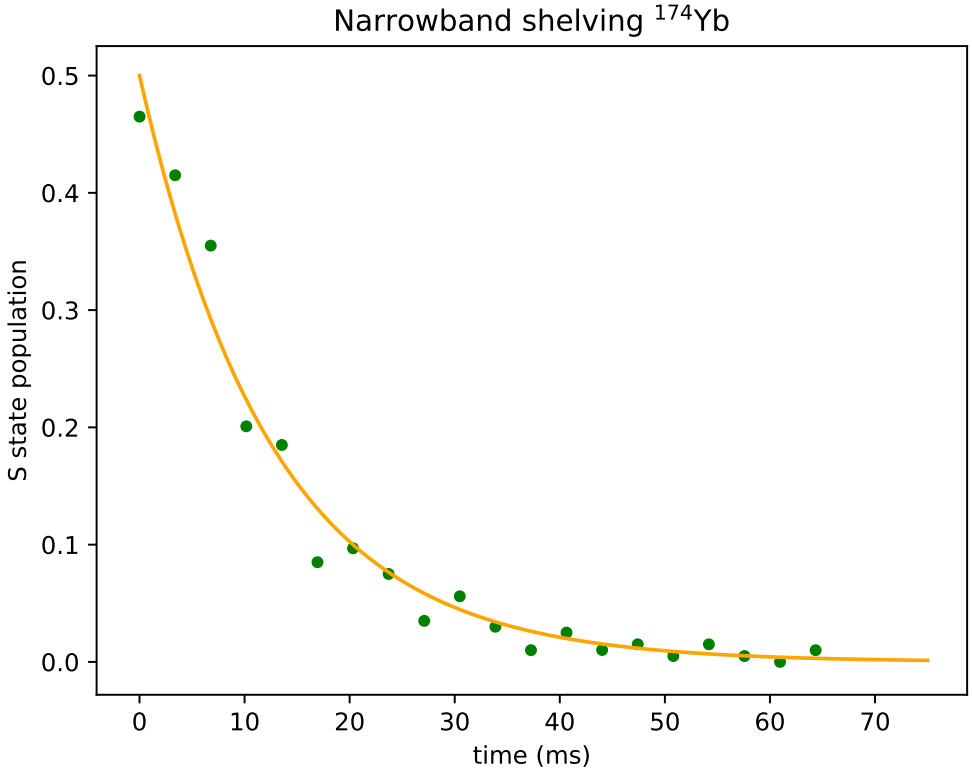

Figure 7.4: S state population transfer. A time constant of 18 ms shows this is very much in line with the theory

transition is the $^2S_{1/2}$ F=1 $\longrightarrow$ $^2D_{5/2}$ F=3 which we shelve on. One might be concerned with the Zeeman structure on this transition, however for the $^2S_{1/2}$ F=1 $\longrightarrow^2$ $D_{5/2}$ F=3, the Landau g factors are the same leading to degenerate Zeeman levels splitting into only 5 lines ($\Delta m = \pm 2, \Delta m = \pm 1$ and $\Delta m = 0$). This means that we can shelve all Zeeman levels with a single tone. We use linearly polarized light with a wave vector orthogonal to the B field which has the effect of removing the $\Delta m = 0$, however the other four lines are clearly visible in figure 7.6

The procedure for a single experiment is as follows

- Doppler cooling on the 369 nm transition (500 μs)
- Optical pumping on the $^2S_{1/2}$ F=1$\longrightarrow$ $^2P_{1/2}$ F=1 (20μs)

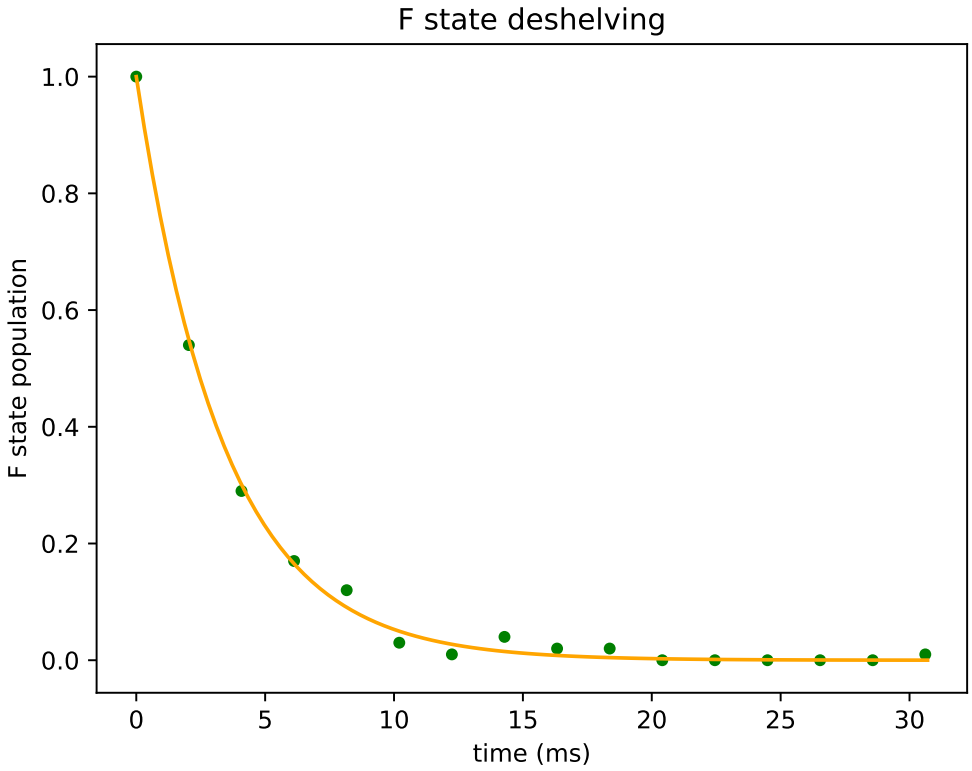

Figure 7.5: Deshelving of the F state manifold with the 760 nm repumpers. Time constants of a few ms are achieved with ≈5mW of power in a 100 μm beam waist.

- Variable Microwave pulse on the $|^2S_{1/2}, F = 0\rangle \longrightarrow |^2S_{1/2}, F = 1; m_F = 0\rangle$ (0-30 μs)
- 411nm shelving from the $^2S_{1/2}$ F=1 $\longrightarrow$ $^2D_{5/2}$ F=3 (100ms)
- Doppler cooling state detection with photon counting on (2ms)
- Deshelving with the 760nm laser (10ms)

It should be noted that for $^{171}Yb^+$ we required 2 lasers at 760 nm which we detuned by 5.257 GHz to deshelve both hyperfine levels in the F state. While a fiber EOM could be used, the power loss was unacceptable in these experiments.

By performing the outlined procedure, we are able to get coherent Rabi oscillations that very nearly approach unity contrast. Note this flopping is out of phase with the standard scheme because the "Bright" and "Dark" state have been flipped.

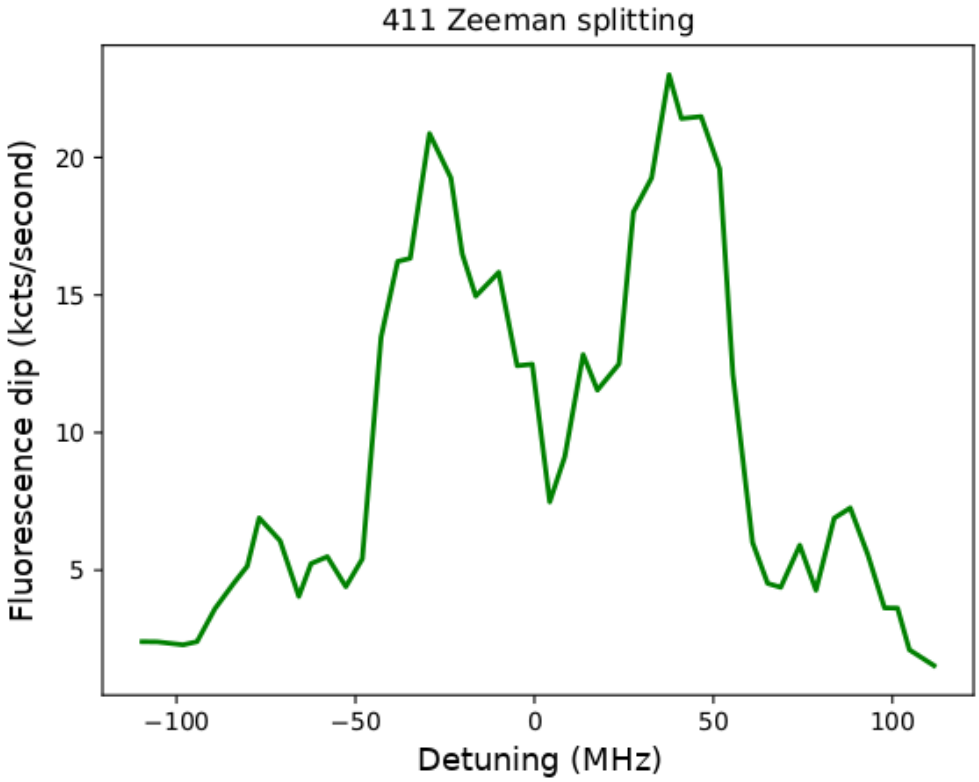

Figure 7.6: Zeeman splitting of the ${}^2S_{1/2}, F = 1 \longrightarrow {}^2D_{5/2}, F = 3$ transition. Detuning is of the red non-doubled light.

To achieve a quantitative fidelity measurement as in figure 7.9, the previous procedure was applied with two cases: First no microwave interaction ideally leaving the atom in the $|{}^2S_{1/2}, F = 0\rangle$ "Bright" state and Second a π area pulse ideally fully transferring the population to the $|{}^2S_{1/2}, F = 1; m_F = 0\rangle$ state. These two sequences were interleaved and sent to the FPGA pulse sequencer where hundreds of iterations at a time can be performed. The interleaving of bright and dark is intended to eliminate any systematic effects due to laser drift or ion loss.

When the data is returned by the FPGA the total counts achieved in each experiment are binned and plotted. A discriminator is placed between the two Poisson distributions and any ideally dark preparations right of the discriminator are counted as errors while any bright preparations to the left of the discriminator are also counted as errors. For the data presented here the achieved fidelity is 99.95(4), consistent with the best fidelity measurement

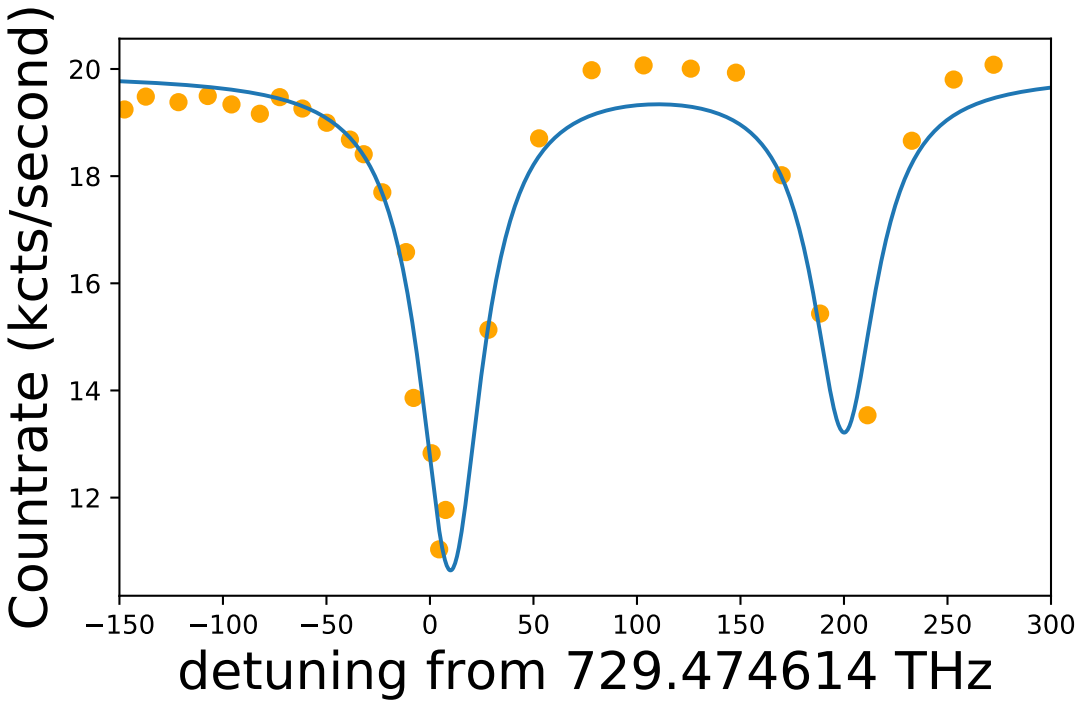

Figure 7.7: Initial measurement of the 411 nm hyperfine interval of the $^2D_{5/2}$ level. The splitting of 190MHz is in line with previous measurements [56]

in Yb^+ [16]. Recently we have diagnosed the remaining errors to be optical pumping and microwave errors and are continuing to improve the measured fidelity of this scheme.

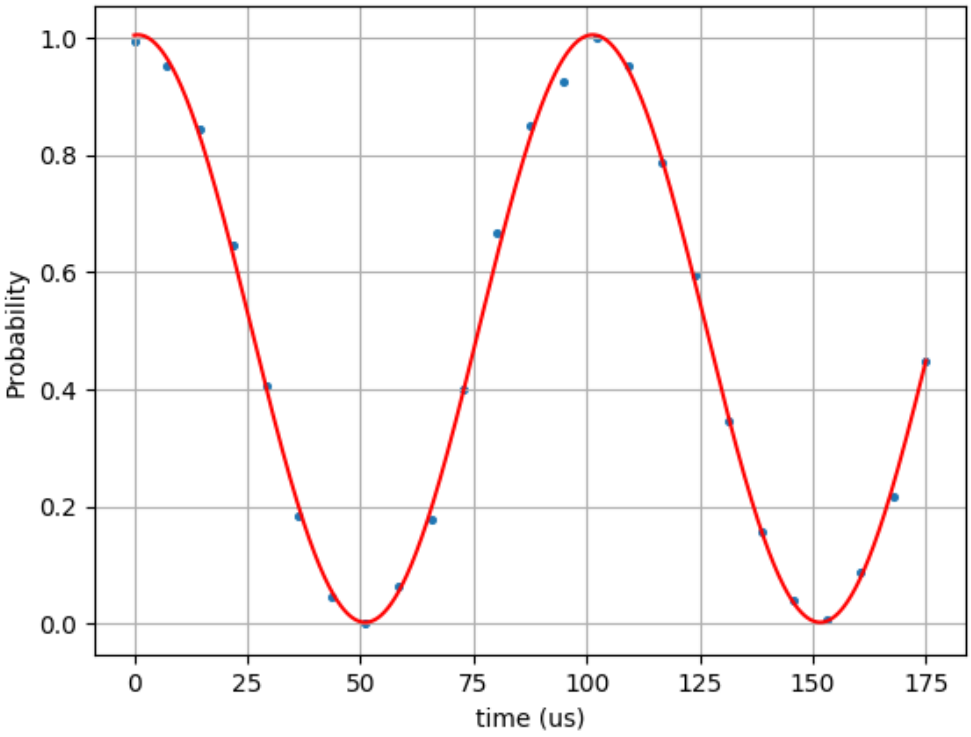

Figure 7.8: Rabi flopping on the hyperfine qubit in $^{171}Yb^{+}$ using the shelving technique

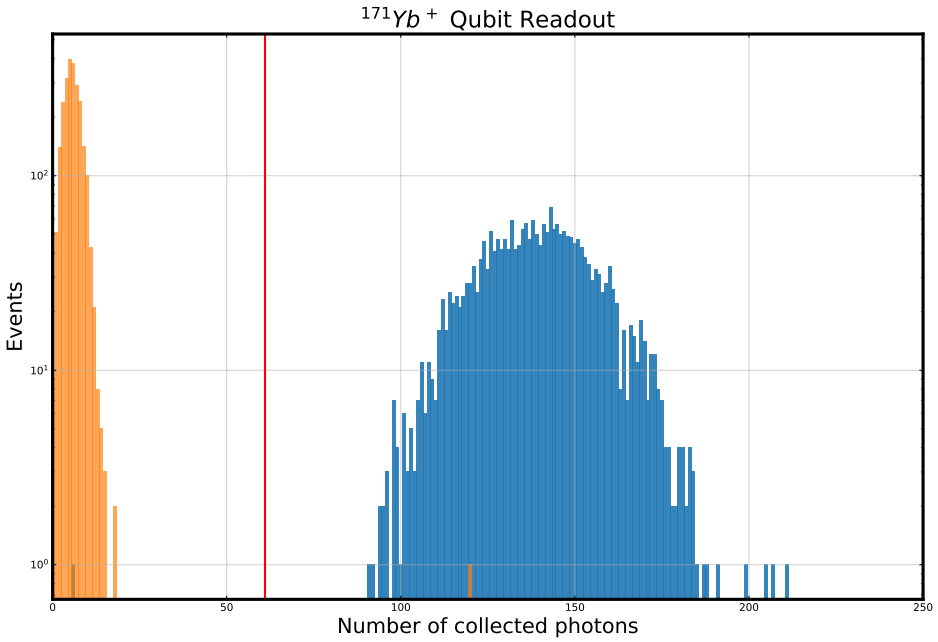

Figure 7.9: High fidelity state preparation and measurement of the hyperfine qubit. Fidelity is measured to be 99.95(4). Note the lack of decays in the region between Poissonians. This is due to the extremely long lived (5.5 yr) F state.

CHAPTER 8

Ultrafast State Detection

In order to scale trapped quantum computers, it is natural to integrate all the photonics into the actual trap. This is most conveniently accomplished in 2D surface traps that can be printed via lithography techniques that benefit greatly from the rich semiconductor technology. In such traps the laser delivery is generally accomplished by either skimming the surface with a laser beam or guiding the light with wave-guides under the trap [44]. Regardless of the technique, much larger amounts of scatter will enter the imaging system if the laser is closer to the trap thus adding noise to state detection. The standard way to remove such scatter is to spatially filter the light using apertures and relay imaging.

An alternative to spatial filtering is temporal filtering in which light is observed at specific times in a pulse sequence when background scatter is low. In the following we demonstrate temporal light filtering on both shelved hyperfine qubits and un-shelved hyperfine qubits.

Using and ultra-fast laser pulse we excite the ion nearly one thousand times faster than its decay time (excitation time $\sim$ 10ps, decay time 8ns). After the ion is excited fluorescence detection of the decaying photon will be free of any laser intensity and therefore background scatter.

8.1 Hyperfine

In the typical cw laser driven $I = \frac{1}{2}$ qubit state readout scheme [2], the $^2S_{1/2}$ F=1 $m_F = 0$ acts as the bright state; a single-frequency cw laser resonant with $^2S_{1/2}; F = 1 \rightarrow {}^2P_{1/2}; F = 0$ is applied and excited atoms spontaneously decay back to $^2S_{1/2}; F = 1$ with high probability [48]. This cycle is driven until the probability that off-resonant excitation mixes the qubit

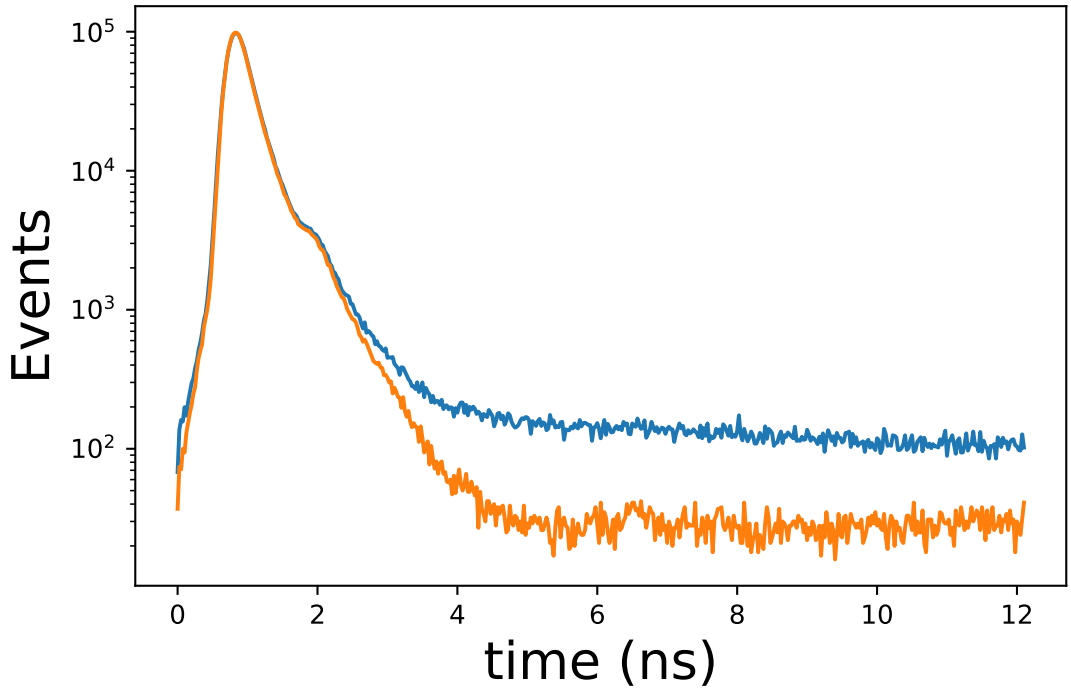

Figure 8.1: S-P lifetime measurement from ultrafast pulses

states and limits the SPAM fidelity.

For pulsed excitation a simple Fourier argument shows that we expect our ∼10ps pulses to have band widths on the order of 100 GHz. The spectral components near the ${}^2S_{1/2}; F = 1 \rightarrow {}^2P_{1/2}; F = 1$ transition would completely destroy the state selectivity of the scheme. In order to recover the state selectivity, we pass the mode-locked laser pulses through a Mach-Zehnder interferometer and remove the spectral components that would drive undesired transitions.

There are two undesired transitions. Besides the ${}^2S_{1/2}; F = 1 \rightarrow {}^2P_{1/2}; F = 1$, the ${}^2S_{1/2}; F = 0 \rightarrow {}^2P_{1/2}; F = 1$ transition will also destroy state selectivity. Fortuitously, the ratio of the lower hyperfine splitting (12.642/2.105) is very nearly an integer (6.005). For this reason, a single Mach-Zehnder interferometer will be able to avoid both undesired transitions (see figure 8.2).

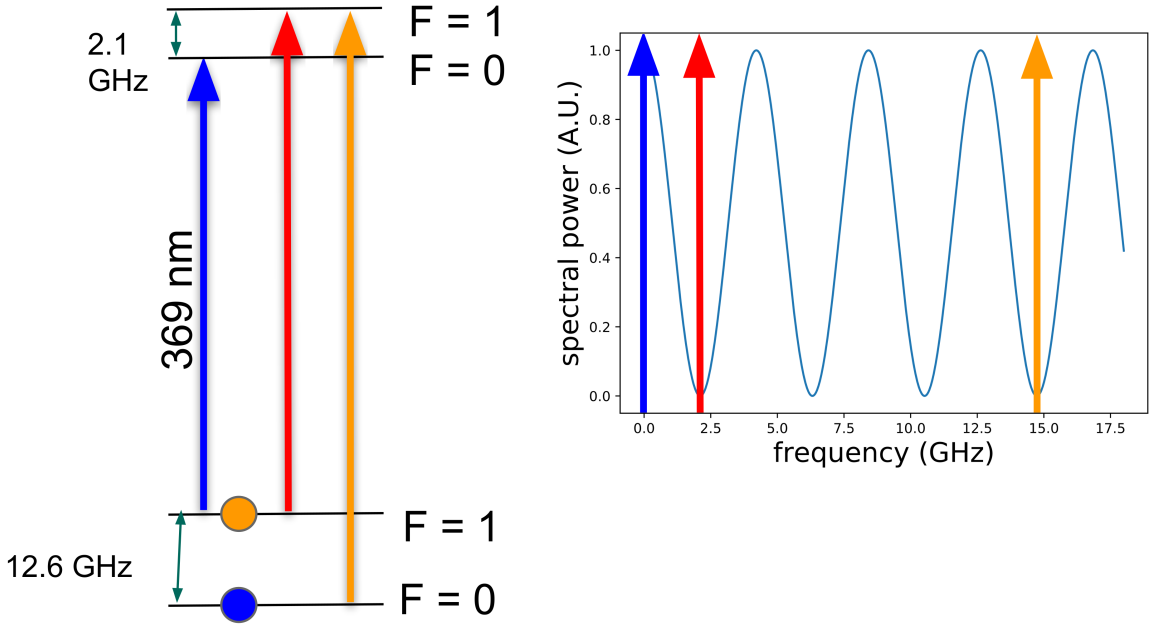

Figure 8.2: Hyperfine structure of $^{171}Yb^{+}$ (left) showing the transition in blue that we desire to drive and the orange and red transitions which are to be avoided. The right shows the frequency of these transitions relative to the state selective cycling transition (blue) superimposed with the Mach-Zehnder interferometer frequency output.

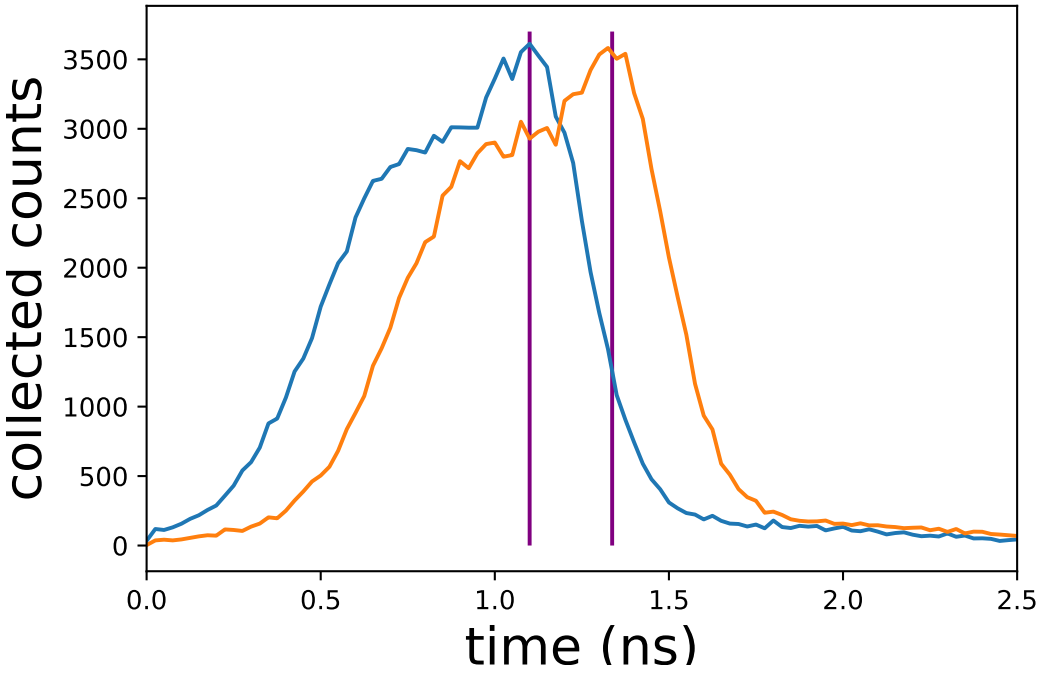

Figure 8.3: Scatter counted from the pulses on the TDC. The shape is due to after pulsing of the PMT. The two purple lines are 237 ps apart showing the coarse delay is set properly

8.2 Shelved Hyperfine

In contrast, for electron-shelved Yb ions, the roles are reversed and the population of the ${}^2S_{1/2}; F = 1$ manifold is transferred ("shelved") to a metastable state and photon collection during subsequent CW Doppler cooling is used to discern whether the ion was shelved. For shelving of ${}^{171}\mathrm{Yb}^+$ hyperfine qubits [52], we apply a laser at 411 nm to transfer population from $|1\rangle$ to the effectively stable ${}^2F^o_{7/2}$ state *via* the ${}^2D_{5/2}$ state. Subsequent illumination at 369.5 nm and 935.2 nm reveals essentially unlimited LIF for an ion found in $|0\rangle$, whereas an ion initially in $|1\rangle$ has been shelved and is dark (see previous chapter for more shelving details). This removes the need for the Mach-Zehnder interferometer.

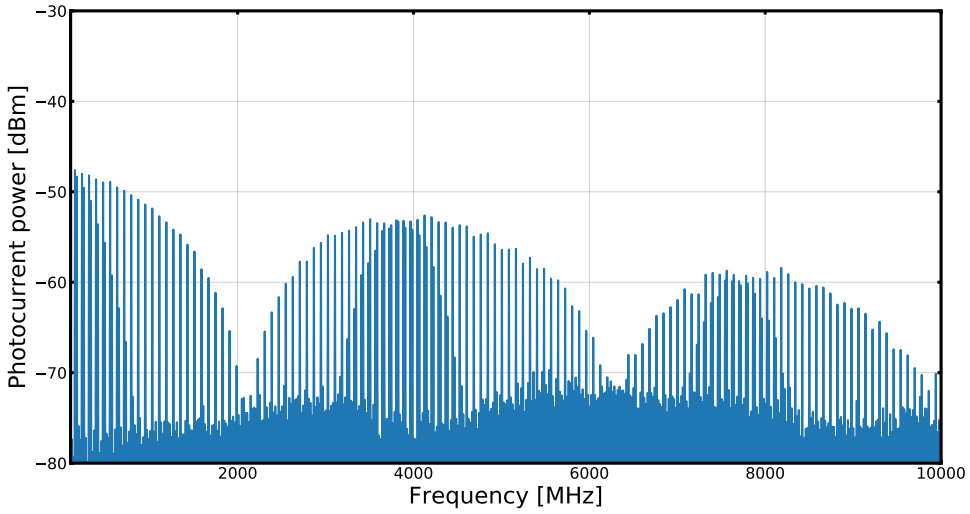

Figure 8.4: Frequency domain of pulses

8.3 Experimental setup

For the pulsed qubit state detection in this work, excitation of the bright state population to ${}^2P^o_{1/2}$ is driven by a frequency doubled mode-locked (ML) laser generating near-transform-limited ≈ 10 ps pulses at 369.5 nm with a repetition rate of $f_r = 79.5$ MHz. Because the laser-excited ${}^2P^o_{1/2}$ state has a lifetime of $\tau = 8.12$ ns [47], an atom excited by a pulse from the ML laser will emit a photon with high (78%) probability before the next pulse arrives. Nonetheless, multi-pulse coherence can still lead to strong comb tooth effects [33], and the positions of the laser's optical frequency comb teeth in this work are held far from any resonances by an intra-cavity piezo-mounted mirror. Pulse energies at the ion are typically ≈ 0.25 pJ, corresponding to a rotation of the atomic ${}^2S_{1/2} \leftrightarrow {}^2P^o_{1/2}$ Bloch vector of $\theta \approx 0.05\pi$. Ion fluorescence at 369.5 nm is collected by an objective lens and registered by a PMT through a 369 nm bandpass filter. The PMT output is monitored by either an FPGA-based photon time tagger (≈ 10 ns resolution [51]) or a fast, time correlated single photon counter (TCSPC, ≈ 25 ps resolution [1]).

[1] PicoQuant TimeHarp 260P

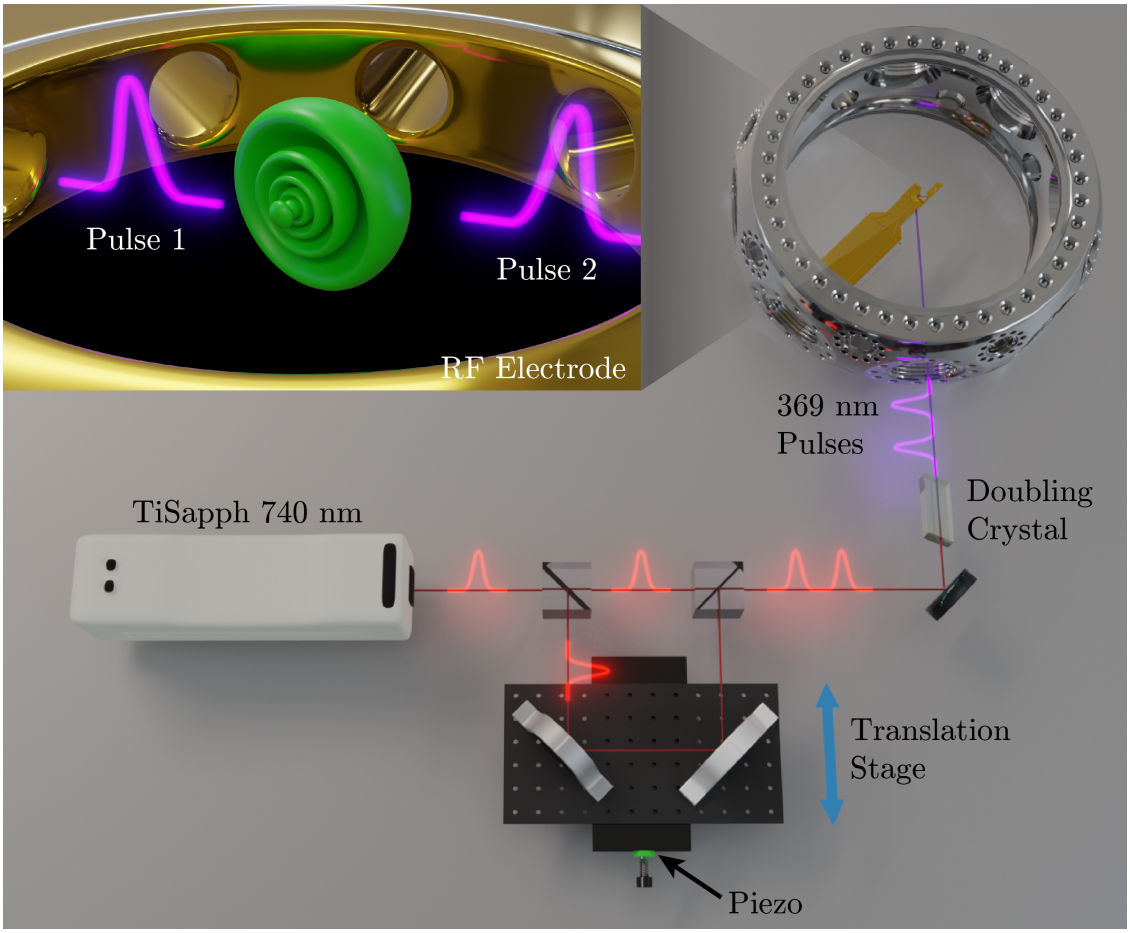

Figure 8.5: Experimental setup with Mach-Zehnder interferometer

The pulse pairs are created by sending pulses into a Mach-Zehnder interferometer figure 8.5. The interferometer delays the pulses by the required 237 ps and is tuned coarsely via a knob on a translation stage. The knob also contains a ring piezo. The piezo can change the fine scale of the interferometer in the sub-picosecond regime. The time domain of these pulses is shown in figure 8.3. Scatter of the ML laser off the trap generates the signal and this signal is used to power balance the two legs of the interferometer. In frequency space this will look like a phase filter and can be seen by measuring the output on a fast photo-diode which is read by a spectrum analyzer (figure 8.4)

For shelved and optical-frequency qubits, the population in ${}^2F^o_{7/2}$ is well separated from the ground and excited states (by $>$ 100 THz) and sits far outside the spectral bandwidth of the excitation pulse. Figure 8.1a shows a time trace of the collected photons from many

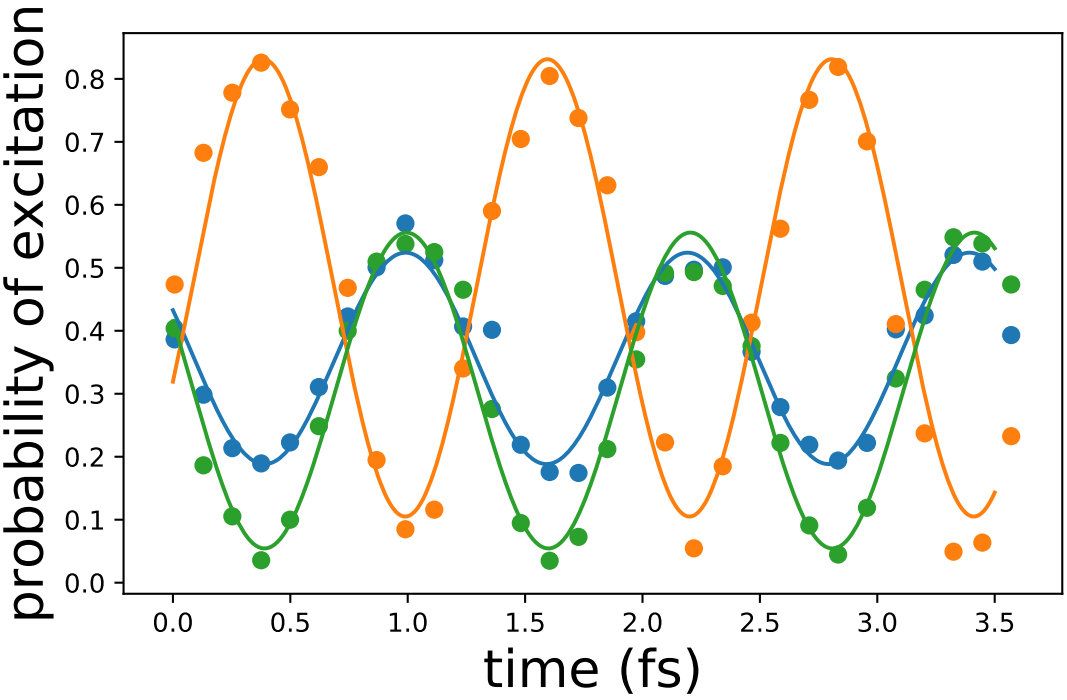

Figure 8.6: Ramsey experiment on the three transitions involved, orange is the F=1-F=0 manifold. The fidelity of the oranges is much higher do to the lack of mixing after a single scattered photon. For the other two transitions leakage occurs after a few scattering events

repeated excitations of a single $^{171}Yb^{+}$ ion initially prepared in the dark ($D_{3/2}$, blue trace) and bright ($S_{1/2}$, orange trace) states. The peak near $t = 1$ ns is caused by incidental laser scatter and is extinguished below the level of dark counts (40 s^{-1}) in about 4 ns. The observed pulse width of greater than 100 ps is due to the transit time spread of photoelectrons in the PMT. The window from $\approx 3 - 12.5$ ns, allows fluorescence detection that is essentially free of corruption by background scatter.

8.4 Results

By separately recording the number of collected photons for an ion initially prepared in dark state and the bright state for many repetitions, histograms of the two results are constructed (Fig. 8.8). Well-separated histograms are required for single-shot state detection, where a threshold is typically chosen between the two distributions to discriminate the two states. However, the total collected light, shown on the right side of Fig. 8.8, shows substantial overlap of the two histograms and poor state discrimination due to incidental scatter from the excitation laser, yielding an average single-shot detection fidelity of $\mathcal{F} = 0.76 \pm 0.01$ using a threshold.

In contrast, essentially all of the substantial technical scatter caused by the mode-locked laser can be rejected by repeating the same experiment while rejecting counts outside the background-free window. This is shown by the solid histograms on the left side of Fig. 8.8. This technique achieves an average single-shot detection fidelity of $\mathcal{F} = 0.9993^{+0.0003}_{-0.0006}$, and can be used, for instance, to observe high-contrast Rabi flopping of the qubit (Fig. 8.9). As a result, despite the high amount of scatter introduced by using a mode-locked laser for qubit state detection, temporal rejection of background counts effectively eliminates the background scatter as a concern for detection fidelity. The remaining errors (the three blue counts in the solid red histogram on the left side of Fig. 8.8) are consistent with the bright state histogram and are therefore likely due to incomplete shelving, not poor manifold discrimination. Further improvements in shelving [52] can be used to reduce this infidelity, and this type of error will be entirely absent for optical-frequency qubits.

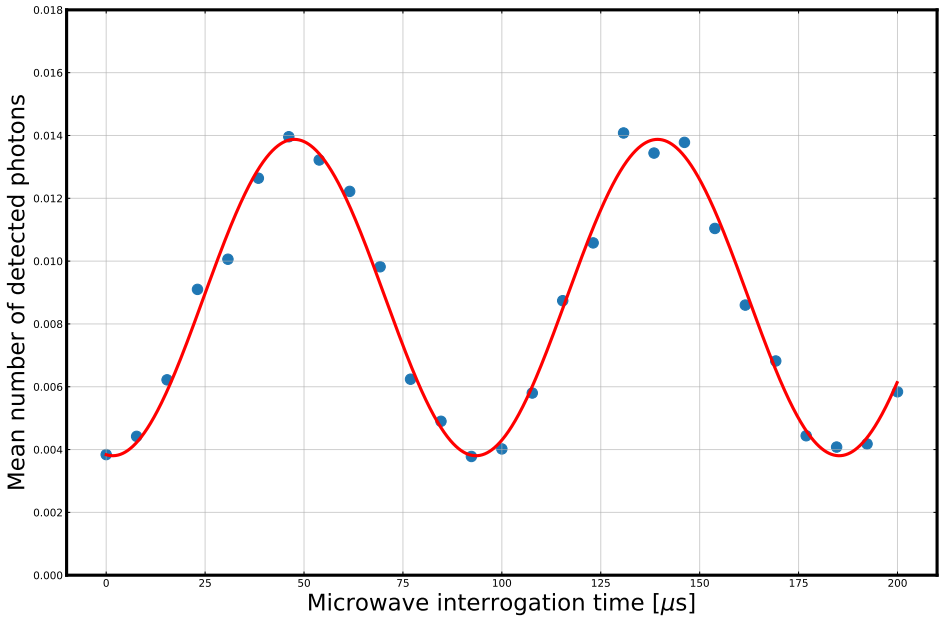

Figure 8.7: Detection of Rabi oscillation of the hyperfine qubit using the frequency comb

Given the improvement that this technique can provide for scatter-dominated environments, it is well suited for chip-based systems with integrated detectors, where high solid angle can be achieved, but scatter cannot be well filtered spatially. In particular, integrated superconducting nanowire single photon detectors, which feature high efficiency at relevant wavelengths, low dark counts, high maximum count rates, and fast timing resolution, are being integrated into next-generation ion systems [62, 67, 16]. With an estimated fractional solid angle coverage of 5% (taken from the middle of the predicted 3%-8% range for future integrated SNSPDs [62]) and a system detection efficiency of 60%, an optical-frequency qubit (or pre-shelved hyperfine qubit) in the bright state will be able to produce an average of 10 detector counts in $\approx$5 s. Even if complete temporal filtering of the incidental scatter requires discarding half of these LIF counts, the achievable fidelity is $> 99\%$ in only 5s.

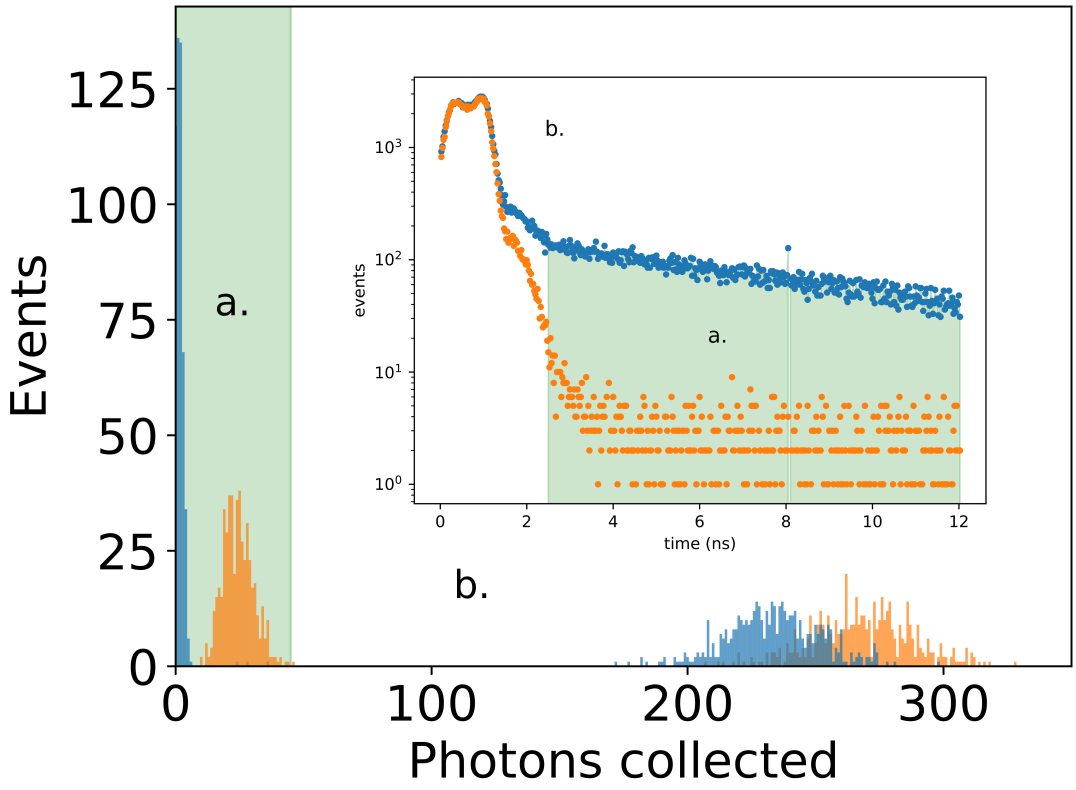

Figure 8.8: Detection of Rabi oscillation of the hyperfine qubit using the frequency comb

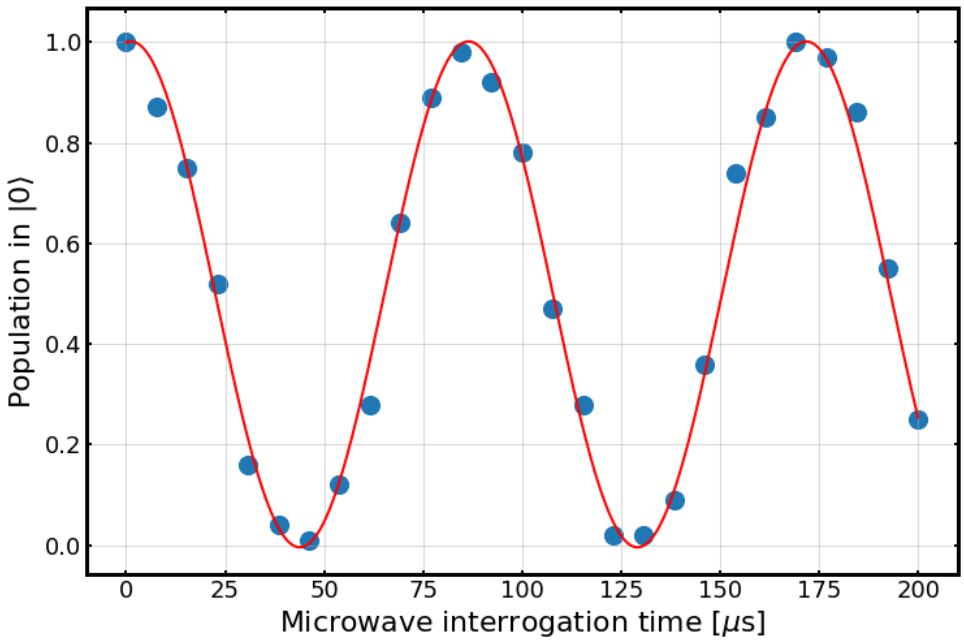

Figure 8.9: Detection of Rabi oscillation of the hyperfine qubit using the frequency comb after shelving to the F state

CHAPTER 9

The F state as a Resource for Quantum Information

9.1 A Qubit in the F state

The F state of Yb provides a platform for another qubit contained in the same ion. Using the lessons from the standard qubit we desire a clock transition. On top of this, we would like to prepare a pure quantum state. The first requirement is easy, in $^{171}Yb^{+}$ this is accomplished by the $|^2F_{7/2}, F = 3, m_F = 0\rangle$ and the $|^2F_{7/2}, F = 4, m_F = 0\rangle$ states. These states are separated by 3.6GHz and can be driven with microwaves. The second task, state preparation will be more challenging but can be accomplished via heralding as described below

9.1.1 State Preparation, Manipulation and Measurement of F state Qubits

State preparation can be heralded in two ways, either with a coherent laser or with optical pumping.

Coherent-laser heralded state preparation of $^{171}Yb^{+}$

One way is to prepare a pure state is to use the octupole [55] transition at 467 nm, to drive a π on the $|^2S_{1/2}, F = 0\rangle \longrightarrow |^2F_{7/2}, F = 3, m_F = 0\rangle$. In practice this pulse can only be accomplished with finite fidelity; however, by subsequently applying 369 nm Doppler cooling light a null measurement projects the ion into $|^2F_{7/2}, F = 3, m_F = 0\rangle$.The fidelity of which is now limited by either off resonant Zeeman states in the F=3 manifold (this can be arbitrarily mitigated with laser intensity and B fields) or the lifetime of the F state. During Doppler cooling, photon counts of a bright ion can be around 100,000 counts per second with a

standard 0.3 NA lens. This means that the probability the ion was in the S manifold after only 200 μs of detection and no photons collected is about 2×10^{-9}. With reasonable powers and narrow enough frequencies preparation times of a few ms could be achieved, limited by the Rabi frequency of the 467 nm transition with reasonable intensities.

Incoherent-laser heralded state preparation of $^{171}Yb^{+}$

Another way to prepare a pure state is to first optically pump population into the $^2F_{7/2}$, F=3 manifold via 411 nm light on the $^2S_{1/2}, F = 1 \longrightarrow^2 D_{5/2}, F = 2$ transition. The population will now be in a mixed state of this manifold however one could still perform a π area pulse on the clock qubit transferring what population exists in the $|^2F_{7/2}, F = 3, m_F = 0\rangle$ state to the $|^2F_{7/2}, F = 4, m_F = 0\rangle$. After performing this pulse, deshelving via the 760 nm laser on the $^2F_{7/2}, F = 3 \longrightarrow^1 [3/2]_{3/2}$, F=1 manifold will move the population into the cooling cycle leading to fluorescence, or project the ion into the pure state $|^2F_{7/2}, F = 4, m_F = 0\rangle$ heralded by no fluorescence. Deshelving to the F=1 bracket state would protect against population mixing due to quadrupole selections rules.

9.1.2 Driving the F state qubit

The F-state qubit can be driven directly with microwaves at 3.6 GHz, providing an excellent way to rotate single qubits for global non-entangling rotations. In order for the qubits to be useful we must be able to couple their motion to a laser field. A few options listed below.

- stimulated Raman transitions off the strong $^2F_{7/2} \longrightarrow (7/2, 0)_{7/2}$ or $(7/2, 1)_{7/2}$ states at 363 nm and 378 nm respectively.
- quadrupole transitions via the $^2F_{7/2} \longrightarrow^3 [11/2]_{9/2}$ or $^3[11/2]_{11/2}$ at 1136 nm 1094 nm respectively
- directly with the octupole transition at 467 nm

9.2 Towards Qudits in the F state

The weak transition at 467 nm severely limits the first state detection scheme. Luckily $^{173}Yb^{+}$ highly deformed nucleus, discussed earlier in this thesis, resolves this problem. The nuclear deformation induces a dipole moment between the $^{2}S_{1/2}$ and $^{2}F_{7/2}$. This dipole moment is predicted to drastically reduce the lifetime of this state from years to days[21]. This means heralded state preparation of this isotope will be fast and high fidelity.

Not only does $^{173}Yb^{+}$ provide fast high fidelity pure state preparation, but the $^{2}F_{7/2}$ manifold provides an extremely rich set of levels allowing manipulation of an SU(48) system. These levels are conveniently separated by microwave frequencies which enjoy all the coherence and simplicity afforded to $^{173}Yb^{+}$. A large system like this that can be prepared and measured are referred to as qudits. Most of these available levels will be magnetically sensitive, however the six $m_f = 0$ allow the creation of an N=6 qudit.

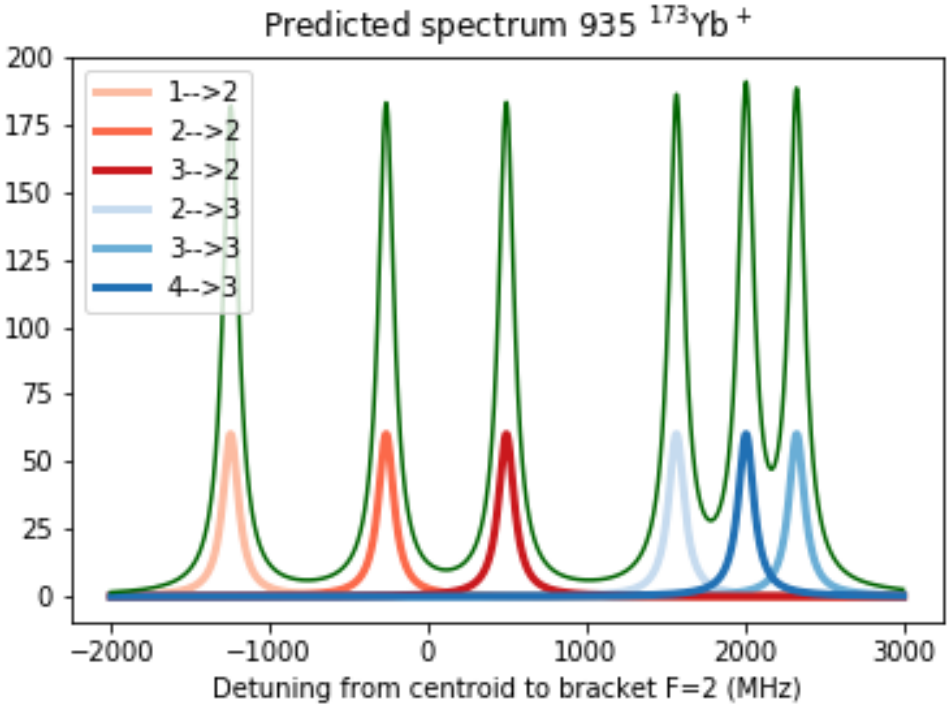

Figure 9.1: Predicted spectra of the 935 nm transition based on hyperfine coefficients

CHAPTER 10

Quantum Networks and the F state of Yb (possible future directions)

Quantum networks are promising for key distribution, connected quantum information processors and quantum repeaters [5][17]. Entanglement between distant systems is accomplished in trapped ions via short pulse excitations of two distant qubits to a quickly decaying state. The resultant emitted photons are interfered on a beam splitter and joint detection of the photons heralds entanglement between the ions. [18][60]. This probabilistic process requires many ($\sim 10^4$) scattering events that induce cross-talk in neighboring trapped ions. Spontaneous photon emission resonant with nearby adjacent ions is a fundamental source of cross-talk. One way to mitigate cross-talk is by using multi-species traps, e.g. $^{138}Ba^+$ and $^{171}Yb^+$ [34], necessitating multi-species two qubit gates in order to share information across the ion chain. The mass mismatch complicates entanglement swapping between the photonic interconnected ions and the memory qubits and the frequency mismatch can lead to an optical beat note whose phase must be tracked [31]. The best fidelity of these multi-species gates is far worse than any other gate in trapped ions required for quantum information processing [63][35][29]. In the following we describe how to use the unique meta-stable $^2F^o_{7/2}$ state in Yb^+ to protect neighboring ions from cross-talk allowing remote entanglement generation without disturbing nearby ions and removing the requirement of multi-species gates altogether.

10.1 Remote entanglement

Remote entanglement was achieved between ions separated by meters over a decade ago [18]. Subsequent work achieved teleportation of quantum states [60] and entanglement with ancilla ions in the trap [17]. Despite large N.A. which allow for large photon collection probabilities, heralded remote entanglement in ion traps is still limited to rates of 10-100 Hz [17]. This slow rate creates challenges for two reasons. First, entangled states tend to decohere on these time scales induced by the entanglement generation laser which is on resonance with qubit states functionally connected to the dissipative cooling cycle. Second, and more fundamentally, the entanglement ion emits light which scrambles the information in register ancilla ions.

The standard solution to this is to employ an alternate species to generate entanglement [34]. This second species has transitions many THz from the ancilla qubits and thus does not cause decoherence. Besides the challenges of having to include multiple loading sources, a new set of lasers, and new optical paths for these lasers, there are more fundamental problems. The normal mode structure of the ion chain becomes more complicated. Also, the different masses can cause heating during shuttling due to stray fields. Finally, multi-species requires two sources that are coherent with each other requiring beat note stability [31] since the qubits are generally driven with different sources.

Metasable states allow for electron shelving both incoherently and coherently which can remove ions from any states connected to a dissipative channel. For current entanglement generation rates however, even the very long lived $^2D_{5/2}$ of Ba^+ ($\sim$ 30s) would lead to large errors limiting the fidelity to $\sim$ 99.9% worse than state of the art single qubit [29], two qubit [35] and state preparation and measurement (SPAM) errors [38].

The submerged $^2F^o_{7/2}$ in Yb^+ lives for 5.5 years [54, 55] due to its only decay path being an electric octupole transition. This state has a sufficient lifetime to shelve ancilla qubits during trap-trap entanglement generation. Shelving may be accomplished incoherently via a quadrupole transition at 411 nm or coherently at 467 nm by driving the octupole directly as

in Figure 1. This transition has been driven before and is currently employed as a clock at physikalisch-technische bundesanstalt (PTB) [58]. Although possible to drive the transition is slow due to its weak coupling (electric octupole), luckily an easier path to driving this transition may be in $^{173}Yb^{+}$ where the highly deformed nucleus induces a dipole moment and is theorized to have lifetimes of several days [21], drastically increasing the rate it can be driven at while still allowing for sufficiently long shelving times.

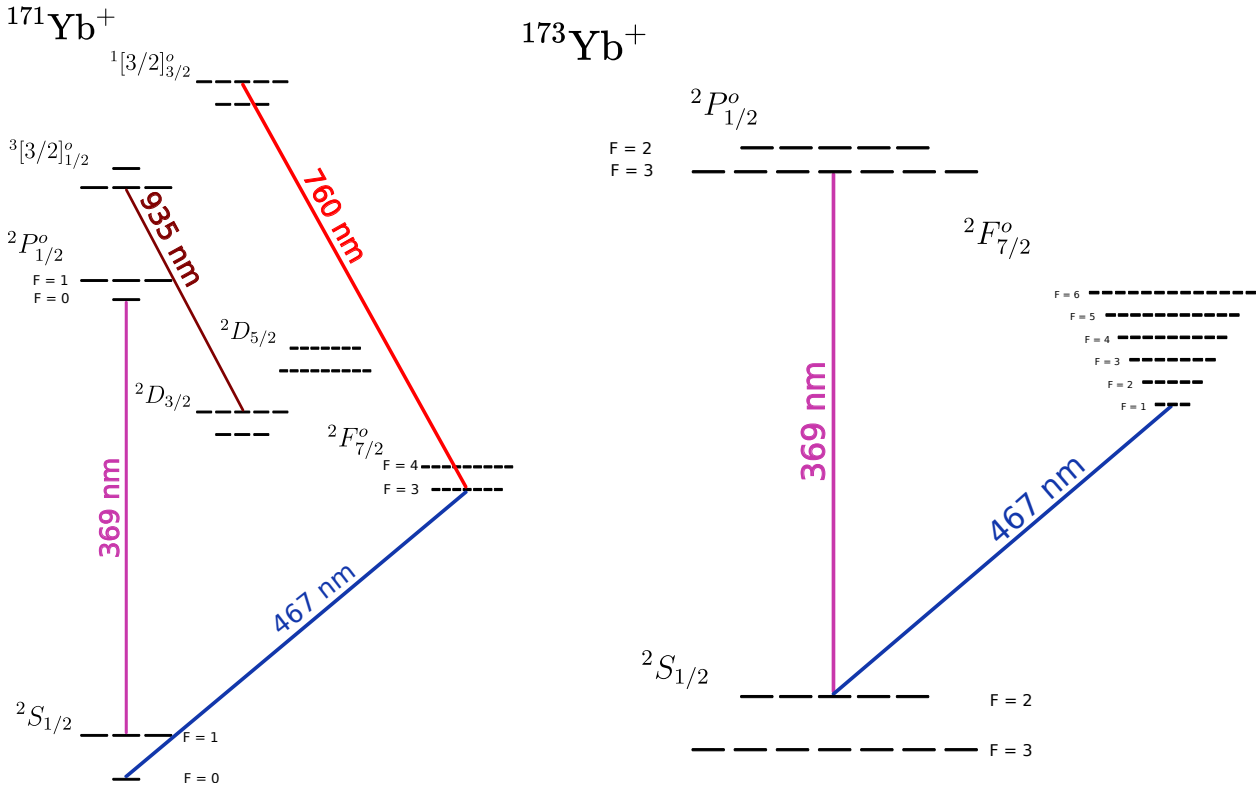

Figure 10.1: Structure of $^{171}Yb^{+}$. Frequency-selective driving of the $^2S_{1/2}(F=0)$ states to $^2F^o_{7/2}(F=3)$ on the octupole transition will coherently shelve this population. $^{173}Yb^{+}$ structure used in fast excitation and shelving (right)

In what follows we describe three possible shelving schemes of ancilla qubits and generate cross-talk free entanglement across two traps. First, using four $^{171}Yb^{+}$ (two in each trap), where one ion in each trap is chosen as the ancilla and the other is chosen as the entangling qubit. Second a pair of $^{171}Yb^{+}$ and $^{173}Yb^{+}$ ion are co-loaded in each trap, where the $^{173}Yb^{+}$ acts as the ancilla qubit and the established remote entanglement scheme is used for the two

$^{171}Yb^+$ ion in each trap. Finally, two $^{173}Yb^+$ ions are loaded in each trap with one behaving as the ancilla. These schemes are described in the following sections.

10.2 Scheme I: $^{171}Yb^+$-$^{171}Yb^+$

Current remote entanglement schemes in Yb^+ exclusively employ the ion $^{171}Yb^+$. This tested system provides a natural starting point for implementing shelved ancilla qubits. One standard approach entangles the frequency of the photons with the ion. Ions in two separate traps are optically pumped to the $|F = 0, m_f = 0\rangle$ state of the $^2S_{1/2}$ state via state selective tones, followed by microwaves to generate superpositions of the $|F = 0, m_f = 0\rangle$ and $|F = 1, m_f = 0\rangle$ states. Subsequent illumination of pulsed, π-polarized light will simultaneously and state selectively (aided by selection rules) map the superposition to the excited $^2P^o_{1/2}$ manifold hyperfine structure $|F = 0, m_f = 0\rangle$ $|F = 1, m_f = 0\rangle$ states for both ions. The ions are then allowed to decay via dipole emission with σ^+, σ^- or π radiation. A polarizer selects π radiation and the photons are guided to a non-polarizing beam splitter where they interfere. While we only consider frequency-ion state entanglement, the polarization degree of freedom of the photon can also be used.

One could add to this already established scheme an ancilla ion to each of the two traps. These two ancilla ions (one in each trap) will be optically pumped into a pure state along with the neighboring entangling ions. After the state is created however, individual addressing of the ancilla qubit at 467 nm will coherently transfer its state to the $^2F^o_{7/2}$ along the magnetically insensitive transition $^2S_{1/2}|F = 0, m_f = 0\rangle \rightarrow {}^2F^o_{7/2}|F = 3, m_f = 0\rangle$. While this maps the simple state $^2S_{1/2}|F = 0, m_f = 0\rangle$, a superpostion of ground states could also be mapped to two F state levels and will be discussed later. This operation has moved the ancilla qubit into a fully protected space. It will neither see microwave transitions at the standard qubit frequency nor fast pulse excitations to the dipole excited $^2P^o_{1/2}$. Also, subsequent optical pumping events after failed entanglement generation will not mix this shelved qubit. Entanglement generation can now proceed the standard way and upon a heralded event (coincidence click) the population can be returned to the $^2S_{1/2}|F = 0, m_f = 0\rangle$ and the state

of the system will be pure and well defined, allowing quantum processing between ancilla and entangled qubits. This processing can now proceed with a single coherent e.g. (355 nm stimulated Raman) source due to the ions being the same species.

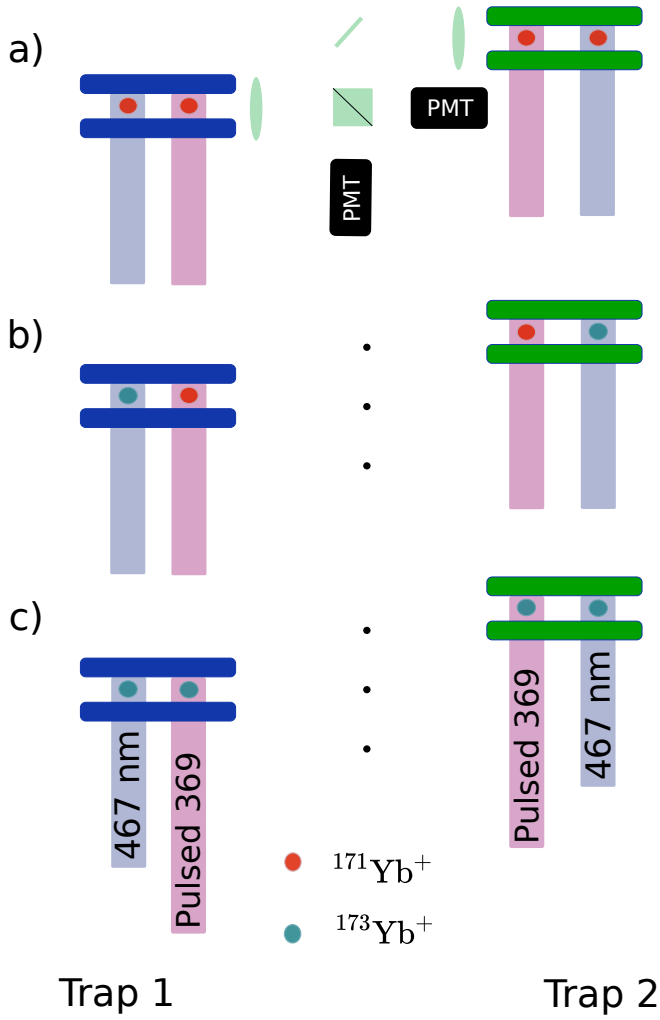

Figure 10.2: Three methods of cross-talk free remote entanglement: $^{171}Yb^+$-$^{171}Yb^+$, (b) $^{171}Yb^+$-$^{173}Yb^+$ and (c) $^{173}Yb^+$-$^{173}Yb^+$

10.3 Scheme II: 171-173

The very weak coupling of the 467 nm transition leads to challenges in laser power and speed. The estimated transfer rate for population to these states are estimated to be only

a few hundred Hz. $^{173}Yb^{+}$ however, has a highly deformed nucleus which induces and $\vec{E} \cdot \vec{d}$ coupling of the $^{2}S_{1/2}$ and $^{2}F^{o}_{7/2}$ states. This coupling is predicted to shorten the lifetime of certain hyperfine levels in the excited states by up to 3 orders of magnitude [21] leading to Rabi frequencies 30 times faster $\sim$ 10 kHz. In order to use this ion, state preparation and measurement of the $^{173}Yb^{+}$ hyperfine qubit must be performed for the first time. Luckily similar ions, namely $^{137}Ba^{+}$ and $^{43}Ca^{+}$, which have nuclear spins 3/2 and 7/2 respectively, have successfully been used as qubits. We could use a similar scheme with $^{173}Yb^{+}$.

Laser cooling of $^{173}Yb^{+}$ can be performed using a resonant 5.246 GHz electro-optical modulator (EOM) such that the first order sidebands span the 10.49 GHz hyperfine splitting. The laser can be addressed to either the $^{2}P^{o}_{1/2}$ $F = 3$ or $F = 2$ (Figure 3). In order to avoid coherent population trapping all polarizations will be applied to the light. To prepare a pure state (optical pumping), the polarization will be switched to linear along the quantization axis (π light), this will drive all transition except for ΔF = 0, $\Delta m_F = 0$. This allows for stochastic pumping into the pure quantum state $|F = 2, m_F = 0\rangle$ or $|F = 3, m_F = 0\rangle$ depending on which upper hyperfine state is addressed. After the ion arrives in a pure state a coherent pulse will be applied with the 467 nm laser moving the population into a single $^{2}F^{o}_{7/2}$ hyperfine and Zeeman level e.g. ($|F = 3, m_f = 0\rangle$). The ion will now be protected from any scatter near 369 nm and remote entanglement generation of neighboring $^{171}Yb^{+}$ ions may proceed.

10.4 Scheme III: 173-173

While the approach in Part II allows one to use the standard remote entanglement scheme of $^{171}Yb^{+}$ with the fast shelving of $^{173}Yb^{+}$ in concert, it is not strictly speaking a single species. Entanglement has been performed on multiple calcium isotopes with fidelities on par with same species two qubit gates (0.998(6)) it would be technically simpler to use a single isotope. In the final part of this proposal we describe how to use two $^{173}Yb^{+}$ ions, one to generate remote entanglement across traps and one to store protected quantum information.

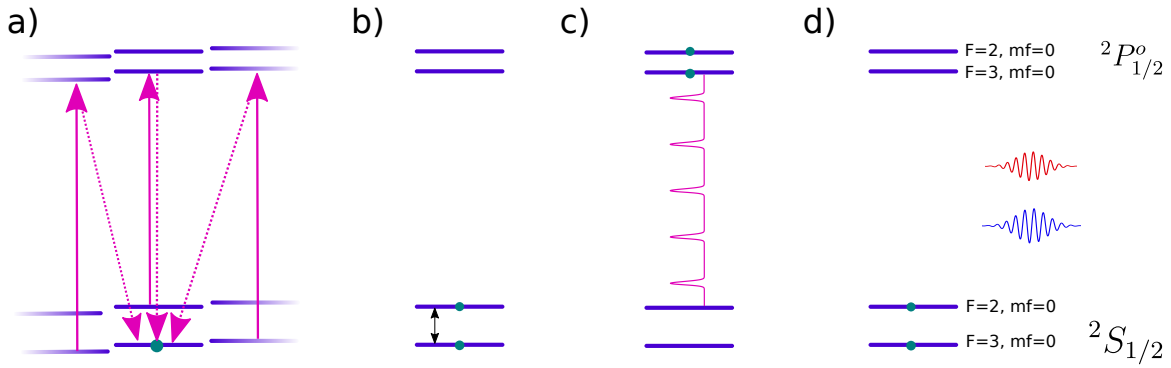

Figure 10.3: Ion photon frequency entanglement scheme in $^{173}Yb^+$. The ion is optically pumped with pi light (a), microwaves at 10.49GHz drive a superposition of qubit states (b), a mode-locked pulse maps the population (selection rules prevent mixing) (c) and finally the emitted photon color is entangled with the final state of the ion

With all ions being the same isotope cooling, repumping and coherent laser sources can be tuned to the same frequency reducing complexity. After first exploring full protection of these qubits during remote entanglement we will explore hiding coherent superpositions of states in the ancilla qubits as required for a full quantum information processor.

Octupole transition selection rules allow for transitions where the total angular momentum F changes by 3. The $^2F_{7/2}$ state in $^{173}Yb^+$ has six hyperfine levels with angular momenta F=1 to F=6. This allows coupling of the ground state F=2 to F=1,2,3,4,5 and the F=3 to F=1,2,3,4,5,6. The boost in transition strength only occurs in dipole allowed transitions thus for concreteness we propose mapping the $^2S_{1/2}|F=2,m_f=0\rangle$ and $^2S_{1/2}|F=3,m_f=0\rangle$ to the $^2F_{7/2}|F=3,mf_0\rangle$ and $^2F_{7/2}|F=2,mf_0\rangle$ states respectively.

The procedure for this will be as follows:

- Optically pump the ancilla qubits and entangling qubits in both traps to $^2S_{1/2}|F=2,m_f=0\rangle$
- Perform global microwave pulse to create a superposition of $^2S_{1/2}|F=2,m_f=0\rangle$ and $^2S_{1/2}|F=3,m_f=0\rangle$

- Map the ancilla superpositions to two F state levels with 467 nm light via individual addressing
- Perform remote entanglement scheme outlined in Part II on entangling qubits
- Upon heralding of entanglement return superpositions of ancilla to the ground state manifold via 467 nm

References

[1] Email communication.

[2] M. Acton et al. *Quantum. Inf. Comp.*, 6:465, 2006.

[3] Markus Ansmann. *Benchmarking the superconducting Josephson Phase Qubit: The violation of Bell's inequality.* Citeseer, 2009.

[4] D. Aumiler and T. Ban. Simultaneous laser cooling of multiple atomic species using an optical frequency comb. *Phys. Rev. A*, 85:063412, 2012.

[5] L. M. Duan C. Monroe B. B. Blinov, D. L. Moehring. Observation of entanglement between a single trapped atom and a single photon. *Nature*, 428:153–157, 2004.

[6] Vladimir M. Bedanov and François M. Peeters. Ordering and phase transitions of charged particles in a classical finite two-dimensional system. *Phys. Rev. B*, 49:2667–2676, Jan 1994.

[7] K. Beloy, A. Derevianko, V. A. Dzuba, G. T. Howell, B. B. Blinov, and E. N. Fortson. Nuclear magnetic octupole moment and the hyperfine structure of the $5D_{3/2,5/2}$ states of the ba^+ ion. *Phys. Rev. A*, 77:052503, May 2008.

[8] Paul Benioff. Quantum mechanical hamiltonian models of turing machines. *Journal of Statistical Physics*, 29(3):515–546, Nov 1982.

[9] R. W. Berends, E. H. Pinnington, B. Guo, and Q. Ji. Beam-laser lifetime measurements for four resonance levels of YB II. *Journal of Physics B: Atomic, Molecular and Optical Physics*, 26(20):L701–L704, 1993.

[10] RW Berends, EH Pinnington, B Guo, and Q Ji. Beam-laser lifetime measurements for four resonance levels of yb ii. *Journal of Physics B: Atomic, Molecular and Optical Physics*, 26(20):L701, 1993.

[11] D. J. Berkeland and M. G. Boshier. Destabilization of dark states and optical spectroscopy in zeeman-degenerate atomic systems. *Phys. Rev. A*, 65:033413, Feb 2002.

[12] Joseph W Britton, Brian C Sawyer, Adam C Keith, C-C Joseph Wang, James K Freericks, Hermann Uys, Michael J Biercuk, and John J Bollinger. Engineered two-dimensional ising interactions in a trapped-ion quantum simulator with hundreds of spins. *Nature*, 484(7395):489–492, 2012.

[13] Natalie C Brown and Kenneth R Brown. Comparing zeeman qubits to hyperfine qubits in the context of the surface code: Yb+ 174 and yb+ 171. *Physical Review A*, 97(5):052301, 2018.

[14] CIAAW. Atomic weights of the elements 2019.

[15] J. I. Cirac and P. Zoller. Quantum computations with cold trapped ions. *Phys. Rev. Lett.*, 74:4091–4094, May 1995.

[16] Stephen Crain, Clinton Cahall, Geert Vrijsen, Emma E. Wollman, Matthew D. Shaw, Varun B. Verma, Sae Woo Nam, and Jungsang Kim. High-speed low-crosstalk detection of a $^{171}Yb^{+}$ qubit using superconducting nanowire single photon detectors. *Communications Physics*, 2:97, 2019.

[17] G. Vittorini C. Crocker S. Debnath S. M. Clark D. Hucul, I. V. Inlek and C. Monroe. Modular entanglement of atomic qubits using photons and phonons. *Nature Phys.*, 11:37–42, 2014.

[18] S. Olmschenk K. C. Younge D. N. Matsukevich L.M. Duan C. Monroe D. L. Moehring, P. Maunz. Entanglement of single-atom quantum bits at a distance. *Nature*, 449:68–71, 2007.

[19] Josue Davila-Rodriguez, Akira Ozawa, Theodor W. Hänsch, and Thomas Udem. Doppler cooling trapped ions with a UV frequency comb. *Phys. Rev. Lett.*, 116:043002, 2016.

[20] David P. DiVincenzo. The physical implementation of quantum computation. *Fortschritte der Physik*, 48(9[U+2010]11):771–783, 2000.

[21] V. A. Dzuba and V. V. Flambaum. Hyperfine-induced electric dipole contributions to the electric octupole and magnetic quadrupole atomic clock transitions. *Phys. Rev. A*, 93:052517, 2016.

[22] D. Felinto, C. A. C. Bosco, L. H. Acioli, and S. S. Vianna. Coherent accumulation in two-level atoms excited by a train of ultrashort pulses. *Optics Communications*, 215:69, 2003.

[23] Richard P. Feynman. Simulating physics with computers. *International Journal of Theoretical Physics*, 21:467–488, 1982.

[24] Christopher J Foot. *Atomic physics*. Oxford master series in atomic, optical and laser physics". Oxford University Press, Oxford, 2007.

[25] Pradip K Ghosh. Ion traps. 1995.

[26] Lov K. Grover. A fast quantum mechanical algorithm for database search, 1996.

[27] T. W. Hänsch and A. L. Schawlow. Cooling of gases by laser radiation. *Optics Communications*, 13:68, 1975.

[28] Aram W. Harrow, Avinatan Hassidim, and Seth Lloyd. Quantum algorithm for linear systems of equations. *Phys. Rev. Lett.*, 103:150502, Oct 2009.

[29] T. P. Harty, D. T.C. Allcock, C. J. Ballance, L. Guidoni, H. A. Janacek, N. M. Linke, D. N. Stacey, and D. M. Lucas. High-fidelity preparation, gates, memory, and readout of a trapped-ion quantum bit. *Physical Review Letters*, 113(22):2–6, 2014.

[30] Michael R. Hush, Weibin Li, Sam Genway, Igor Lesanovsky, and Andrew D. Armour. Spin correlations as a probe of quantum synchronization in trapped-ion phonon lasers. *Phys. Rev. A*, 91, 2015.

[31] D. Hucul C. Crocker I. V. Inlek, G. Vittorini and C. Monroe. Multi-element logic gates for trapped-ion qubits. *Phys. Rev A*, 043216:90, 2015.

[32] E. Ilinova, M. Ahmad, and A. Derevianko. Doppler cooling with coherent trains of laser pulses and a tunable velocity comb. *Phys. Rev. A*, 84:033421, 2011.

[33] Michael Ip, Anthony Ransford, Andrew M Jayich, Xueping Long, Conrad Roman, and Wesley C Campbell. Phonon lasing from optical frequency comb illumination of trapped ions. *Physical review letters*, 121(4):043201, 2018.

[34] M. Lichtman K. Sosnova I. V. Inlek, C. Crocker and C. Monroe. Multi-element logic gates for trapped-ion qubits. *Phys. Rev. Lett.*, 250502:118, 2017.

[35] Y. Lin Y. Wan R. Bowler A. C. Keith S. Glancy K. Coakley E. Knill D. Leibfried J. P. Gaebler, T. R. Tan and D. J. Wineland. Multi-element logic gates for trapped-ion qubits. *Phys. Rev. Lett.*, 117:060505, 2015.

[36] John David Jackson. Classical electrodynamics 3rd edition. *Cited on*, page 17, 1998.

[37] A. M. Jayich, X. Long, and W. C. Campbell. Direct frequency comb laser cooling and trapping. *Phys. Rev. X*, 6:041004, 2016.

[38] Wesley C. Campbell Eric R. Hudson Justin E. Christensen, David Hucul. High fidelity manipulation of a qubit built from a synthetic nucleus. *arXiv*, arXiv:1907.13331, 2015.

[39] K. Kim, M. S. Chang, R. Islam, S. Korenblit, L. M. Duan, and C. Monroe. Entanglement and Tunable Spin-Spin Couplings between Trapped Ions Using Multiple Transverse Modes. *Physical Review Letters*, 103(12):1–4, 2009.

[40] Walter Koechner. *Solid-State Laser Engineering*. 01 2006.

[41] Tony E. Lee, Ching-Kit Chan, and Shenshen Wang. Entanglement tongue and quantum synchronization of disordered oscillators. *Phys. Rev. E*, 89:022913, 2014.

[42] Tony E. Lee and H. R. Sadeghpour. Quantum synchronization of quantum van der Pol oscillators with trapped ions. *Phys. Rev. Lett.*, 111:234101, 2013.

[43] E. Mathieu. Memoire sur le mouvement vibratoire d'une membrane de forme elliptique. *Journal de Mathématiques Pures et Appliquées*, pages 137–203, 1868.

[44] Karan K. Mehta, Colin D. Bruzewicz, Robert McConnell, Rajeev J. Ram, Jeremy M. Sage, and John Chiaverini. Integrated optical addressing of an ion qubit. *Nature Nanotechnology*, 11:1066, 2016.

[45] Harold J. Metcalf and Peter van der Straten. *Laser Cooling and Trapping*. Springer-Verlag, New York, 1999.

[46] W. Neuhauser, M. Hohenstatt, P. Toschek, and H. Dehmelt. Optical-sideband cooling of visible atom cloud confined in parabolic well. *Phys. Rev. Lett.*, 41:233, 1978.

[47] S. Olmschenk, D. Hayes, D. N. Matsukevich, P. Maunz, D. L. Moehring, K. C. Younge, and C. Monroe. Measurement of the lifetime of the $6p\ ^2P^o_{1/2}$ level of yb^+. *Phys. Rev. A*, 80:022502, Aug 2009.

[48] S. Olmschenk, K. C. Younge, D. L. Moehring, D. N. Matsukevich, P. Maunz, and C. Monroe. Manipulation and detection of a trapped yb^+ hyperfine qubit. *Phys. Rev. A*, 76:052314, Nov 2007.

[49] M. J. Petrasiunas, E. W. Streed, T. J. Weinhold, B. G. Norton, and D. Kielpinski. Optogalvanic spectroscopy of metastable states in Yb^+. *Applied Physics B*, 107(4):1053–1059, 6 2012.

[50] John Preskill. Quantum Computing in the NISQ era and beyond. *Quantum*, 2:79, August 2018.

[51] Thaned Pruttivarasin and Hidetoshi Katori. Compact field programmable gate array-based pulse-sequencer and radio-frequency generator for experiments with trapped atoms. *Rev. Sci. Instrum.*, 86:115106, 2015.

[52] A. Ransford, C. Roman, T. Dellaert, P. McMillin, and W. C. Campbell. Manuscript in preparation. 2020.

[53] R. L. Rivest, A. Shamir, and L. Adleman. A method for obtaining digital signatures and public-key cryptosystems. *Commun. ACM*, 21(2):120–126, February 1978.

[54] M Roberts, P Taylor, G P Barnwood, P Gill, H A Klein, and W R C Rowley. Observation of an electric octupole transition in a single ion. *Physical Review Letters*, 78:1876, 1997.

[55] M Roberts, P Taylor, G P Barnwood, W R C Rowley, and P Gill. Observation of the $^2S_{1/2} -^2 F_{7/2}$ electric octupole transition in a single $^{171}Yb^+$ ion. *Physical Review A*, 62:020501(R), 2000.

[56] M. Roberts, P. Taylor, S. V. Gateva-Kostova, R. B. M. Clarke, W. R. C. Rowley, and P. Gill. Measurement of the 2S1/2-2D5/2 clock transition in a single 171Yb+ ion. *Physical Review A*, 60(4):2867–2872, 1999.

[57] Thomas Ruster, Christian T Schmiegelow, Henning Kaufmann, Claudia Warschburger, Ferdinand Schmidt-Kaler, and Ulrich G Poschinger. A long-lived zeeman trapped-ion qubit. *Applied Physics B*, 122(10):254, 2016.

[58] S A Webster H S Margolis L A M Johnson K Szymaniec P E G Baird S A King, R M Godun and P Gill. Absolute frequency measurement of the 2s1/2–2f7/2 electric octupole transition in a single ion of 171yb+ with 10−15 fractional uncertainty. *New Journal of Physics*, 323:14, 2012.

[59] P. Maunz D. Hayes L. M. Duan S. Olmschenk, D. N. Matsukevich and C. Monroe. Quantum teleportation between distant matter qubits. *Science*, 323:486–489, 2009.

[60] P. Maunz D. Hayes L.M. Duan C. Monroe S. Olmschenk1, D. N. Matsukevich. Quantum teleportation between distant matter qubits. *Science*, 323:486–489, 2009.

[61] Peter W. Shor. Polynomial-time algorithms for prime factorization and discrete logarithms on a quantum computer. *SIAM Rev*, 41(2):303–332, 1997.

[62] D. H. Slichter, V. B. Verma, D. Leibfried, R. P. Mirin, S. W. Nam, and D. J. Wineland. Uv-sensitive superconducting nanowire single photon detectors for integration in an ion trap. *Opt. Express*, 25(8):8705–8720, Apr 2017.

[63] Y. Lin Y. Wan R. Bowler D. Leibfried T. R. Tan, J. P. Gaebler and D. J. Wineland. Multi-element logic gates for trapped-ion qubits. *Nature*, 528:380, 2015.

[64] P Taylor, M Roberts, SV Gateva-Kostova, RBM Clarke, GP Barwood, WRC Rowley, and P Gill. Investigation of the 2 s 1/2- 2 d 5/2 clock transition in a single ytterbium ion. *Physical Review A*, 56(4):2699, 1997.

[65] D. J. Wineland and H. Dehmelt. Proposed $10^{14}\delta\nu < \nu$ laser fluorescence spectroscopy on Tl^+ mono-ion oscillator. *Bull. Am. Phys. Soc.*, 20:637, 1975.

[66] D. J. Wineland, R. E. Drullinger, and F. L. Walls. Radiation-pressure cooling of bound resonant absorbers. *Phys. Rev. Lett.*, 40:1639, 1978.

[67] E. E. Wollman, V. B. Verma, A. D. Beyer, R. M. Briggs, B. Korzh, J. P. Allmaras, F. Marsili, A. E. Lita, R. P. Mirin, S. W. Nam, and M. D. Shaw. Uv superconducting nanowire single-photon detectors with high efficiency, low noise, and 4 k operating temperature. *Opt. Express*, 25:26792–26801, 2017.

[68] Bryce Yoshimura, Marybeth Stork, Danilo Dadic, Wesley C Campbell, and James K Freericks. Creation of two-dimensional Coulomb crystals of ions in oblate Paul traps for quantum simulations. *EPJ Quantum Technology*, 2:2, 2015.

[69] N Yu and L Maleki. Lifetime measurements of the 4 f 14 5 d metastable states in single ytterbium ions. *Physical Review A*, 61(2):022507, 2000.